Non-invasive Detection of Peripheral Arterial Disease in the Lower Limb

Diana-Mădălina Suciu

A thesis presented for the degree of
Master of Chemistry

University of Kent

Acknowledgements

I would like to start by thanking the University of Kent for giving me the opportunity to complete my study here. I am also utterly grateful to my supervisory team: Dr Robert Barker, Dr Stuart Gibson, Irantzu Yoldi and Dr Matthew Hockley.

I am extremely thankful towards Dr Robert Barker, for all the opportunities he has offered me during all the time we have worked together. Your advice and insight has always helped solve any issues and your encouragement and enthusiasm has always been motivating.

I would like to also express my gratitude towards Irantzu Yoldi for the constant support throughout this research, particularly for all the help regarding the physiology of a foot and all the inside jokes that resulted out of it.

I am also utterly grateful to Dr Matthew Hockley. Your guidance, patience, knowledge and constant moral support have been extremely inspiring. Thank your for listening, for always offering your advice and for always making me take my lunch breaks! I can easily say that your presence has been pivotal for my learning and development, especially regarding coding.

I am also grateful for all the support received from our research group. Many thanks to Dr Fungisai Matemadombo, George Tushingham, Chloe Skingle, Ashton Stone, Jack Marsh, Alix Blissett and James Lockhart. You have always made the long hours spent in the lab turn into a friendly and fun environment.

I would also like to thank Phil Marsh for always being helpful and allowing me to use parts of his laboratory when needed.

I also must thank Dr Vassilia Spathis and Faith Taylor for being amazing friends and for listening to my excessive whining and existential crises. The times spent with you after a long day in the lab made me want to do it all over again. I have learned a lot from you two and I thank you for giving me the best memories I could have gotten during university.

Last, but never the least, I would like to thank my parents for all the moral support while being away from home. They consistently push me to become a better person and they inspire me everyday.

Contents

Appendices 98

Abstract

Multispectral imaging (MSI) is a novel, non-invasive technique, which can detect tissue reflectance and deliver information regarding tissue oxygenation. The application of spectral imaging in medical care, can lead to development of early-stage diagnosis and monitoring of vascular diseases, such as Peripheral Arterial Disease. Although MSI is known to be widely applicable with a high functionality, many techniques have not been fully validated and require bulky, non-intuitive setup and analysis, hence more research and clinical trials are required. This thesis presents the first step of the development cycle in collaboration with the National Health Service, to create a low-cost, portable device for use in a clinical setting and that can also be transported to housebound patients.

The system uses a four-lens multispectral camera and 16 attachable filters available in the visible range of 500 nm - 650 nm, with an LED medical lamp to collect images of a foot before and during arterial occlusion, using a blood pressure cuff inflated at 180 mmHg. A MATLAB program was created and used for calibration, processing of images and implementation of Beer-Lambert function; which delivered the oxygen saturation value. Four wavelengths were chosen as best fit: 520 nm, 540 nm, 610 nm, 640 nm, out of which 520 nm represents the isobestic wavelength, where no variation is seen between the image with and without cuff occlusion. Whereas, the other three wavelengths represent the opposite.

The system created and the final results can provide proof of principle regarding the feasibility of the technology presented. Although, the results of the preliminary four filters were not highly conclusive, the methodologies developed provide a promising platform for future optimisation.

Chapter 1

Introduction

The method presented in this research uses multispectral imaging (MSI) for detection of tissue oxygenation, while also attempting to improve the technical aspects of the camera, making it more portable, cost effective and easily transportable to patients.

The following chapters will explain the process created, starting with a brief literature introduction and continuing with the technical set-up of the method, the development of the image processing program and the analysis of the final results, whilst also presenting various future perspectives.

1.1 Peripheral Arterial Disease

1.1.1 Function of the arterial system

The circulatory system as a whole, has the task of assisting main functions such as transportation of oxygen and nutrients, balance of extracellular fluid, and it also plays an important part in a number of physiological functions.[1] These functions can vary from contributing to hormonal control to helping in regulating the body temperature.[1]

Blood is transported through the body via two circulation pathways; systemic and pulmonary.[1,2] The pulmonary circuit describes the transport of blood from the right ventricle of the heart to the lungs, from where it returns to the left ventricle of the heart and continues to be transported to the rest of the body through the systemic circuit. The latter consists of arteries, which carry oxygenated blood through the body before splitting into smaller vessels; and of veins which have the task of returning blood with less oxygen back to the heart, including carbon dioxide and other waste products.[1,2]

Both veins and arteries share more or less similar structural characteristics. Although

they are both blood supply vessels, arteries have to resist the higher pressure of the blood being expelled from the heart and further transported through the body. Hence, arteries consist of a thicker internal muscle and elastin layer than other blood vessels, also aiding in maintaining a suitable blood flow through the expansion of the vessel walls. Arteries display a smaller diameter, which benefits in controlling the pressure of blood as it travels through the vessel.[1,2]

Blood pressure has an important role in the circulation of blood. Systemic arterial blood pressure varies according to the cardiac cycle, meaning that it will be recorded as two values: systolic (maximum) and diastolic (minimum) pressure. The systolic pressure represents the rate at which blood is being ejected from the heart during the ventricular contraction. Diastolic pressure represents the arterial pressure during the relaxation of the ventricle. The greater blood pressure out of the two recorded is the systolic pressure, as the rate at which the blood is ejected into the systemic arteries is higher than during relaxation of the ventricle.[1,2] Following these fluctuations, a pressure wave is formed, resulting in a pulse that can be perceived at various parts of the body.[1]

Blood vessels possess a characteristic called compliance. This indicates the ability of a blood vessel to expand in order to adjust blood flow oscillations without a great resistance or an increased blood pressure.[2] Unlike veins, arteries do not have a high compliance, thus in the presence of a vascular disease they cannot expand as much resulting in increased resistance to blood flow and higher pressure.[2]

Therefore, the difference in the structural components of blood vessels aids in the transport of blood through the body and to extremities, by maintaining an adequate level of blood flow and pressure.[1,2]

1.1.2 Formation of Peripheral Arterial Disease

The normal function of the arterial system can unfortunately be disrupted by disorders of the cardiovascular system, such as arteriosclerosis. Arteriosclerosis is characterised as "hardening of the arteries", when compliance of the vessel decreases.[2]

One type of arteriosclerosis is atherosclerosis, a condition that forms when a buildup of fatty, calcified deposits, called plaques, block the arteries and hinder blood flow, Figure 1.1.[2–4] When arteries are half or fully blocked, the blood flow to the rest of the body decreases – this is known as ischemia. Ischemia will eventually create hypoxia, which occurs when there is not enough oxygen supply to the tissue.[2]
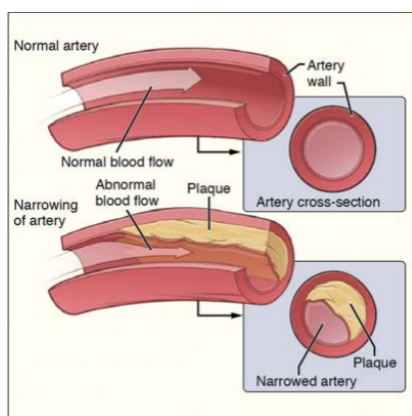
Figure 1.1: Plaques that form inside blood vessels, leading to atherosclerosis.[2]

Atherosclerosis in the lower extremity of the body leads to Peripheral Arterial Disease (PAD). Depending on the severity of the disease, PAD can manifest in two ways: asymptomatic or symptomatic.[3] Symptoms of PAD range from intermittent claudication, when any pain felt during effort will subdue with rest, to critical limb ischemia (CLI). CLI is caused by severe occlusion of arteries and it can be presented either as resting pain and/or ulcers of the lower limbs.[3] Unfortunately, critical limb ischemia will frequently result in amputation of the affected areas and patients have a higher risk of premature death.[3,5]

There are multiple risk factors that can lead to peripheral arterial disease. These factors can range from cigarette smoking to hypertension and elevated fibrinogen levels. However, this type of lower limb disease is particularly common in people diagnosed with diabetes mellitus.[3]

In cases where diabetes is prolonged and not regulated accordingly, it can lead to an irreversible nerve and tissue damage.[6] The presence of such damage births diabetic neuropathy which can decrease or even lose the performance of sensory and autonomic functions related to the lower limbs. These losses display themselves through insensitivity, limited mobility of specific areas, callus development, excessive pressure etc., eventually producing more extreme conditions such as ulcers.[6,7] Studies have found that around half the patients with diabetes suffer from PAD.[5] Thus, diabetes patients with neuropathy are inclined to also exhibit PAD although due to the nerve damage, they will more likely be asymptomatic therefore increasing the difficulty in detection and monitoring.[5]

A report from the UK Diabetes Annual Conference 2017,[8] indicates that individuals that are affected by diabetes have a 25% chance of also forming a foot ulcer and that approximately 86,000 individuals in the UK suffer from diabetic foot ulcers concurrently. In Europe and USA, diabetic foot infections form about a quarter of diabetes hospital admissions. Of these, up to 85% of lower limb amputations were caused by ulcers.

Despite diabetes being a frequent generator for PAD, as described above, this is not the only cause of it. In fact, guidelines point out that the overall chance of developing PAD for patients that suffer from diabetes is closely resembling that of smokers.[5]

Even though the risks of PAD are alarming, the majority of people are asymptomatic

and only 1-3% patients in 5 years will advance to critical limb ischemia from intermittent claudication.[5] However, when a patient becomes affected by CLI, studies show that the survival rate is lower than for some cancers. Research expresses that individuals are exposed to a 30% chance of limb amputation over one year and a 50% mortality risk over five years.[5,9] An observational study also concluded that mortality rate for patients that had to endure limb amputation was two times lower than for patients who were not subjected to such procedure.[5,10]

1.1.3 Contemporaneous detection methods

The chances of lower limb amputation could be drastically reduced if the detection and monitoring techniques available could provide more information regarding the evolution of the disease. In terms of investigating and detecting PAD, a variety of non-invasive methods are used by clinicians.

A common method to examine patients at risk is taking pressure measurements. Ankle-brachial index(ABI) and toe-brachial index(TBI) are measurements that use the differences in the systolic blood pressure between brachial - upper arm artery - and ankle/toe to indicate the presence of PAD.[4] Although these methods can offer valid indications and are not as costly, Grimaldi *et al.*[11] and Barshes *et al.*[12] point out the limitations of ABI in cases where individuals also exhibit vascular stiffness, as this can yield erroneous results such as false-negatives. The blood vessels in the far extremities, such as toes are not prone to stiffening, hence TBI may become a more favourable approach.

There are other existing blood pressure assessments that aid in the diagnosis of peripheral arterial disease. Such measurements can include transcutaneous partial pressure of oxygen (TcPO2). TcPO2 delivers an indirect estimate of arterial flow by measuring the level of oxygen underneath the skin.[11] Another measurement is skin perfusion pressure (SPP). This involves controlled minimal arterial occlusion and is also considered to be preferable when assessing PAD in comparison to ABI, TBI and TcPO2, due to a higher sensitivity rate.[8,11,12] Research regarding the use of TcPO2 has concluded that, although the technique involves a higher cost and demonstrates a slightly lower precision than TBI and SPP, its use can still be beneficial if other methods are not accessible.[12]

Similarly to TcPO2, there is a method of detecting the oxygen saturation level by using pulse oximetry. A pulse oximeter monitors the oxygenation of the blood, by examining the ratio between the absorption of light in oxyhaemoglobin and deoxyhaemoglobin in blood, at

a specific location.[13,14] Pulse oximetry is widely used in an intensive care environment as it is considered to be cost-effective.[15] However, the method is not included in the initial PAD assessment. Although some studies have concluded that pulse oximetry could be useful together with other presumptive tests[16], there are other research that disputes this theory, mainly due to the instrument proving to lack the sensitivity needed for early PAD detection[17,18]; but also due to the false results that can yield when tested close to arterial blockage.[19]

As an addition to these assessments, walking tests can be performed by clinicians while also applying a fair test to it. That means that the patients will have to exercise for a specific period of time but one or more of the above measurements would have been executed before and after the activity. This test is considered inadequately controlled and subjective according to certain studies; some variables such as speed or distance, have not been taken into consideration.[4,11,20]

The general investigation of peripheral arterial disease also includes Doppler ultrasonography. This is a non-invasive procedure and it is displayed as a continuous wave in conjunction with a sound signal based on the fluctuations created by the flow of the blood in the arteries.[4] Combining the Doppler system for blood flow display with the ultrasound imaging for vessel visualisation, results into a technique called duplex scanning. The method can provide valuable data, although it seems to be somewhat inadequate for detecting disease in the lower extremities.[4,11,20]

Besides the pulse and pressure measurements performed, ultrasonography is one of the most frequently promoted non-invasive technique to be used during PAD investigation.[4,20] However, although many health care professionals use a Doppler instrument during patient assessment, there is a lack of access to duplex scanning.[20,21] The reasons for this, firstly consist of the high cost that such equipment represents; and secondly, the practitioner using the equipment has to be highly trained. Moreover, an assessment can take up to two hours, which can be inconvenient especially since patients have to be on site to be examined.[20]

On the other hand, albeit the use of a simple Doppler system can still be costly and require adequate training, it can still provide a strong indication during an assessment. Furthermore, the portable function of the instrument permits at-home assessments, which is highly beneficial for patients. However, although non-invasive, the use of a Doppler requires direct contact of the probe with the skin, which is not possible if the skin is ulcerated or has other skin disorders.[4,20]

In addition to this, there are other more complex imaging techniques that can provide

extra information regarding the development of the disease. Of these, one imaging technique would be angiography[11], which is based upon X-ray visualisation of the blood vessel after they had been injected with a contrast medium. It is a common imaging method, however it has its drawbacks as well. Not only it is an invasive procedure executed under radiation exposure, but it can also produce further complications and it is an expensive procedure.[11,12]

Other similar and more costly imaging techniques are available, such as magnetic resonance angiography (MRA) or computed tomographic angiography(CTA). However, they both have their limitations as well, particularly with the high cost and with excluding certain type of patients. Due to the magnetic field involved in MRA any patients with claustrophobia, pacemakers or other implants cannot be assessed.[11] CTA involves all the risks already stated above for angiography but it also exclude patients with renal insufficiency, hence it can end up excluding individuals with diabetes.[11]

These complex imaging techniques are mostly used in high-risk cases, like critical limb ischemia and ulcers.[8] Guidelines indicate the usage of certain screening tests, mostly involving methods that are not as costly, such as pressure measurements and Doppler ultrasonography.[8] Although there have been studies[11,12] disputing pressure measurements such as ABI due to its limitations, guidelines given to the NHS by the National Institute for Health and Care Excellence[22], are advising the use of ABI and Doppler probe during PAD assessment.

Therefore, only procedures that have certain limitations are used at the early start of the investigation, producing a high risk of PAD development in a short time, without leaving much possibility for action to be taken.

1.2   Skin Optics

Tissue optics and the way light interacts with biological tissue is a subject that has been thoroughly researched along the years. Tissue optics has aided particularly in the development of medical imaging technologies and treatments.[23–25]

When a medium such as skin is exposed to light, the latter can be reflected or transferred through the surface of the skin. The interaction between skin and light causes the light to be propagated in a different direction, reflecting it back into its original medium. Light reflection from skin surface is highly dependent on different refractive indices and the light's angle of incidence. These structural differences are also involved in the type of reflection produced, either specular or diffuse reflection.[26,27]

When light penetrates the skin it experiences absorption and scattering as it travels.

However the process is proportional to the ability of the tissue to perform said events.[23–27]

Skin is formed of multiple layers and each layer contains components distributed across the tissue that have different optical characteristics. As observed in Figure 1.2, the outer skin is mainly formed of epidermis, dermis and hypodermis. It is mainly the dermis and hypodermis that contain the vascular tissue.[1,2,13,25]

Chromophores are any elements from within the tissue that have the ability to absorb light.[24] Depending on which skin

Figure 1.2: Skin layer diagram, displaying the vascular tissue present in the dermis and the hypodermis.[2]

layer they are part of and the wavelength region they interact with, some chromophores will be stronger than others.[23,24,28] For the purpose of this research, the wavelengths used and analysed are part of the visible (VIS) wavelength region.

For the visible range the strongest chromophores in the skin are melanin and haemoglobin. Melanin is part of the outer layer of the skin, the epidermis, being present in the top 50-100 μm of the layer, but its absorption is known to be higher in the UV (ultraviolet) region.[13,26,28,29] Blood however, is predominantly found in the middle layer, the stronger chromophore being haemoglobin and therefore delineating the optical absorption characteristics of skin dermis. Haemoglobin can be found in the dermis as oxygenated haemoglobin (oxyhaemoglobin) and deoxygenated haemoglobin (deoxyhaemoglobin), at generally 50-500 μm underneath the epidermal surface.[13,26,28,29]

Although the following would need their own specific section to be fully understood, there are other less significant chromophores for the VIS region, such as carotene and bilirubin, lipids etc. It is also worth mentioning that in the visible region, water does not contribute substantially to the absorption of light. Water and lipids are strong chromophores in the near infra-red wavelength ranges in the dermis, where less scattering occurs, therefore facilitating a higher depth of light penetration.[13,26–28]

Studies on the absorption and scattering coefficients of skin layers have demonstrated that the epidermis presents a higher level of scattering than the other skin layers, due to melanin exhibiting higher optical properties.[13,26–30] In the VIS range in dermis, it was shown that haemoglobin is the main chromophore, with a rapid decline in absorption after 600
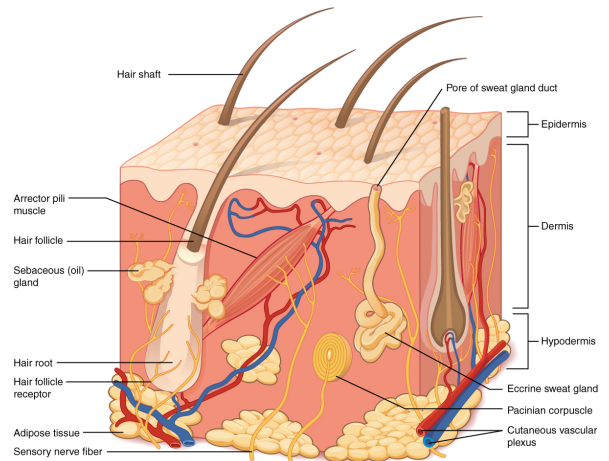
nm.[26,30,31] Scattering is also a factor which highly influences and can limit the depth of light penetration. High scattering and absorption levels can limit the penetration depth of light, therefore wavelengths under 600 nm (such as blue and green) do not tend to surpass 2 mm in depth. In the VIS range haemoglobin display absorption peaks in the blue and green wavelengths.[26,27,31]

Absorption spectra between fully oxygenated haemoglobin (O_2Hb) and fully deoxygenated haemoglobin (presented here as Hb, however the rest of the thesis will refer to it as HHb) has been recorded and tabulated as shown in Figure 1.3.[26–28,31,32] The spectra illustrates the wavelengths at which there is no change in the absorption coefficient of haemoglobin, namely the isobestic wavelengths; versus the wavelengths that display a range of differences between the two extinction coefficients.[31,32]
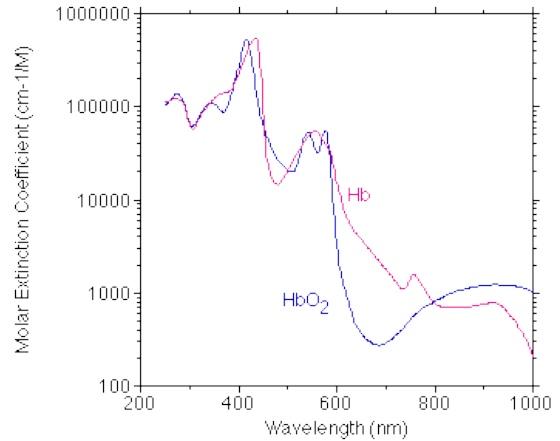

Figure 1.3: Absorption spectra of oxygenated haemoglobin (O_2Hb) and deoxygenated haemoglobin (Hb). Data tabulated and figure created by Prahl, 1999.[32]

Skin is considered a heterogeneous tissue that displays optical spatial variations across its structure. Therefore whenever light encounters one of these differences in the refractive index, high optical scattering takes place.[23,24,33] Most light that is not absorbed, will be reflected of the surface of the skin through multiple scattering.[23,26–28] The reflectance level, will therefore be in strong correlation with the amount of light that is absorbed by chromophores, leading to various options of imaging techniques for reflectance detection.[23]

1.3 Hyperspectral and Multispectral Imaging

1.3.1 Significance

Both hyperspectral (HSI) and multispectral (MSI) imaging, are methods used to measure the reflectance of the surface of interest; this is determined by collecting the spectral information given by the reflected incident light of a surface.[6,23,33–35] Hyperspectral and multispectral imaging are the result of the combination of digital imaging and spectroscopy, collecting two-dimensional images in series over certain wavelengths.[23] The set of images generated is a

three-dimensional dataset known as a hypercube. A hypercube provides spatial and spectral information, forming a spectral signature for every pixel in the image, each being connected to their neighbours. [6,23,34]

The difference between HSI and MSI, resides simply in the number of bands used, however both techniques have been used in medical imaging. MSI creates two dimensional images for a preselected number of specific wavelengths, whereas HSI collects data for a larger, continuous wavelength range. [6,35–37]
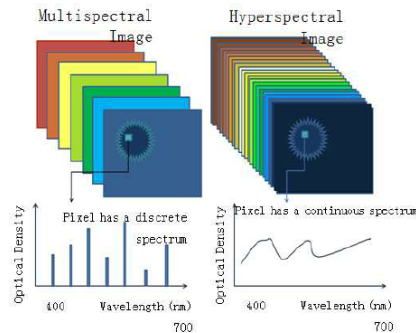

Figure 1.4: Figure generated by Aboras *et al.* [37], displaying a comparison between the multispectral and hyperspectral imaging methods. [37]

Figure 1.4 displays a general side by side comparison between HSI and MSI and how the spectrum for each pixel is depicted. [37] HSI presents a continuous spectrum at each wavelength from the chosen range, therefore being more sensitive to changes, whereas MSI produces data on a limited number of chosen spectral bands, hence focusing only on the data obtained from the applicable wavelengths. [6,35–37]

Hyperspectral imaging was initially mostly used in remote sensing applications, such as soil mapping and monitoring [38], and only later it was investigated by other fields of study. [39,40] HSI now has application in many other departments, such as the pharmaceutical industry [39], food industry [41], forensic science [39,42], cultural heritage [43], medical science and others. [23,39]

The application and research of HSI/MSI in medical science has been branching out in various sectors of the field, particularly due to the ability to collect data with an increased precision and produce a non-invasive diagnosis. However, even though research in the field has increased in the last decade, the technique is new and requires additional validation before applying it to a real work environment.

Surgery is considered to be a dangerous procedure that depends mostly on the skills and expertise of a surgeon. Hyperspectral imaging has been found to be extremely helpful when used in surgery to visualise tissues. HSI/MSI does not only have the ability to provide clearer images, but can also potentially present images that cannot be visualised under the naked eye as they are under blood. [44] It has been proposed that the technique has the capacity to support the surgeon in finding and making a distinction between veins, arteries and any anomalies present. [45]

Other than surgical guidance, hyperspectral imaging has been applied for the identification of residual tumours during surgery. This is highly beneficial for cases where the tumour has been resected, without being able to examine the possibility of any residual left.[23,46] In Panasiuk's[46] research, the technique not only identified and differentiated tumours but also other different types of tissue, such as muscle, connective tissue and blood vessels.[23,46]

The application of HSI during surgery has the ability of increasing the rates for complete resection, and lead to a better preservation of the organ as well as a better health condition for the patients.[23] The majority of research involving this technique has been done for surgery guidance or even focused on identifying dental carries, although this has not been investigated enough to be validated.[40] However, most of the research regarding HSI/MSI is non-invasive and focuses on skin optics and tissue oxygenation.

As mentioned previously, when light enters a biological tissue, it will absorb but also scatter across the tissue. Blood and melanin are known to be significant chromophores for visible wavelengths. Variables observed in optical properties of the skin can be investigated through its reflectance signal, which is affected by the structural and biochemical characteristics of the tissue.[23] Therefore, the light absorbed, transmitted and reflected from the tissue will change if a disease is present and advancing. Hyperspectral/multispectral imaging is capable of monitoring those changes and acquire data about the tissue pathology.[23,31]

The dominant chromophore in blood is haemoglobin, which has the role of carrying oxygen across the body. Oxygenated haemoglobin (oxyhaemoglobin) can be affected by certain diseases in such a way that it will make the oxygen detach itself from the haemoglobin (deoxyhaemoglobin), leading to changes in the optical absorbance and reflectance properties. Recording the tissue oxygenation at more wavelengths, will determine the level of blood flow within the area and present more information about these changes.[23,31] Being able to detect changes of the blood flow within the vascular system, can eventually lead to early diagnose of diseases such as PAD.

1.3.2 Application of MSI and HSI in Tissue Oximetry

As mentioned previously, the hypothesis of which MSI and HSI are based on, consists of an oxygen saturation (SO_2) measurement of the tissue area in interest. In order to measure the SO_2, the oxygenated haemoglobin (O_2Hb) and the deoxygenated haemoglobin (HHb) have to be known.[31,47] The SO_2 calculation is based on Beer-Lambert's Law at two wavelengths, out of which one represents the isobestic point, where there is no change in the reflectance

between O_2Hb and HHb; whilst the other represents the wavelength with the highest ratio between O_2Hb and HHb. However most research and instruments were performed within a large range of wavelengths, mostly depending on the depth of the tissue.[23,31,40,47,48]

The fundamental form of the equation used to determine SO_2 is:

$$SO_2 = \frac{C_{O_2Hb}}{(C_{O_2Hb} + C_{HHb})} \tag{1.1}$$

where C_{O_2Hb} and C_{HHb} are the concentrations of the oxygenated haemoglobin and the deoxygenated haemoglobin.[49–52]

From Equation 1.1, there are other derivatives that can be formed, taking into consideration the extinction coefficients of O_2Hb and HHb and their known or unknown values. This is specifically dependent of the type of research that is conducted and the final aims.[47]

HSI and MSI have a large literature background for a variety of applications. The spectral range used is fundamental for further research, however there are also many variables influencing the range used, such as tissue depth, the instruments used and the final objectives (Table 1.1). Table 1.1 illustrates a summary of some of the ranges used in literature. The 'Isobestic λ' and the 'Largest Difference λ' are shown if the respective study has stated the wavebands or graphically displayed them.

HSI/MSI has an immense potential for further development and implementation in the medical field. In the past decades, there have been some novel, state of the art devices and techniques with HSI/MSI produced. HyperMed Inc, USA[53] has produced a portable, hand-held imaging instrument, which determines oxygen saturation through the use of HSI. Currently, there are studies that have used the instrument to validate its functionality in the medical environment with successful conclusions.[6,54–57] However, due to the components used to build the device, its novel state and the cost-benefit relationship, the instrument is unlikely to be procured by the NHS.

Secondly, advances have also been seen when combining HSI with other imaging methods. An example of this consists of the studies that have been made, when using optical coherence tomography with HSI for a more in-depth tissue information and topography.[58,59] Furthermore, another portable novel device was created, which uses the same tissue oxygenation principles as a printed organic reflectance oximetry configuration that can measures the reflected light from the tissue.[60]

From the short overview of the contemporaneous methods used in medical care (Section 1.1.3), it can be easily seen that new detection methods are needed. Methods that are not as

costly, non-invasive, provide real-time data, more time effective and that clinicians can use in the clinic as well as for any home visits. HMSI requires more clinical research for validation, together with an instrument that can fulfill the previous requirements.

The research described during this thesis, focuses on creating a new MSI instrument that is portable, hand-held, less costly and which has the ability of early stage detection and monitoring of vascular diseases in the lower limb.

Table 1.1: Short summary of some wavelength ranges used in literature for tissue oximetry and their applications. 'Isobestic λ' represents the point with no change in reflectance between O_2Hb and HHb; whilst the 'Largest Difference λ' represents the opposite. If known, the values were taken from the respective studies together with the waveband range. Some studies only mention the range used.

Study	Spectral Range (nm)			Application
	Isobestic λ	Largest Difference λ	Range	
Wang *et al.*[47]	573	-	550 - 1000	Blood vessel imaging
Akbari *et al.*[45]	-	650 - 700	400 - 1000	Blood vessel imaging
Rubins *et al.*[51]	450 - 500	650 - 700	450 - 800	Oximetry changes during vascular occlusion
Bruins *et al.*[61]	-	-	400 - 600	Oximetry changes during vascular occlusion
Bashkatov *et al.*[13]	-	410, 540, 575	500 - 2000	Tissue oximetry
Gillies *et al.*[62]	-	560	500 - 600	Shock and resuscitation
Chin *et al.*[63]	-	-	500 - 660 every 15 bands	Irradiated tissue oximetry
Yudovsky *et al.*[64]	-	-	550 - 660 every 15 bands	Diabetic foot ulcer
Akbari *et al.*[65]	-	-	450 - 950	Prostate cancer
Clancy *et al.*[66]	-	-	500 - 620 every 10 bands	Bowel oximetry

Chapter 2

Method Development

2.1 Instrumentation

The multispectral greyscale camera used was developed in collaboration with Buzzard Cameras Limited, Figure 2.2. The camera has four lenses on top of which a filter mount can be attached. The mount acts as a filter holder for each of the filters available, making the filters interchangeable. The connection between the camera and a computer was easily achieved by four HDMI cables. The four-band camera has a spectral range from 500 nm to 650 nm, with a full-width-at-half-maximum (FWHM) of 10 nm.

A heavy load capacity camera stand was used to support the camera, as it can be observed in Figure 2.1.

The camera set-up has 16 attachable filters available in the visible range: 500 nm, 510 nm, 520 nm, 532 nm, 540 nm, 550 nm, 560 nm, 568 nm, 580 nm, 589 nm, 600 nm, 610 nm, 620 nm, 632 nm, 640 nm and 650 nm. These are the wavelengths at which the images were collected for further analysis.

Figure 2.1: Heavy duty extendable camera stand, for image collections.

The light source used for the acquisition of the images was a magnifier lamp with 90 white light-emitting diodes (LED) and an intensity of 1600 mcd/LED.

During initial tests the lamp was illuminating the sample from an oblique angle, whereas for the following trials the lamp was attached to the camera by removing the magnifying
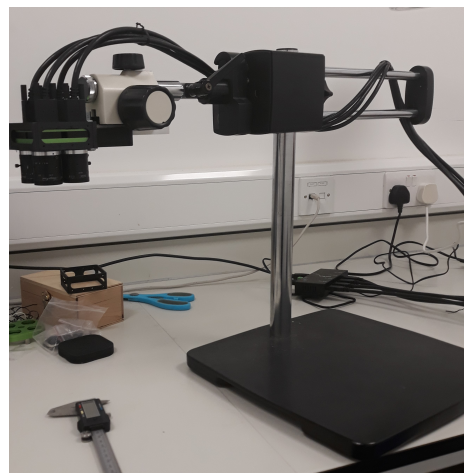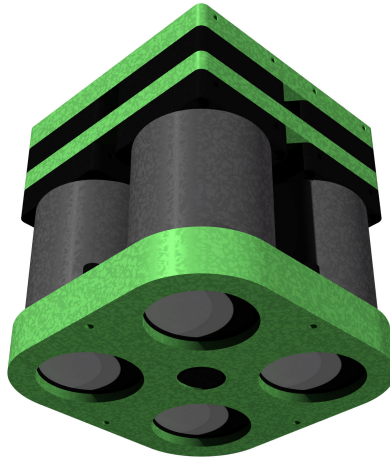
(a) Camera.

(b) Camera with filters detached.

(c) Camera with filters and cables.

Figure 2.2: 2.2a Camera developed with Buzzard Cameras Limited. 2.2b Each of the four cylinders attached to the bottom green frame is a lens, with an individual rotating mechanical focus ring. The filters are attached to the lens with the green filter mount displayed next to the camera. 2.2c There are four HDMI cables that connect to each camera lens, while the other side connects to the computer.

glass from its centre. This set up can be observed in Figure 2.3.

After the presumptive tests, in order to be able to achieve different oxygenation results, arterial occlusion was performed. This was used as a method to imitate the effects of PAD on the arteries, and therefore reduce the oxygenation levels during occlusion.

The apparatus used for the arterial occlusion was Welch Allyn Durashock DS66 Sphygmomanometer. The sphygmomanometer is a manual aneroid blood pressure metre, that utilises an adult cuff and a gauge display with an inflation bulb. For the presumptive tests, a UV-visible spectrometer has been used together with Fisherbrand™ Polystyrene Macro Cuvettes for Visible Wavelengths. Blanks were run between each trial.
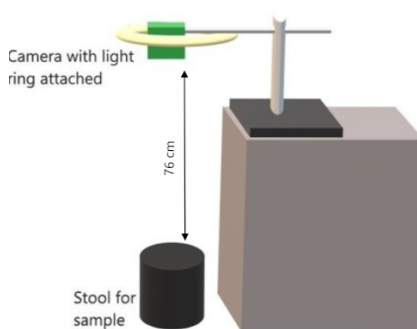
Figure 2.3: Instrument set-up used to acquire images for offset calibration, initial and final samples.

XIMEA CamTool V2.07 was the software used for histogram extraction of the presumptive tests in addition to the image acquisition of all trials. Images were initially captured with the default exposure setting of the software, while the final sets collected had a set exposure of 43.74 ms. Images were exported in a TIF and BMP format. For all the calibrations, image processing related analysis and resulted graphs, MathWorks MATLAB *ver. R2019a* was used.

2.2 Preliminary Tests

One of the first hypothesis considered was concerning the different illumination environments and the effects that these could potentially have on the data collected by the camera. On the grounds that in real life clinical illumination backgrounds are extremely unpredictable, the commencement of the initial tests was performed in a dark room. Acquiring data in a dark room implies a controllable environment at the start, which opens the possibility of a lighting system, that during the beginning of the trials aids in controlling any lighting variables. After using a dark room for the preliminary tests, the environment setting can gain more lighting variables, such as testing the data collection in a laboratory environment and then outdoors, until finally reaching a real-life clinical environment. That being said, the fact that all samples cannot be collected concomitantly, leaves space for variables to arise between sample collections, such as change in illumination and in the position of the sample, hence potentially decreasing comparability.

The hypothesis for which the preliminary tests are based on, was to examine the functionality of the camera in conjunction with the filters. Figure 2.4 display the process taken to test and calibrate the camera. The first procedure consisted of the preliminary tests, which have the objective of confirming that the camera can detect reflectance by comparing it against the absorbance spectra of the same samples. Secondly, the image offset for the four cameras was calibrated and the then the images were flat-field corrected. The calibration setting and method are explained in the following section.

The tests were carried out using distilled water and five different food colours as samples. The food colours used were from PME's range Concentrated Natural Food Colouring: red, green, blue, yellow and orange. For the test samples to be produced, a 1:100 dilution of each
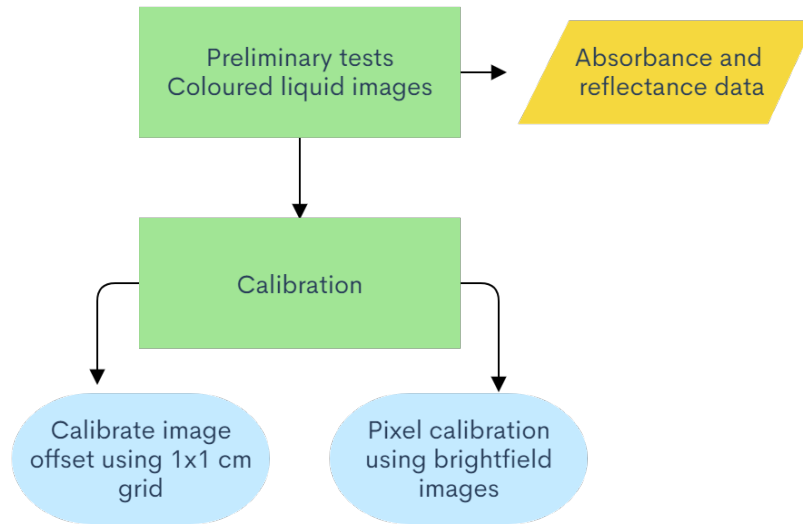
Figure 2.4: Schematic process for the preliminary camera test and calibration. Starts with the preliminary tests, which confirm the ability of the camera to detect tissue reflectance. Secondly, the calibration tests were performed.

colour with distilled water was performed. Images were then acquired of each colour with all the different filters. The filters were grouped in an ascending order, starting with the 500 nm wavelength and ending with 650 nm. They were then swapped after each image was collected by removing the filter mount of the camera and replacing the filters with the following batch.

Examining the functionality of the camera and testing its limits, started by looking at how the samples used absorb or reflect light. The ability of the surface, in this case the coloured liquids, to absorb or reflect light is of paramount importance for the final results. Light can be absorbed, transmitted or reflected.[23] Depending on specific chromophores contained by the surface in question, light at a certain wavelength will be absorbed by the sample, whereas other wavelengths will be reflected. The colour perceived by the camera is the reflected light.[23,24] This
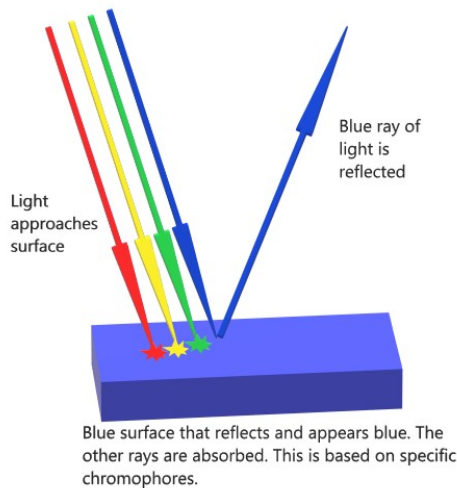
Figure 2.5: Diagram showing absorption and reflection of light depending on surface.

process is schematically explained in figure 2.5.

As a result of this, two methods were used to analyse the coloured liquids. First method uses the image acquisition software to collect the images of the liquid from the Petri dish and extract the histograms needed for pixel intensities. Hence, through this type of analysis, the

measurable element is reflection.

Due to the camera having four lenses which overlap on a certain region in the images collected and the offset not being calibrated yet, only the area of interest that appears in each image was chosen. This area has the following coordinates: x-axis = 498, y-axis = 367, 205 x 185 (width x height). The extracted values from this previously defined area, consisted of the greyscale intensity value for each pixel within it. The values were then multiplied and all the results added together, producing the total intensity value of the area selected for that particular wavelength. In this case the pixel intensity represents the total reflectivity for that particular region.

The repository link for the raw images of the coloured liquid can be found in Appendix .1.

The second technique examines the absorption of the same samples with the use of UV-VIS, in a continuous range of 400-700 nm. The spectra resulted from the UV-VIS analysis was incorporated together with the data collected from the pixel intensities.

Figures 2.6 and 2.7 display all the final profiles of absorption and reflectivity data for each color. Each colour is absorbed at a certain wavelength, where its reflected fraction will drop significantly. This is to be expected based on the theory explained above. If light is absorbed, then it will not be reflected as much and vice versa.
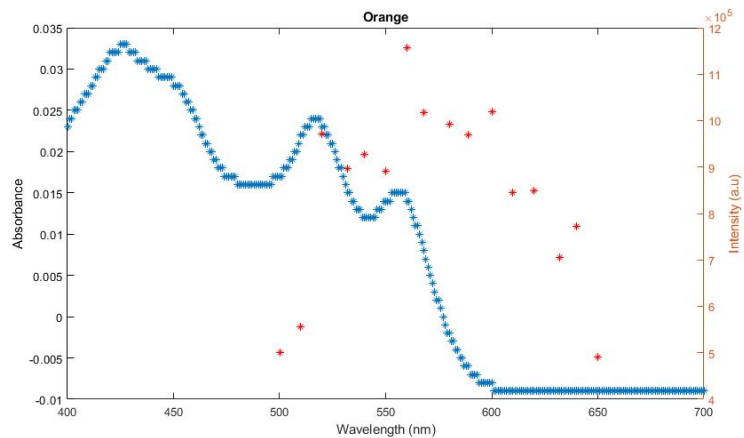
As depicted in figures 2.6 and 2.7 below, the reflectance and absorption spectra compatibility, confirmed the high functionality of each wavelength filter, making them suitable for the continuation of the project.
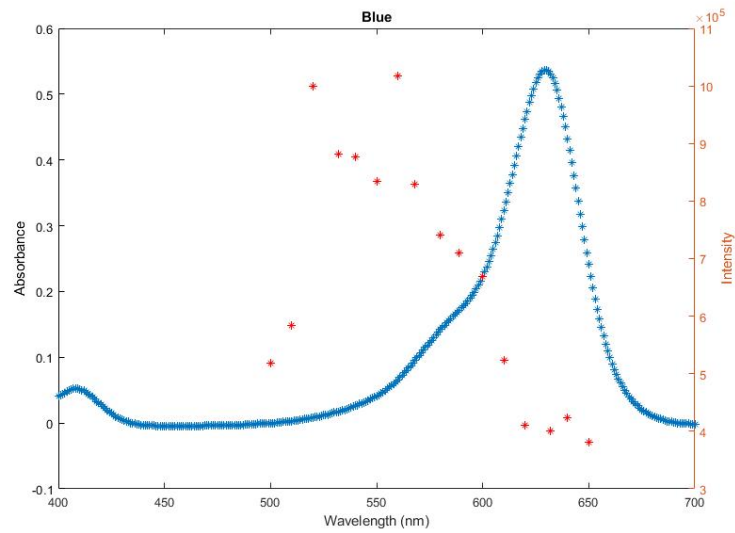
(a) Blue colouring profile.
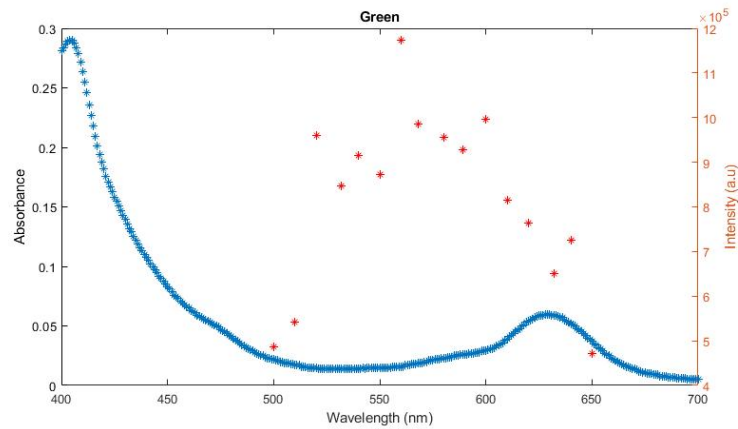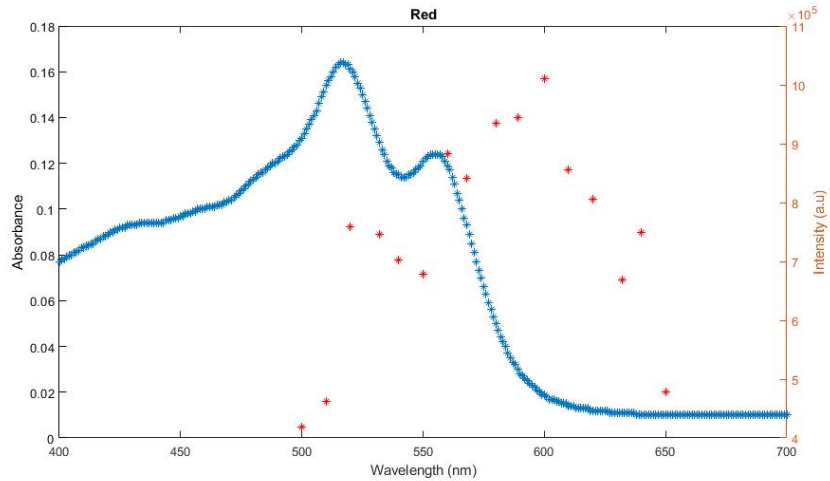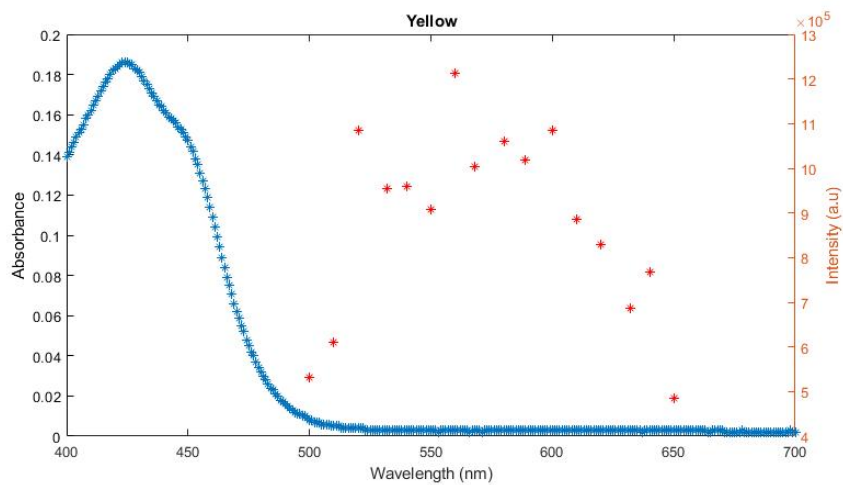

(b) Green colouring profile.

(c) Orange colouring profile.

Figure 2.6: Absorption and reflection profile of blue, green and orange liquids. It can be seen how whenever there is an increase in the absorption peak, the reflectivity in the same wavelength drops. The blue dots represent the absorbance, whilst the red stars represent the reflectance profile from the pixel intensities.

(a) Red colouring profile.

(b) Yellow colouring profile.

Figure 2.7: Absorption and reflection profile of red and yellow. It can be seen how whenever there is an increase in the absorption peak, the reflectivity in the same wavelength drops. The blue dots represent the absorbance, whilst the red stars represent the reflectance profile from the pixel intensities.

2.3 Calibration

Calibrating the operating instruments used in any study has an outstanding importance in diminishing all analysis imprecisions and errors, thus culminating into a notable higher instrumental performance.

The previous section examined the performance of the camera with the filters, proving its functionality in detecting reflectance. The rest of the practical work regarding the calibration process was executed in the dark room as well. Three different calibration methods were discussed initially in order to achieve the best results, as seen in Figure 2.4: image offset and overlay, pixel calibration and wavelength calibration. The latter was already performed by the distributor, with a result of Full–Width-at-Half-Maximum (FWHM) of 10 nm.

2.3.1 Pixel Calibration

The pixel calibration was performed using two approaches: bright and dark field corrections. This aided in visualising the pixel response and saturation for the specific environment, making sure any non-uniformities were eventually corrected.

In order to calibrate using bright field correction, multiple images were taken of a white A3 paper sheet, using the camera with no filters attached. The control room was illuminated normally and the lamp was turned on as well, but it should be mentioned that the light was not pointed directly at the sample to avoid any over saturation.

The A3 paper sheet was virtually divided into 12 parts, hence each of the four cameras has collected 12 images. The diagram from Figure 2.8 presents the pattern that was followed when acquiring the calibration samples.

Subsequent to the collection of the images, MATLAB was used to plot the intensities of each bright field image, which was later used to correct the data of the first trial samples.

1	4	7	10
2	5	8	11
3	6	9	12

Figure 2.8: Pattern used when images for Bright field correction were acquired.

```
% Sum of each pixel in array
Exmean{j} = plus(Exmean{j},S(i).data);

% Divide by total images to create mean for each channel
Exmean{j} = Exmean{j}/length(ExPosSurf);
```

Figure 2.9: Code for performing an average on bright-field data.

The 12 images from each camera were collected and their pixel intensities were imported into arrays, making it eventually easier to develop mean values. The following steps (observe Figure 2.9 for code) consisted of summing each pixel value in the array for each camera and then divide the result by the number of pictures, hence an average value for pixel was obtained.

The values for each individual image, as well as the intensities for the resulted averaged image were plotted in a surface plot (Figure 2.10). A few spikes are visible in each camera, with the highest ones in camera one, indicating dead pixels, which will later be corrected with the help of these averages. However, the overall response of the pixel values recorded is in concordance with the environment from which the images were taken, a highly bright sample.

The individual images and their respective surface plots can be found through the link in Appendix .2.

(a) Camera 1.

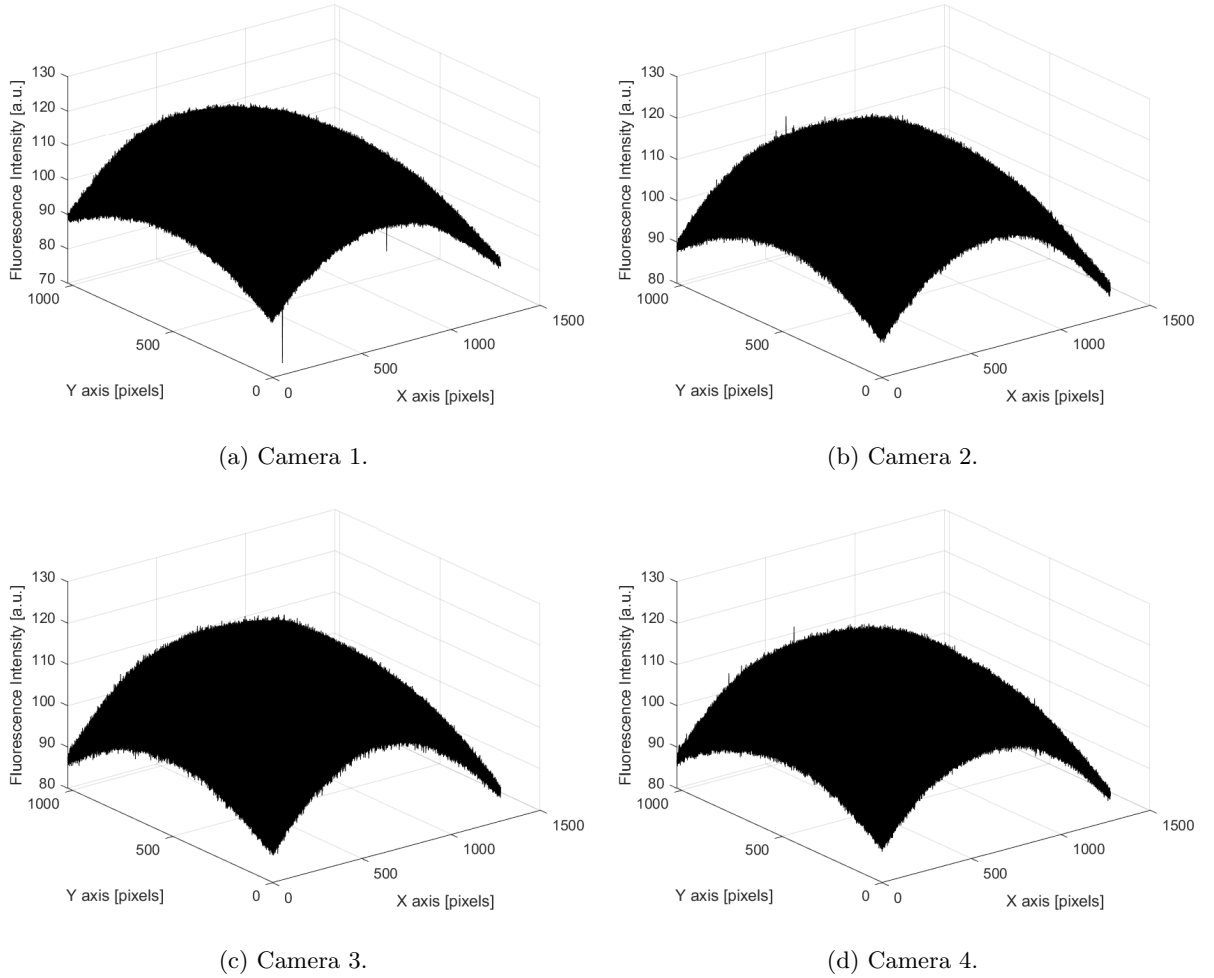(b) Camera 2.

(c) Camera 3.

(d) Camera 4.

Figure 2.10: Multiple bright-field images were collected for each camera. The mean intensity value of pixel response from the images of each camera was recorded and displayed through surf plots.

Additionally, the darkfield images were collected using the camera, although the lens caps were attached. The dark images were collected with the lens caps on, in the dark room. Due to the camera being an experimental model and its sensitivity also being tested by the manufacturers, no extra analysis was performed for the dark-field images at this point.

2.3.2 Image Offset

As mentioned previously, the Buzzard multispectral system is formed from four different cameras (Figure 2.2b) next to each other. This indicates a slightly different field of view for each of them, thus requiring a method of correction in order to be consistent and achieve best results. The overlay of the four cameras with each other can be seen in Figure 2.11.

As observed, there is an overlap area between the four cameras, which ultimately becomes the global region of interest for any subsequent analysis. The objective for this calibration part is to eliminate any parts from the analysis region that are not overlapped by all four cameras.

Starting with this part of the calibration, the following sample acquiring and processing occurred out of the dark room. The dark room was used for initial experiments before migrating to a open laboratory environment, without controllable lighting, for a closer step towards real life clinical application.

This part of the calibration process involved the employment of a 1x1 cm grid on a A3 paper sheet. Using the set-up displayed in Figure 2.3, images were again acquired without the filters attached to the camera lenses. One image was collected with each camera from the fix positioned grid. The images are available in Figure 1 from Appendix .3.

Figure 2.11: Visualisation of the overlap of the four camera lenses. Each colour and number represents a lens on the camera and their respective field of view. The overlap in the middle shows the only mutual area within the field of view for all four lenses, whilst the corners show the regions that belong to only that particular camera.

These four images were then evaluated and processed in such a way that the resulted method could be further applied in the initial development of any successive samples. The grid images were subjected to a MATLAB procedure called translation. This function has the role of yielding a product image from an original set of coordinates by assigning each pixel with respect to its original axis coordinates.[67,68] To clarify, in this case, the image from Figure 1a (from Appendix .3) was appointed as the main and original set of coordinates.
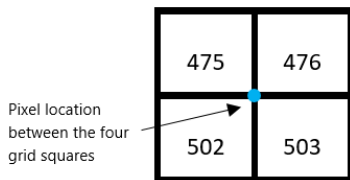

Figure 2.12: Pixel chosen for offset calibration at intersection of the four squares, numbered as displayed.

The position of one pixel was noted and then the relative distance to that pixel was established in the rest of the grids, hence finding the offset distance and resulting into a clipped output image.

The location of the pixel selected from the original grid image was arbitrarily chosen from one of the intersections between the squares of the grid. Figure 2.12 depicts the location of the chosen pixel on the grid of the first camera. The pixel has the cartesian coordinates of 732 on the x-axis and 555 on the y-axis, C1(732, 555). The next step involved the detection of the location of the pixels found at the same intersection in the other grids, followed by locating their coordinates.

For the second camera (Figure 1b) the location on the x-axis is 523 and on the y-axis is 544, C2(523, 544). The pixel of the third camera's grid (figure 1c) has the coordinates C3(739, 346), while on the fourth grid (1d) it has the coordinates C4(525, 342).
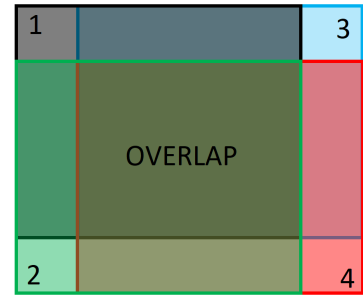
With this in mind, the distances required to reach the values of C1 in both axes were calculated for C2, C3 and C4. Figure 2.13 depicts how the translation function was used in order to acquire the offset calibration.

As explained above, the 'imtranslate' image translation function, will displace each pixel by a specific given distance in both x and y axes until it reaches the original coordinates, C1(732, 555). Thus, values were added or subtracted for each X-axis and Y-axis (C(X,Y)) as seen in Figure 2.13.

```
function [img]=OffSet(j,img)
if j == 2 %camera 2
    img = imtranslate(img,[209, 11]);
elseif j == 3 %camera 3
    img = imtranslate(img,[-7, 209]);
elseif j == 4 %camera 4
    img = imtranslate(img,[207, 213]);
end

% Final Crop
img = img(213:end,209:end-7); % Y X
```

Figure 2.13: Code used to perform translation on the camera overlay and isolate the global region of interest using the offset data.

Finally, all four images were cropped in order to discard any regions that are not being overlapped by all four cameras. The last line from the code in Figure 2.13 illustrates the method used to crop only the image overlap needed.

The following section further explains how these calibration methods were applied to the test samples prior to image processing.

2.4 Sample Acquisition

2.4.1 Preparation for Sample Acquisition

A formal ethical approval was sought, following the institution's standard procedures. As the only sample used at this stage in the process was the author's foot, a full application wasn't considered necessary. For any further clinical testing an ethical approval would be needed. Therefore, the sample used for all tests was the author's foot, having no previous or current known disease or illness, particularly with no effect on the cardiovascular system.

In order to be able to imitate the impact of a peripheral arterial disease, a Sphygmomanometer was used to obstruct the blood supply in the artery.[51,52,56,61,70] Arterial occlusion temporarily replicates the oxygen deficiency that would normally result in patients affected by the disease. With this in mind, it was important to identify the pressure at which there is no blood supply through the lower extremity arteries.

The occlusion pressure is based on an individual process not exceeding a certain artery pressure due to safety. Cuff occlusion leads to no blood being transported after the point of the obstruction, which in turn leads to the absence of pulse. Therefore, in order to achieve

the lack of pulse, the pressure point needed to be established.

Information regarding the guidelines for safe pressure limits when using a blood pressure cuff, has been discussed before in literature with the conclusion that the cuff should be inflated by minimum 30 mmHg extra after the cut off point of the pulse[71]. Additionally, inflated cuffs can be kept on the subject for even up to two hours in certain circumstances, without leaving any long term affections[72].

Being able to use a Doppler ultrasound for the correct arteries was crucial, not only due to it having implications in the results of the pressure points, but also in the images that were subsequently acquired, as the focus had to be on the correct arteries. The arteries in question can be observed in the Figures 2.14 and 2.15.

[h]

Figure 2.14: Dorsalis Pedis artery.[69]

Figure 2.15: Posterior Tibial artery.[69]

The aforementioned figures illustrate the positions of the most relevant arteries for which pulsations can be accurately determined in the lower extremities[69]. These particular arteries, together with the tip of the toes, are commonly used by qualified professionals in PAD investigation.

Carrying out this examination required the use of the Sphygmomanometer and of an ultrasound Doppler instrument; both of which were controlled by a specialist podiatrist from the National Health Service UK.

The right leg was positioned on a chair in a 90°angle to the body, the cuff of the Sphyg was attached to the calf of the leg and the Doppler was used on the relevant arteries. Initial examination of the arterial pulse started before the pressure was applied; this confirmed the arterial flow was in a desirable condition. With the Doppler still in position the cuff was firstly inflated to 120 mmHG, after which small increments were added until it reached 135 mmHg. At this point, the pulse started to slowly decrease in intensity. By the time the pressure reached 150 mmHG, the pulse stopped completely for both flexed and non flexed knee. Hence, the pressure used was 180 mmHg.

2.4.2 Sample Acquisition

Concomitantly with the acquisition of the grid images, the first test sample images were also collected, which helped keeping a consistent instrumental set-up as seen in Figure 2.3 and 2.16. In Figure 2.17, a schematic representation of the acquisition process for the samples
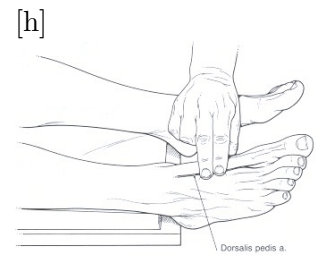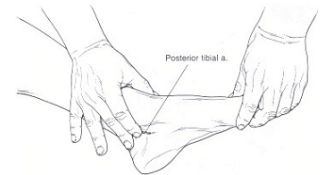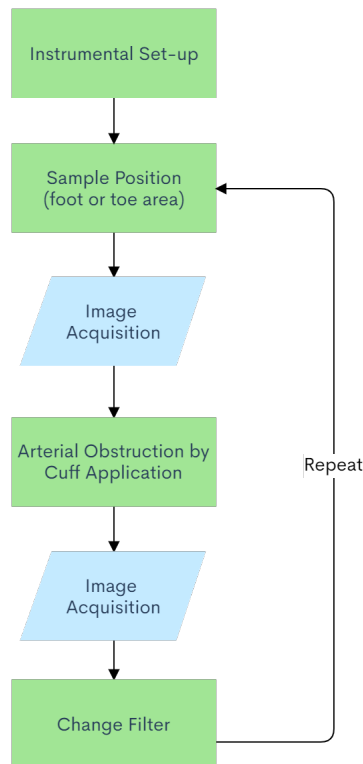
Figure 2.17: Schematic process of the acquisition of the initial samples, using cuff occlusion at 180 mmHg.

acquired is shown.

The first samples were collected, following the pressure point determined previously, with a cuff inflation of 180 mmHg. The images acquired were with the artery termination in the tip of the toes and the Dorsalis Pedis artery. The reason for this being that, with the current set-up (Figure 2.3), the tibial artery was not visible for analysis.

The camera was firstly focused on the toes of the subject however, the focus and therefore the field of view for these tests, was kept constant. In order to be able to also capture the Pedis artery in focus, the leg was raised by 8 cm whilst still being supported. As soon as each image was collected, it was then also exported in a TIF format to an external folder from XIMEA, from which it was subsequently imported into MATLAB. It is worth mentioning that the recommended saving format for spectral imaging is an uncompressed format.[31] Therefore both TIF and BMP can be used, however MATLAB's saving of matrices can sometimes slightly change pixel intensity values between for-
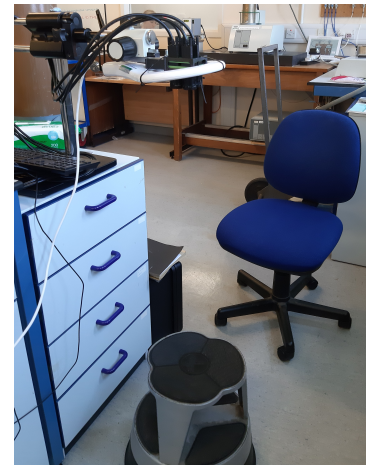

Figure 2.16: Laboratory set-up for image acquisition, as depicted schematically in Figure 2.3. Buzzard camera and lighting system were attached to the camera stand. A chair and stool were used for positioning the foot under the camera. The computer used to acquire the images was present as well and manually controlled from the chair using the keyboard.

mats. Both TIF and BMP will be used in this research, with TIF being a preferable option.

The initial set of samples further contributed to the development of an appropriate analysis technique.

All images acquired for all filters can be seen through the link in Appendix .5.

Chapter 3

Image Analysis

As the absorption spectrum changes, scattering of light will be influenced according to those changes. Measuring the tissue oxygenation through spectral imaging, is based on the application of Beer-Lambert Law(BLL) in a digital setting, hence detecting the light scattered back from skin, rather than absorbance. Establishing and applying the pixel intensity of a sample image into BLL, leads to recording the reflectance given by the skin in a specific area.[23,31,40]

When the image analysis technique is achieved, it determines the oximetry of a tissue in an automatic way, which aids in reducing human error processing and also becomes less time-consuming when subsequent testing is performed. In order to determine the oximetry, four wavelengths which display the smallest (isobestic wavelength) and biggest difference between the cuffed and without cuff images, need to be determined.

This chapter will describe all the code written in MATLAB as part of the method development phase of the research and its automatization. The first section of the chapter focuses on refining the images collected previously and subsequently have them undergo a series of processing and analysis procedures, which are explained in the later section of the chapter.

Figure 3.1 illustrates the image pre-processing and image processing procedures explained throughout this chapter and the following one.

3.1   Image Pre-processing

Image pre-processing has a pivotal role in the successful completion of any further investigation and analysis. It encases certain procedures that are implemented during the initial steps of image processing. The aim of these techniques is to calibrate and process data in such a way, that it ultimately yields a refined output image ready to be further analysed according to its aims.[73,74]
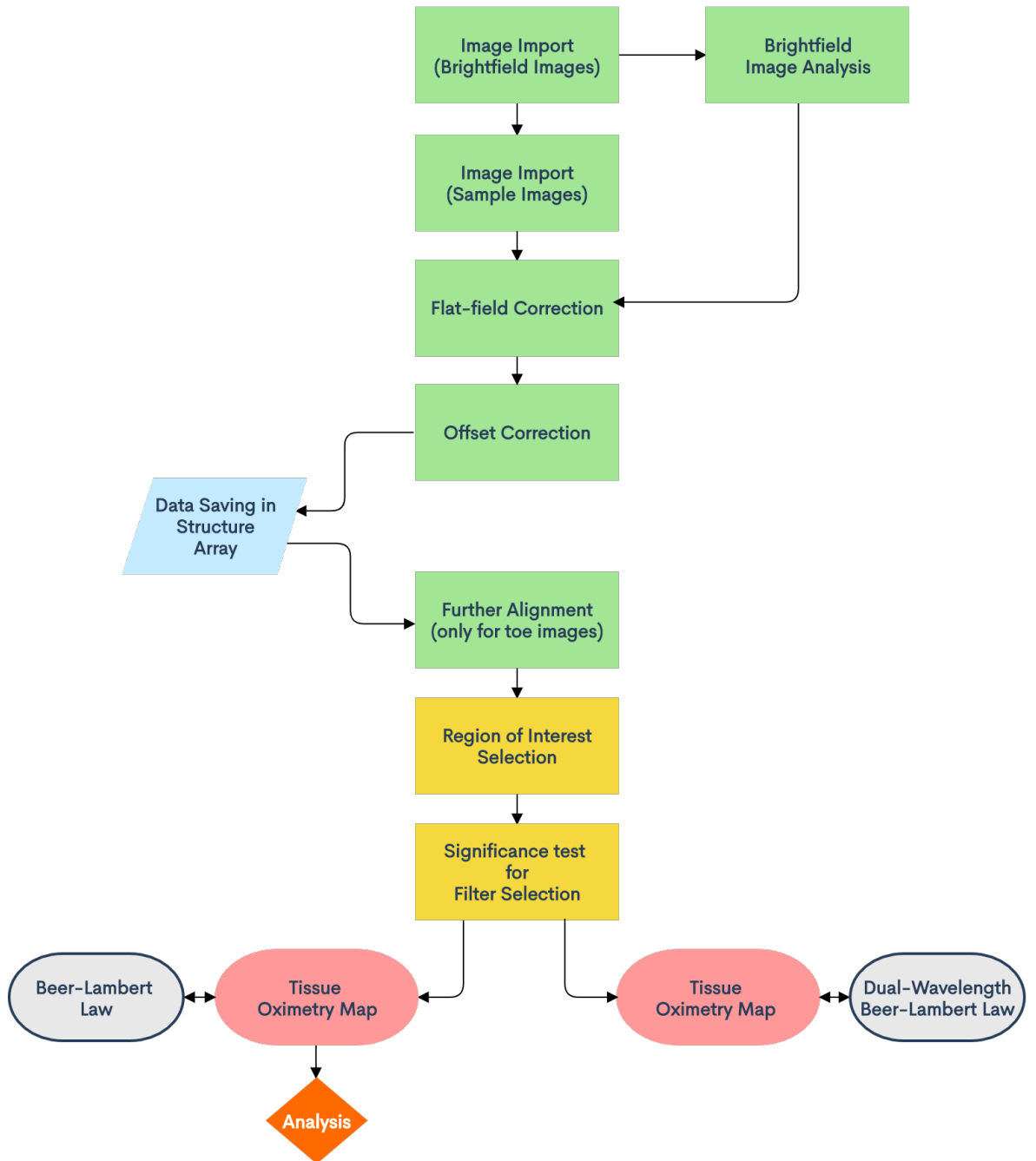
Figure 3.1: Representation of the image pre-processing and processing applied to the samples. Bright-field images were firstly imported into MATLAB and analysed regarding flat-field correction. The sample images were than imported into the software and the correction was applied for each image. The calibration process then continued by application of the offset data from Section 2.3.2. The images were then aligned again through an automatic MATLAB function for a more accurate overlay. During image processing the ROI were selected and analysed, leading to establishing four preliminary filters for further testing. Two oximetry methods were then performed, however only one reached an analysis point.

3.1.1 Image Import

It was unequivocal from the start of the process that many individual scripts, marking each analysis step, would be necessary in order to achieve the goal set. However, having to run many scripts one by one to complete the analysis procedure, would have been an unnecessary system that can also introduce human error. Thus, a central script was created to operate similar to a portal and execute each code program when required. The code in question can be seen in Appendix .4, Figure 2 and it illustrates the final version of the main code created with all the scripts and functions, generated throughout the image processing analysis in MATLAB. Using a title abbreviation, this main program will be further referred to as the NIPAD script.

The first script constructed for the processing of the samples performed a seemingly easy task, however it is of high importance for the following programs. The code focuses on importing all the images collected into MATLAB and it has the same general approach irrespective of the type of images that need importing, as long as it follows certain standards.

This is significant as the first process that took place before any other analysis, was to prepare the bright field images for flat field correction. Thus prior to importing the first set of samples, the images acquired for bright field calibration were also required. As a consequence of this, the written script for image import was operated for both sets of samples, starting with the calibration samples and then continuing with the cuff test samples. Although section 2.3.1 from the previous chapter described the approach used to analyse and process the calibration images, it did not highlight the process of importing and saving the data into MATLAB. The description of the following code will emphasise this procedure as well.

When executed, the code simply opens up a user interface window that allows the individual in charge to choose the folder that contains the data. Then it proceeds to search for all the files in the folder, that have a specific extension and an identifiable name.

As mentioned previously, this is a generic code, hence it can be transferred and used for similar or different scopes. However, the process of the Image Import function is still based mainly on the manner in which the images in question were

```
if exist('Tdir') == 0
    D = uigetdir(matlabroot,txt); % Get directory
end
S = dir(fullfile(D,'*.tif')); % pattern to match filenames.
```

Figure 3.2: Image import based on the file format given.

saved as in the chosen folder, after being acquired. In this case, all the images acquired using XIMEA CamTool, were saved as .TIF files. Once these were found the data was saved as a

structure array. Figure 3.2 depicts the lines of code for the preceding statement.

When the pixel calibration images were acquired, they were named in respect to the camera used to collect them. As explained in Chapter 2, each camera procured 12 images for flat field correction. Therefore, the name given to each image started with the number of the image (1-12), continued with the letter 'c' and ended with a number between 1-4 to identify the camera. For example, the first image collected with the first camera was titled '1c1', followed by '2c1' for the second image from the first camera, and so on.

On the other hand, when naming the images from the cuff trials, the process became slightly more complicated as none of the identifiable markers from this file, had to match with the ones from the calibration folder. The images captured could be virtually divided into four sets of samples: toes without cuff occlusion, toes with cuff occlusion, pedis artery (foot) without cuff occlusion and pedis artery (foot) with cuff occlusion. In addition to this, each one of these sections was repeated for all of the 16 filters.

With this in mind, the denomination for the samples commenced with the letter 'f' or 't', indicating which part of the foot the data is focused on; the pedis artery (foot) or the toe (t). It then mentions the wavelength of the filter for that specific image, proceeding with the letter 'b' (instead of 'c') and with a number between 1-4, which specifies the camera. This is different than previously to avoid any error or data overwriting during the execution of the code. The title finished with the presence of letter 's' or the lack thereof. This letter shows if cuff occlusion was performed or not for that particular sample. Again, the letter appointed for the indication of cuff presence, is not 'c' due to it being used for the bright field images.

To demonstrate, an image of the toes acquired at 500 nm from the first camera, with and without cuff occlusion, was therefore named: t500b1s and respectively t500b1.

It may seem irrelevant and ineffective to explain the nomenclature of any of the samples gathered, however it becomes extremely meaningful when expounding the lines of code, specifically aiding in repeatability. Because the code is used for importing both pixel calibration image and trial tests, as long as the marker in their names and their file extensions is identifiable, the data will be able to import and save accordingly.

Part of the loop used in the script to instruct the order of election during sample importing, is illustrated in Figure 3.3. Once the folder is chosen by the user, the code guides the software to choose the files that contain the letter 'c' in the title, characteristic to bright field images. Otherwise, if the letter does not exit, it will proceed to search for any files that have the letter 'b' in their name - specific for the test samples.

```
posC = strfind(S(k).name,'c');
    if isempty(posC)
        posC = strfind(S(k).name,'b');
    end
posTIF = strfind(S(k).name,'.tif');
ChNum{k} = S(k).name(posC:(posTIF-1));
    if strfind(ChNum{k},'b')
        ChNum{k} = ['c' ChNum{k}(2)];
    end
    if k == numel(S)
        C1pos = find(ismember(ChNum,'c1'));
        C2pos = find(ismember(ChNum,'c2'));
        C3pos = find(ismember(ChNum,'c3'));
        C4pos = find(ismember(ChNum,'c4'));
    end
end
ChPos = {C1pos;C2pos;C3pos;C4pos};
```

Figure 3.3: Loop used for image selection, depending on file nomenclature.

The last part of the script (Figure 3.3) was assigned to distribute the images into categories, simplifying data access for further analysis.

However, prior to this a specific task was operated for the test trials - if 'b' was present in the file name, the letter was eventually replaced with 'c'. The reason for this lies in the way subsequent scripts were written, but also in the fact that it was easier for data saving in MATLAB.

After this was accomplished, images were split into channels based on the camera they were collected with. The names for each channel were also given in relation to the camera used: C1pos represented all the images collected with the first camera, C2pos represents the second camera and the same for C3pos and C4pos together with their corresponding cameras.

The full script can be seen through the link in Appendix .4.

3.1.2 Flat-field Correction and Image Offset

Once the bright field images have been imported into MATLAB, the process explained in section 2.3.1 was pursued. The previous chapter depicted the development of a pixel calibration process, which was subsequently applied to the acquired bright field images in order to achieve a data correction control for the trial tests. After the bright field images were imported and the surf plots were created (Figure 2.10), the Image Import function was executed again. This time, the folder containing all the trial samples was chosen to be imported into MATLAB.

Following this, the results from the mean bright field data of each camera, were applied to all the images gathered during the sample cuff tests. The process in essence was considerably straightforward. For each channel created, namely for the images of each camera used, the

procedure seen in Equation 3.1 was employed.

$$ImagePixelCorrected = \frac{ImagePixel}{\frac{max(MeanBrightfieldPixel)}{MeanBrightfieldPixel}};\qquad(3.1)$$

where 'ImagePixel' represents each pixel in the sample image, 'MeanBrightfieldPixel' represents the intensity of the pixel in the final averaged bright-field data and 'ImagePixel-Corrected' is the flat-field corrected output.

The maximum value from the mean intensity data of bright field images, was divided by the intensity of each pixel in every position of that specific mean bright field data. The result of this division was then further used to perform a flat field correction on all the sample images collected. The intensity of each pixel's position from each image, was therefore divided by the result of the above-mentioned division, leading to correction of any over-saturation present. Flat field correction also removes any camera to camera variance that might exist, hence normalising the acquired data from all four cameras.

Figure 3.4 illustrates the before and after images of two images collected, one for toes and one for the foot area. The left image is the original one, while the right image represents the corrected one. It can be seen how the code slightly corrected the over-exposure of the image, normalising the data.

Following the correction, the resulted images were saved for additional analysis. However, during this final step an issue was encountered. When saving an image from MATLAB externally, regardless of its extension or the type of processing performed in the software, the pixel intensity of that particular image increases. While searching for a reason and means to overcome this concern, it became apparent that the change in intensity occurs when the image is saved externally from MATLAB and then imported back into the software.

Therefore, the decision was made to create a structure array and save the data within MATLAB as well. When verifying the pixel intensity variation it was found that there was no increase in the intensity value. Thus, as long as the image was stored within MATLAB and for any further procedures the data used was the one from the software, then the samples were safe of any automatic altering of its values. For the purpose of this thesis, the method development process was not affected much by this, with the exception of having to create the data storage space within Matlab. However, this could have an effect on any subsequent research, particularly if additional software would be needed in conjunction with Matlab and if data exports would be required.

At this point during pre-processing, the sample images have been flat field corrected
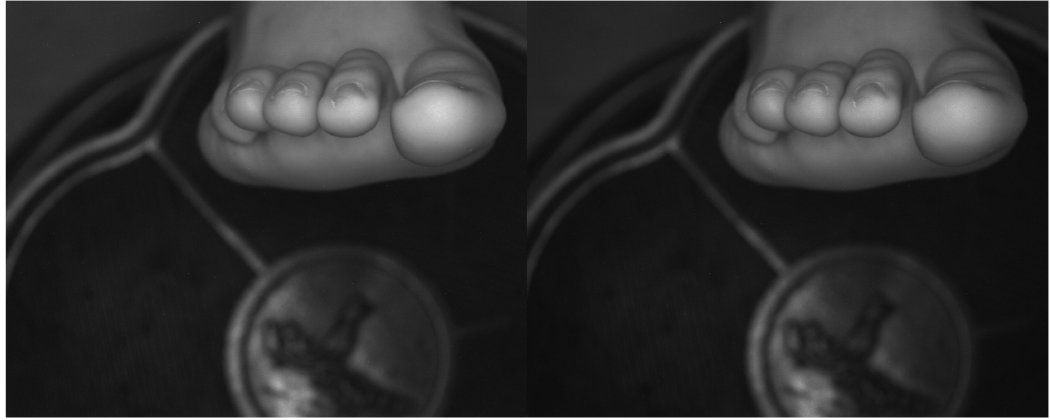
(a) Image taken at 640 nm with cuff.
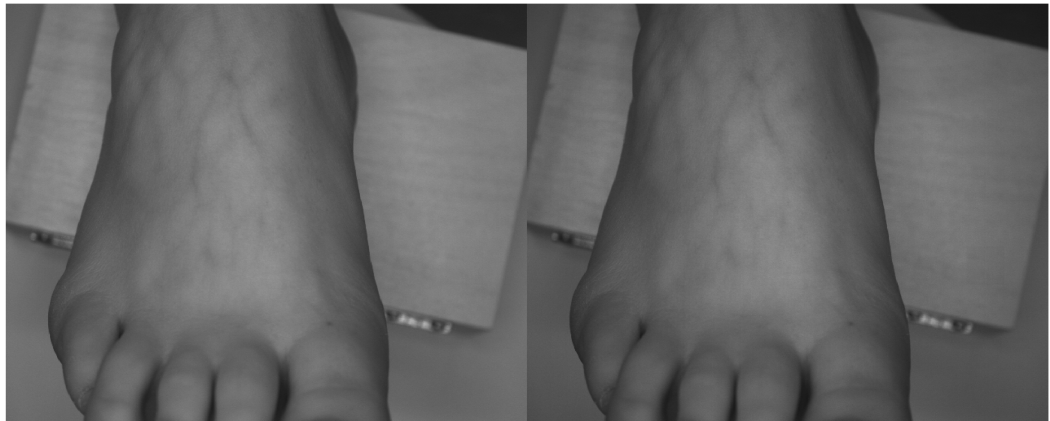
(b) Image taken at 610 nm with cuff.

Figure 3.4: Before (left images) and after (right images) flat-field correction image comparison. The correction in the exposure is visible in the areas that were very bright.

and stored in an array in MATLAB. To complete the calibration process, the image offset explained in section 2.3.2 was applied to the test trials. No adjustments were made to the method used, besides the fact that the sample images were the ones being corrected instead of the 1x1 cm grids. The data from images aligned with the offset correction was also exported in the MATLAB array, as well as being saved externally for visualisation purposes.

The full script can be seen through the link in Appendix .4.

All images that were flat-field normalised and calibrated for the offset, for all filters, can be seen through the link in Appendix .5.

3.1.3 Further Alignment

When examining the data from the cuff tests, it immediately became apparent that the position of the foot throughout the images was not the same. An instinctual movement of the foot was occurring whenever there was cuff occlusion involved, making it impossible for the

person who is cuffed to keep the foot completely still. Therefore, although the images underwent a certain degree of alignment through the offset calibration, there was a prerequisite for additional adjustment.

There is an overall lack of overlay, which could have potentially become a challenge when processing the samples. The misalignment can be seen in Figures 3.5 and 3.6, which depict images from the tests, taken one after the other, with and without cuff occlusion, after the application of calibrations. As a consequence, it was decided that the application of a different form of adjustment was necessary.

(a) Image collected at 640 nm without cuff.

(b) Image collected at 640 nm with cuff.

(c) Image collected at 650 nm without cuff.
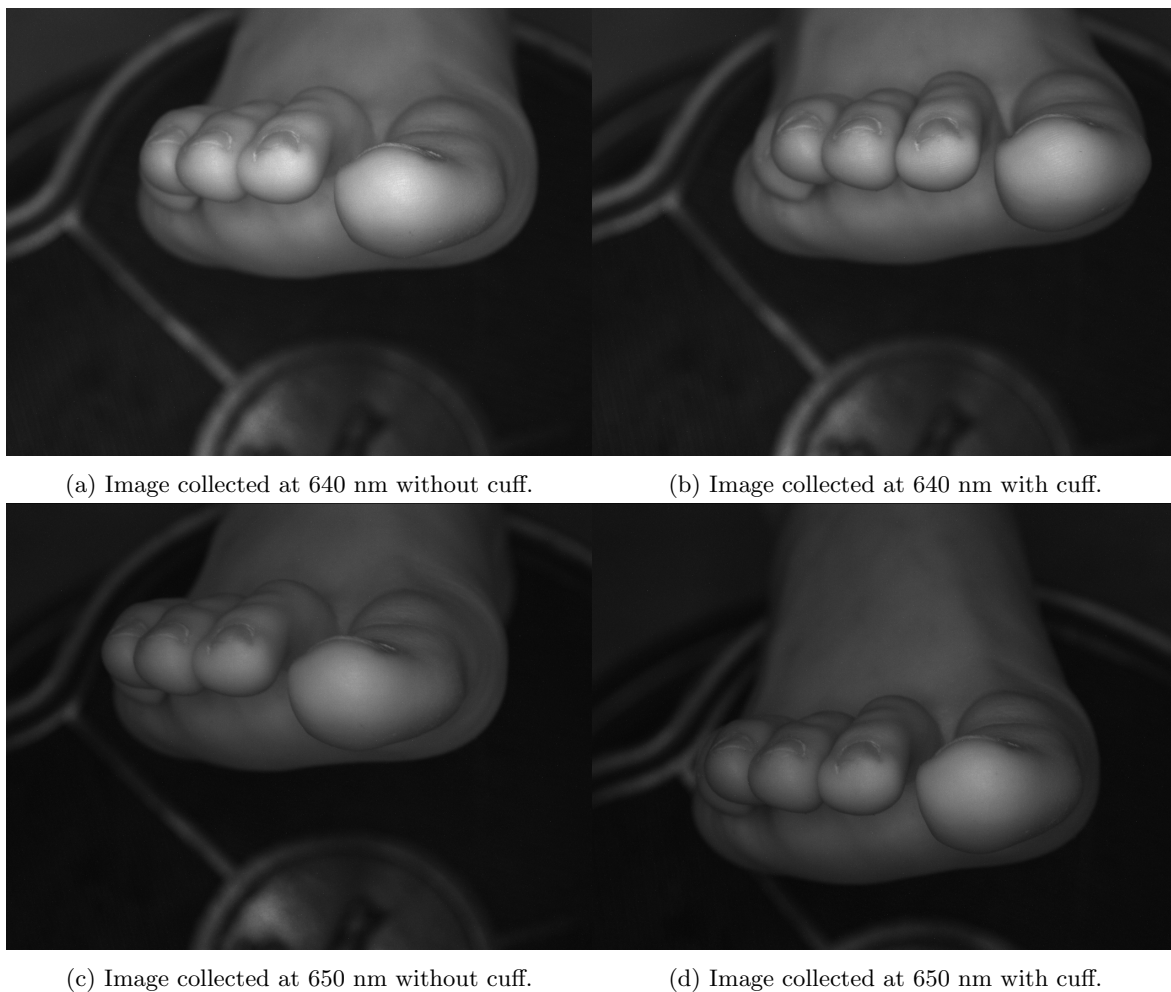
(d) Image collected at 650 nm with cuff.

Figure 3.5: Four consecutive toe images are shown, after flat-field and offset correction, exhibiting the current misalignment.

MATLAB has a variety of in-built functions regarding image processing, hence the decision was made to attempt the application of one of its inherent attributes.

At this point during the pre-processing method, the images were stored in an array within MATLAB, hence they had to be extracted from it, in the correct order, for the alignment function to perform accordingly. That being the case, the code commences with introducing and sorting the data available in a feasible manner.

(a) Image collected at 640 nm without cuff.

(b) Image collected at 640 nm with cuff.

(c) Image collected at 650 nm without cuff.

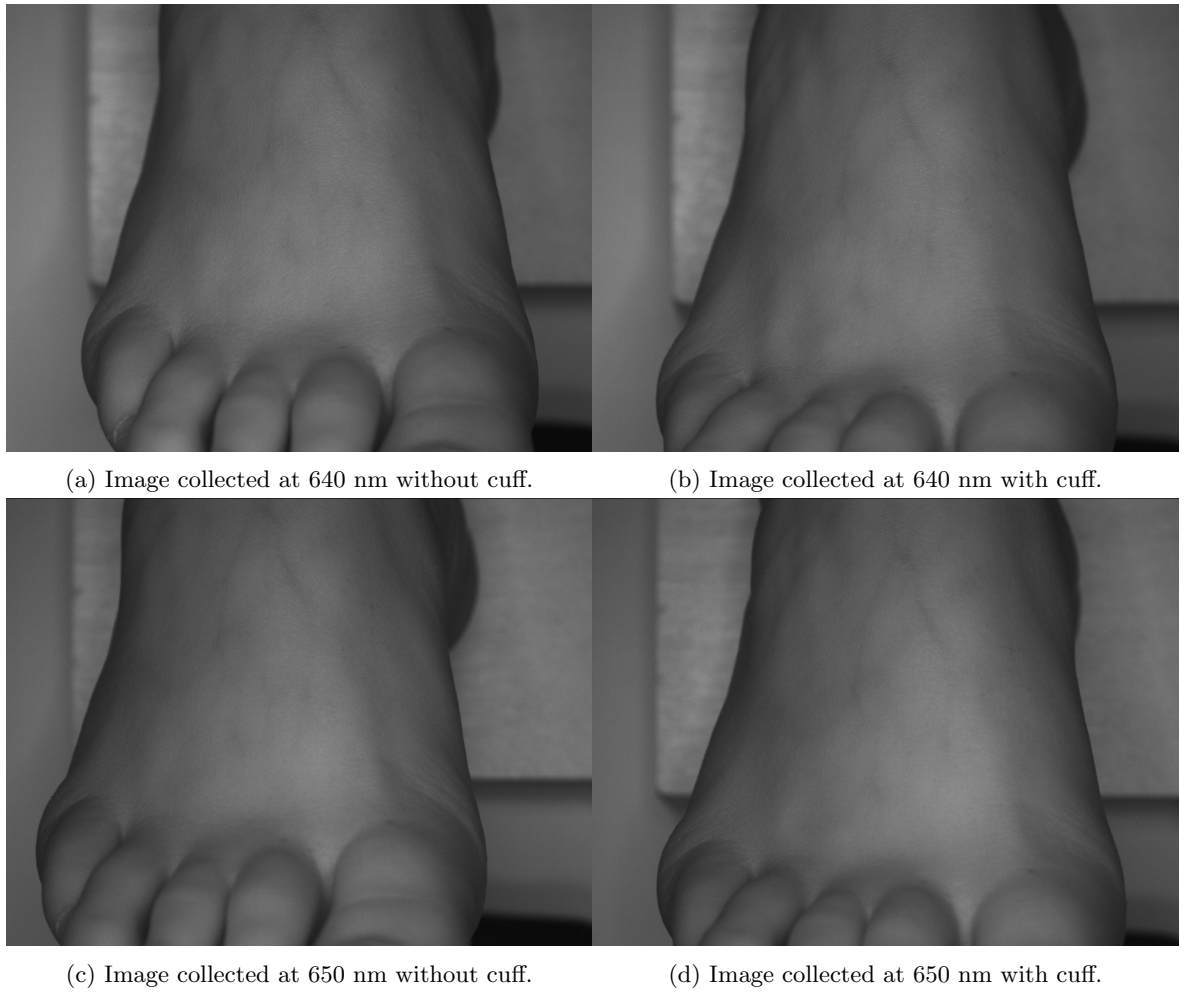(d) Image collected at 650 nm with cuff.

Figure 3.6: Four consecutive foot images are shown, after flat-field and offset correction, exhibiting the current misalignment.

Figure 3.7 illustrates the `for` loop used to extract the necessary images from the array and for further distribution. `Strfind` searches through all the files in the S1 array - where images were stored, and isolates all images whose first position in the name is occupied by the letter "f" (`posF = strfind(S1(k).name(1),'f');`", where '1' indicates the position in the file name), refering to images that depict the Pedis artery. In case the position does not have the aforementioned letter, it will be occupied by the letter "t", indicating the data with the images focused on the arteries ending in the toes.

The code then continues to go through the toe data, whilst instructing the software, using the nomenclature method mentioned above, to separate all the toe images with cuff occlusion from the ones without cuff occlusion. After distributing the two, the target moved on towards the remaining files and proceeded to perform the same technique in order to separate the pedis artery images with cuff occlusion from the ones without.

Concomitantly, for each set imported, the particular series of images were allocated in a cell array for higher accessibility. In Figure 3.7, the indexing expression `(:,1)==0,1` instructs

```matlab
for k = 1:numel(S1)
    posF = strfind(S1(k).name(1),'f');
    if isempty(posF) % Toe
        posST = strfind(S1(k).name(7),'s');
        if isempty(posST) % Toe without cuff
            ij = find(Epos(:,1)==0,1); %don't overwrite export values
            Epos(ij,1) = k;
        else % Toe with cuff
            ij = find(Epos(:,2)==0,1);
            Epos(ij,2) = k;
        end
    else % Foot
        posSF = strfind(S1(k).name(7),'s');
        if isempty(posSF) % Foot without cuff
            ij = find(Epos(:,3)==0,1); %don't overwrite export values
            Epos(ij,3) = k;
        else % Foot with cuff
            ij = find(Epos(:,4)==0,1);
            Epos(ij,4) = k;
        end
    end
end
```

Figure 3.7: Loop used for image extraction, depending on file nomenclature and further used for further alignment.

Table 3.1: Allocation of data into the array, where m is the number of the column.

m	1	2	3	4
	Toe without cuff	Toe with cuff	Foot without cuff	Foot with cuff

the import of the toe files without cuff into the first column of the cell array, whilst making sure no values could be overwritten while exported. As it can be seen subsequently, each series of files were eventually assigned into their own array column. Table 3.1 captures a better visualisation of how the data was allocated into the array.

Hereafter, the alignment functions `imregconfig` and `tformSimilarity` were applied on the existing files. The MATLAB intrinsic functions have the main attribute of performing an intensity-based registration of images with particular configurations.[75,76]

The exact function used to create the configurations needed to execute the image registration is illustrated in Figure 3.8.

The input data was set as 'multi-modal', which indicates that the images have different origins and different visual properties: contrast and illumination. The 'optimizer' and 'metric' param-

```
[optimizer, metric] = imregconfig('multimodal');
```

Figure 3.8: The function the optimises the registration configuration.

eters are then output as configuration methods during the follow-up registration. The 'metric' parameter creates an image similarity metric between the analysed images, while the 'optimizer' parameter develops a method for enhancing the similarity metric.[75,76] These configuration parameters are then employed during `tformSimilarity` function for image intensity registration.

Figure 3.9 depicts the function used in a more uncluttered manner for simplicity purposes. The image registration occurs at this stage, where A1 is the reference image and A2 is attributed to the following ones. As mentioned above, the process is simply an intensity based registration; the software gathers the first image from the set (toe or foot) and it uses the image as a coordinate for the rest of the data. It continues by trying to centre the rest of the images in respect to the previous form registered, hence theoretically leading to a more consistent position of the sample in all the output images. The method uses the obtained configuration parameters, while examining its similarity and eventually translating (explained in section 2.3.2) the image until it reaches a satisfactory geometrical transformation.

```
tformSimilarity = imregtform(A1,A2),'translation',optimizer,metric);
X = tformSimilarity.T(3,1); Y = tformSimilarity.T(3,2);
img = imtranslate(A2), [-X,-Y]);
```

Figure 3.9: Function used for image registration.

Unfortunately, the functionality of the system proved to have its drawbacks as well. After a few executions of the code it was noticed that the registration was applied to only one of the data sets. At

each iteration the function was either completely missing the foot artery data or yielding results in which the images were almost fully cropped. The reason for this being that the images containing the toes possess a more defined shape with various structural patterns, making it easier to detect, whereas the images displaying the foot area, such as the ones in Figure 3.6, can only offer an outline for registration. Therefore, using the default configurations, the software was not able to recognise the patterns.

To assess the reliability of the default configuration parameters and to determine the extent to which they influenced the results, a modified optimisation approach was attempted. Not only the shape of the sample in the image posed an issue, but also the fact that light intensity was more uniform due to the consistent shape. Increasing the brightness thus meant the image optimisation could be improved. Although increasing image brightness could normally lead to increased pixel intensity, which would have been extremely unfavorable considering the main approach of this method development is based on the intensity of the pixels, the method was only altering the data during the process of the registration using `imadjust`, after which the original brightness was recovered and the data was saved accordingly.

However, even with a modified optimisation the initial results for the foot data were unsuitable. The output images were returning with no valuable information present, as most of the images were translated and cropped outside of the foot's outline. As a result, the code in this section was subsequently altered to only further align the data that contains the toes and skip any images that are part of the foot without or with the cuff occlusion. This decision was taken due to time constraints as the code in question would need more attention for a higher efficiency, but also as its performance can be vastly influenced by the sample set-up and sample acquisition methods.

Figure 3.10 depicts examples of before and after images picked from the toe data. It can be seen how the imaged were picked and positioned in a more aligned manner as before. It needs to be mentioned that the automatic alignment does not interfere with the pixel intensity values.

Therefore, the images were taken forward for the next steps, whereas the foot images used were result of offset alignment. The foot data and toe data were not analysed to eventually be compared, therefore the extra overlap for toe did not affect the global results.
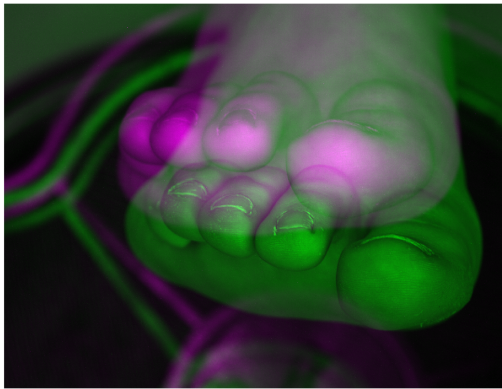
The overlay technique was based on the assumption that the foot was always pointed upwards facing the camera at the same angle, in an identical position. However, the positioning was impossible to control perfectly, hence the automated alignment was implemented.

(a) 540 nm without cuff image, before alignment.

(b) 540 nm without cuff image, after alignment.

(c) 640 nm with cuff image, before alignment.

(d) 640 nm with cuff image, after alignment.

Figure 3.10: Two before and after examples of how the toe images were aligned using MATLAB automation. The colours magenta and green indicate the areas of misplacement between the previous image used as reference. The after images show how the two colours are now closer to each other in placement.

Although the alignment has aided in the placement of the sample, they were still not in the exact same position, as can be seen in Figure 3.10. This is visible from the images in Figure 3.10b and 3.10d, where there is a disparity in the alignment. This has most likely resulted from the inconsistency in the positioning of the foot. There were 9 other filters used between the 540 nm and the 640 nm one, inevitably leading to misplacement between the image collections. However, having the samples more aligned with each other helped in the following section. Moreover, the placement may slightly affect the values reflected, under different light conditions. Nevertheless, many of the illumination consequences that may have occurred, have been mitigated by the flat-field adjustment.

After the code was generated, the images were saved externally but also in arrays. All the automatic alignments for all the toes images can be seen from Appendix .5.

The full script can be seen through the link in Appendix .4.

3.2 Image Processing

This section will introduce the procedures and methods used during the image processing phase, focusing on the coding components of the method development. This part of the code seeks to isolate areas of interest within the images collected and then continue with processing these regions for more information regarding oxygen saturation.

The aim for this particular processing is to eventually determine, through the exploration of these regions of interest, a preliminary set of visible wavelengths relevant in oxygen saturation detection.

3.2.1 Region of Interest

From the images captured during sample acquisition, only specific parts are of interest for further analysis. As explained in section 2.4 the areas that hold the most information are the pedis artery, located on the upper side of the foot, and the tip of toes, where the arteries end. Due to the nature of the acquisition type, the images contain a considerable amount of unnecessary background information, hence automatic features were employed to isolate the vital data from the sample. Being able to extract only the pixels that represent the artery placement from the image, was crucial for the following processing of the data, but the results can also help with the project development direction regarding any future work and improvement.

The code for this part was built as a function that feeds into the main script, following the pre-processing application. As displayed in Table 3.1, the data was divided according to the sample type and was stored in an array. Therefore, `for` loops and `if` statements were used to separate the four data groups and appoint towards the desired category. As the code was generated, it was firstly focused upon creating a region of interest (ROI) for the toe images. Due to the nature of the sample, these images contain four target areas rather than one global region of interest. Taking this into consideration and the shape of those areas, it was decided that the most appropriate MATLAB function to adopt was `drawellipse`, which constructs an elliptical ROI that has customizable properties.

`Drawellipse` was applied to all the images in question, starting with the first image of the first column in the array: toe image at 500 nm without arterial obstruction. As the code is generated, it firstly opens the image and the function allows the user to construct the ROI object. This was applied using the following line of code: `e = drawellipse('Label', ROInames(i,:))`, where each ROI was labeled with sequen-

tial numbering. The same function was then used to synchronize the features of the object, namely to ensure that the original coordinates and properties of each ROI in the first image are imported in all the following ones. This implies that after its creation, the same size ROI object will be employed for the rest of the data. However, due to the position of the sample in the image not being constant, the ability to manually move the ellipse was enabled without changing any of the original dimensions.

When using the function, the ellipse elements that were in focus were the: `'SemiAxes'`, which appoints the lengths of the semi axes; `'AspectRatio'` of the ellipse; `'Center'`, which delivers the coordinates of the centre of the ellipse; and `'RotationAngle'` for the clockwise angle of the ellipse.[77] The values for both the rotation angle and the centre of the ellipse, are dependent upon the position of the ROI object. When the ROI is relocated and rotated in order to encapsulate the correct area, their respective values change accordingly, nonetheless the size of the ROI remains the same and was therefore used for the rest of the data.

Due to inherent software functionality, creating the elliptical regions of interest proved to be accessible, therefore making the user interface easy to navigate. Once the process is generated and the first ROI created, the code runs through a `wait` function and allows the user to double click or press the `Shift` key to proceed to the next ROI, after saving the dimensions as reference.

Figure 3.11a shows the image at which the ROI selection occurred for this data group. As mentioned before, this image is the first in the array for the toe data and it represents the image captured at 500 nm from camera 1. The size of these ellipses were therefore taken as reference for the following images. In Figure 3.11, three additional images are presented from the same data group for comparison purposes. These images were randomly selected and it exhibits the visible disproportion between the position of the samples, but also the consistent size of the ROI object throughout the image cluster.

In order to be able to produce and save the information inside the ellipse, a binary mask was created. The ability to create a mask is an inherent MATLAB function from its Image Processing Toolbox. It creates a mask over the ROI created in the image by setting all the pixels inside the ROI mask to 1 and the outside pixels to 0. Although these pixels are changed in the mask, the original ROI and the pixels inside it remain the same and the information extracted from the ROI was not affected. As a result of this, characteristics important for the results of this section were extracted and saved in a array in MATLAB. The parameters extracted from each region of interest were the mean and range of the pixel intensity, the

(a) Drawing the initial ellipse.

(b) 500 nm with cuff.
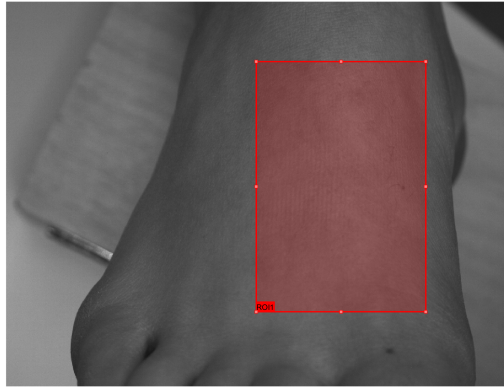
(c) 510 nm without cuff.

(d) 510 nm with cuff.

Figure 3.11: ROI selection for toe data, where the blue colour indicates the reference region for the rest of the images, whilst the red ellipses are the consecutive ROI selected.

minimum and maximum values and the standard deviation of the pixel intensity.

After delineating the regions of interest for these two image groups, the focus was directed towards the final two image clusters, which contain information regarding the artery at the top of the foot. A similar process was followed for this set of data as well. Due to the nature of the sample and the fact that the area of observation is substantially larger than the previous ones, the most appropriate ROI shape was a rectangle. The same principle followed, the object created has the same size all throughout the image set, however it has been moved with the position of the foot, so as to follow the same area for each image. The function used to construct the region of interest was `drawrectangle`, which is another in-built MATLAB function for image processing, hence it has the same functionality regarding user interface as `drawellipse` did.

As explained in the previous section, this image group did not undergo any further alignment aside from offset calibration. Therefore, the discrepancy between the position of the sample in each image is more noticeable. Figure 3.12 depicts four images with the rectangular ROI drawn, where a) is the image at 500 nm and was the first to be processed, thus the ROI
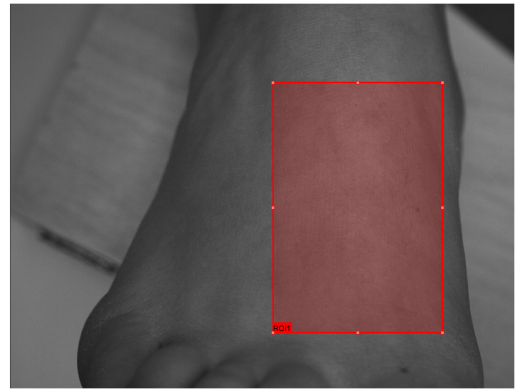
(a) Drawing the initial rectangle.
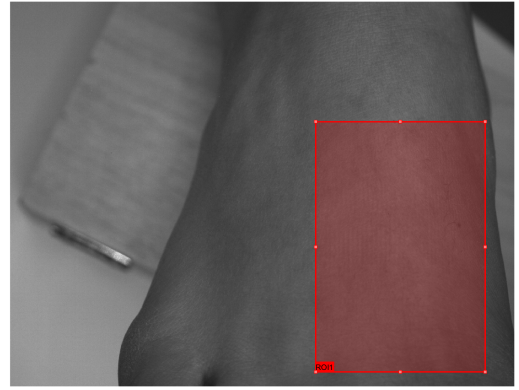
(b) 500 nm with cuff.
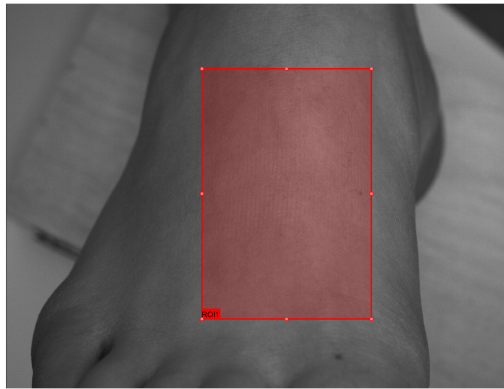
(c) 510 nm without cuff.

(d) 510 nm with cuff.

Figure 3.12: ROI selection for foot data, where figure 3.12a indicates the reference region for the rest of the images.

from this sample was used as reference. Although the object created was moved considerably between images, the region-to-region comparison is still highly reliable due to the manual shift of the object. Moreover, as an initial method development, the main purpose was to be able to yield a substantial amount of information out of these chosen areas to confirm the theoretical performance of the system, and then focus on optimising the approach.

The rectangular ROI function was more accessible regarding data extraction, as it was not necessary to create a binary mask prior to it. In order to isolate the region, a function that crops the image was used. While the ROI was created, MATLAB registered the position of the object for each image, thus using its coordinates as a variable, the function `imcrop` was applied and the ROI object was isolated from the image. Afterwards, the same parameters extracted from the ellipse object were also obtained for the cropped rectangular ROI.

Due to the size of this ROI, it was decided that to increase the accuracy of the resulting information from the regions created, it would be beneficial to divide the area into six smaller segments with two columns and three rows. The exact pattern in which the main ROI was divided and saved as, is displayed in Figure 3.13. The reason being that for such a large ROI,

the data might yield false results for the pixel intensity calculations.

In order to execute this, the code was written using the coordinates, the length and width of the rectangle and the numbers of rows and columns wanted. No visible outcome resulted through this function, specifically there was no image displaying only the segmentation created as this was executed automatically within the software. The localisation of the axes of each segment in the rectangle was performed, a temporary ROI was created with the coordinates of each segment and data parameters were extracted accordingly. The same parameters as for the main rectangle were obtained for the six segments as well. Then the values were saved in the MATLAB array, awaiting further analysis.

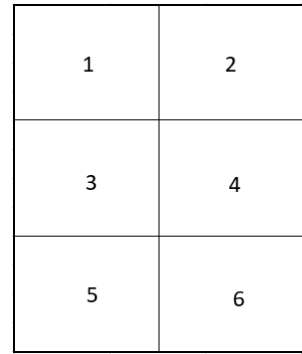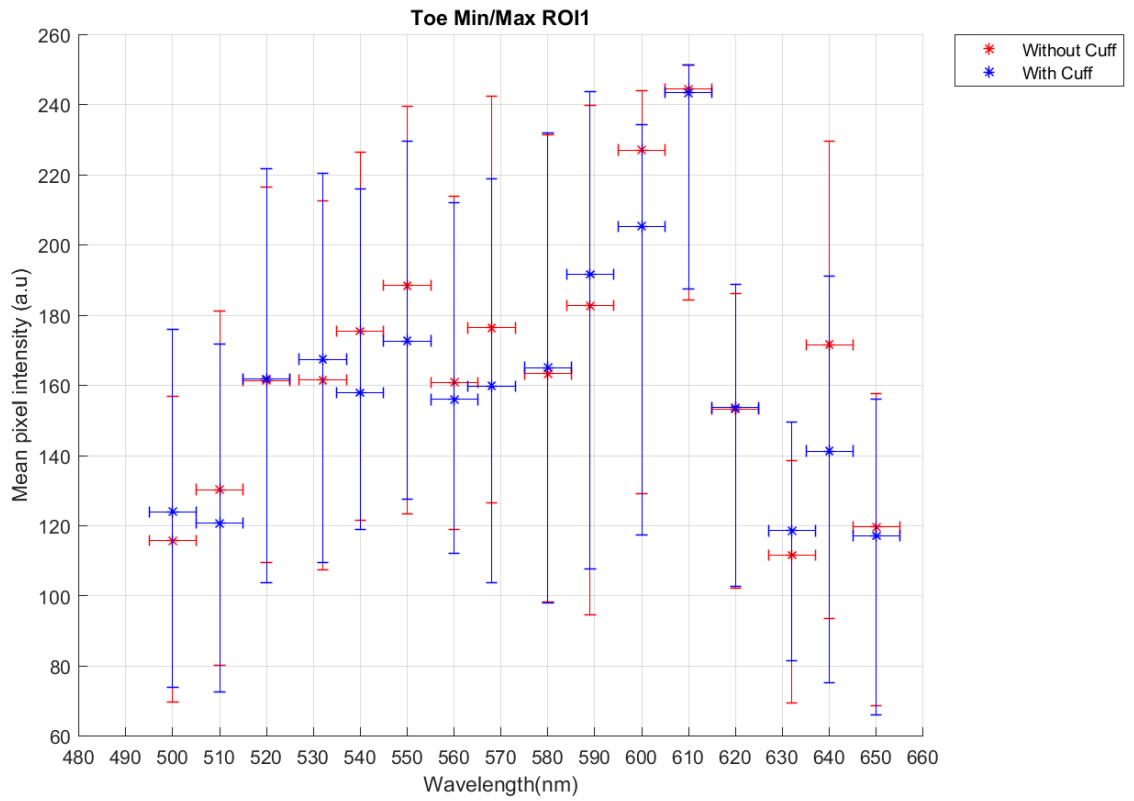| 1	2
3	4
5	6

Figure 3.13: Diagram displaying the segmentation pattern of the main foot ROI. Dividing the ROI aids in the developments of a tissue oximetry sensor for the 6 segments. This is important as it provides a higher sensitivity and specificity for the output data, particularly when the ROI is large.

Once all the regions of interest were produced and all the parameters needed were extracted and saved accordingly, it was first necessary to create a visual representation of the data to identify the essential filters. Using MATLAB, scatter plots of the mean pixel intensity were created for each ellipse, rectangle and segmented rectangle for both with and without cuff images, with the y-axis of pixel intensity and the x-axis of wavelength. Error bars were included in the graphs produced, displaying the range with the minimum and maximum values and the standard deviation on the y axis and the Full Width at Half Maximum on the x axis. FWHM was set by the manufacturer as being 10 nm, hence 5 nm on each side of the mean.
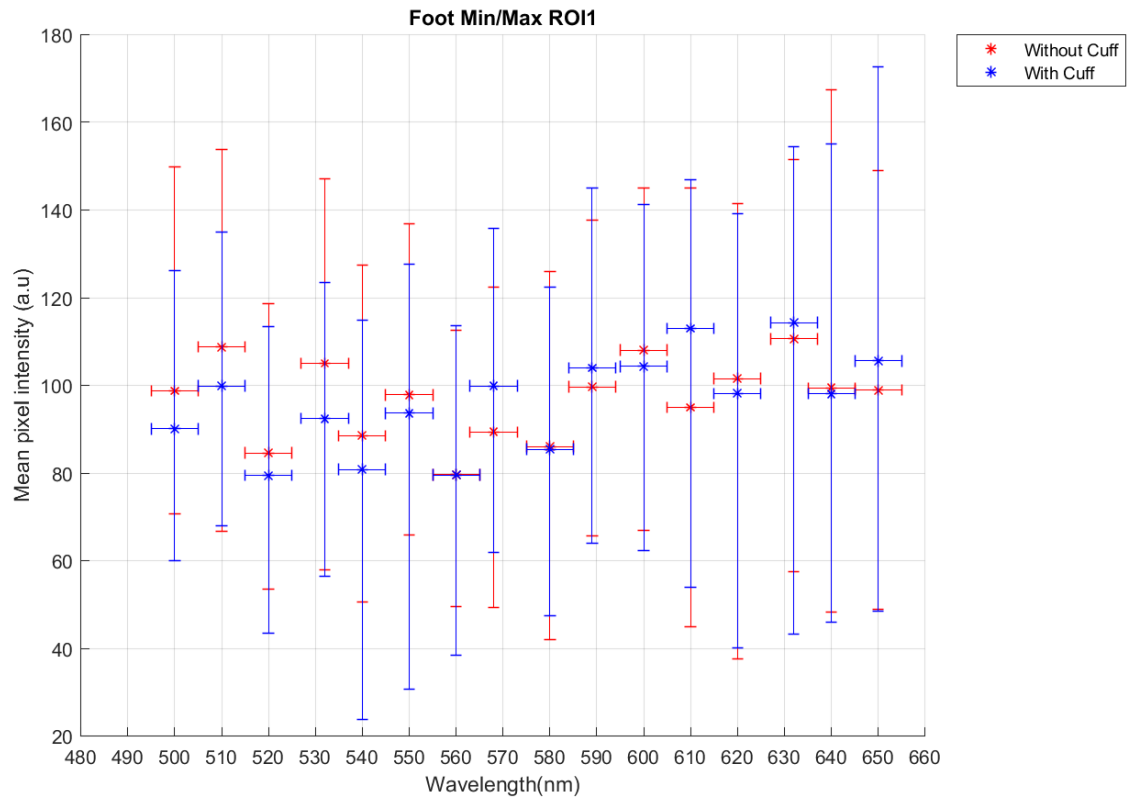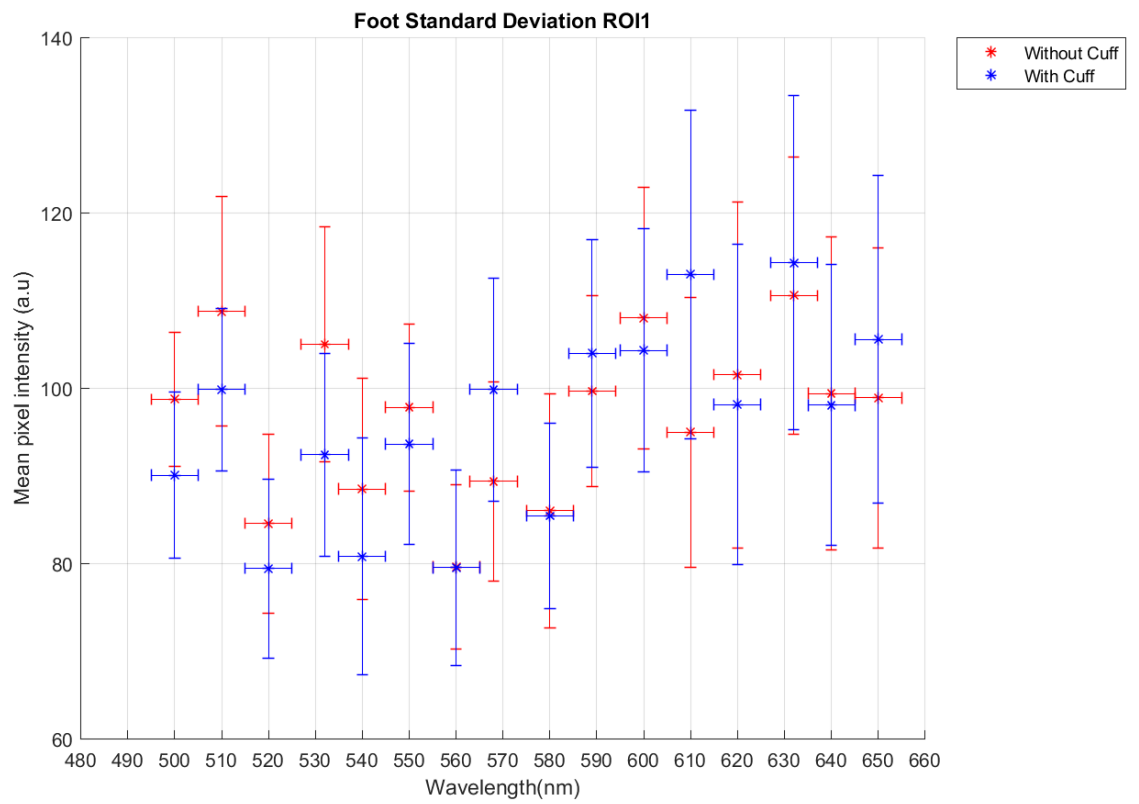
(a) Toe ROI 1 range for each filter.
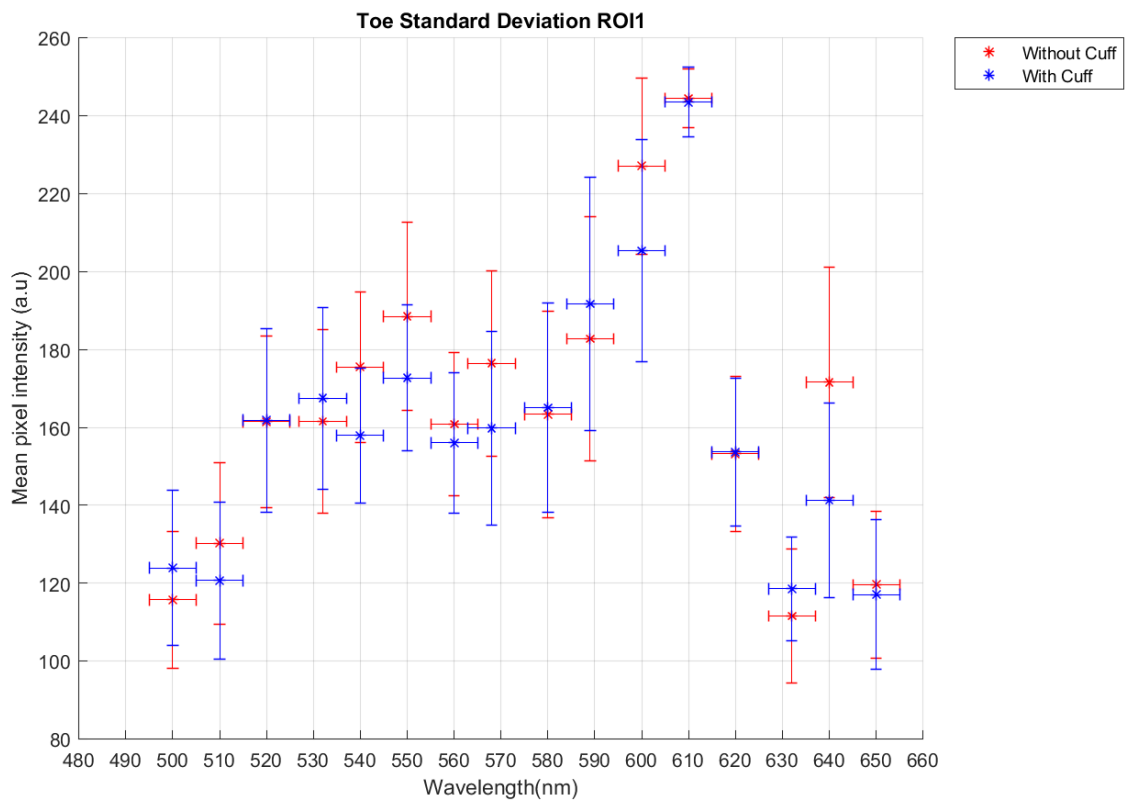
(b) Toe ROI 1 standard deviation for each filter.

Figure 3.14: The resulted graphs for ROI1 of the toe samples. Mean pixel intensity of each image for the specific ROI is shown for all filters. Both standard deviation and range are displayed, as error bars, together with the 10 nm FWHM.

(a) Foot main ROI range for each filter.

(b) Foot main ROI standard deviation for each filter.

Figure 3.15: The resulted graphs for the ROI of the foot samples. Mean pixel intensity of each image for the specific ROI is shown for all filters. Both standard deviation and range are displayed, as error bars, together with the 10 nm FWHM.

As it can be seen from Figures 3.14 and 3.15, the range for the regions of interest seem to be higher the the overall standard deviation. This could mean that there are outliers and extreme values, however the spread of data around the mean value was not as extreme.

The pixel intensity values from the foot area are lower than the ones from the toe area, indicating that the foot ROI might have not experienced as much reflectance as the toes do.

The graphs can be hard to decipher simply by visualising them, which is why a significance test was developed in order to choose the best fit filters.

All graphs for each ROI are available for visualisation through Appendix .5. The entire code for this section can be seen through the link in Appendix .4.

3.2.2 Significance Test

The final section of this chapter, will focus on the method used to determine the preliminary four most appropriate wavelengths for tissue oxygenation.

As outlined above, each wavelength had two images acquired, with and without cuff. Plotting the mean pixel intensity value for each ROI against the respective filter, allowed for a visualisation of the difference in intensity between the cuffed, deoxygenated regions, and without cuff, oxygenated regions, for each wavelength.

Achieving the purpose of this operation, required to examine the region of interest results and try to highlight the wavelengths for which there is a distinct difference between O_2Hb and HHb, as a result of the arterial obstruction. Additionally, a wavelength for which the difference between the two points was minimum across the whole range of filters, was also determined. This is an isobestic point in the data obtained, where little to no change occurs in the reflectance of O_2Hb and HHb for that wavelength. The incentive for choosing an isobestic wavelength consists in having a filter that acts as the calibration point. Along the process of adjusting and improving the techniques used, certain possible issues can appear, such as non-uniform illumination pattern or just illumination changes, that can affect the pixel intensity culminating in false results. Therefore, always setting one of the four filters at the isobestic wavelength, can assure the same response from the camera regardless of the tissue oxygenation. The data from the rest of the filters would therefore be relative to the isobestic one.

The theory of choosing a minimum and maximum difference between oxygenated and deoxygenated tissue, has a strong literature back-up and it has been known to function as expected with both, absorption and reflection of light.[23,31,47,48]

At this particular point, the main question was not only focused on determining the optimal filters from the ROI graphs, but also on the steps that needed to be taken to reach the final aim of determining the four filters. Having to chose only four filters out of the 16 for further testing, imposes some limitations, particularly when some of the values seem to be closer together. Evidently, when visually assessing the pixel intensity graphs (Figures 3.14, 3.15 and Appendix .5), there are few assumptions which can be made regarding the range of the filters across each wavelength. Moreover, the pixel intensities have different levels depending on the sample in question. For the toes, the intensity range between oxygenated (without cuff) and deoxygenated (with cuff) resides between 120 - 240 a.u., whilst the intensity range for the foot resides between 80 - 120 a.u.. The foot ROI has an overall lower pixel intensity, which can be explained by the larger size of the ROI and may also be due to variations in lighting. A common point to observe is that the differences between the oxygenated points and the deoxygenated points do not exhibit extensive and considerable variations.

Nonetheless, there is a large quantity of data available, with each point representing the mean intensity and the error bars clearly displaying outliers. In the most simplest manner, the method could have only focused on the mean values and determine the required wavelengths in this fashion, nonetheless this would have been innacurate as the spread of data is unknown. Thus, the most appropriate approach was to automate the whole process in MATLAB by performing a statistical test, in order to be as consistent as possible and to validate the final results to a certain degree.

Considering the fact that each of the sample has known standard deviations and means, it was decided that the most suitable test to study the two groups of data was the z-test. A z-test compares the means of two sets of data, similarly to a t-test, however it is based on known standard deviations.

The written code for this section, given the name of Significance Test, was firstly generated by importing the parameters of the regions of interest, that were created during the previous section. This was again based on the array from Table 3.1, while also referring to the number of regions present.

After making sure that the script recognised the data developed up to that point, the code starts focusing on the each group of data, while indexing the means and standard deviations required to perform the z-test.

The code used for importing the data necessary to process a z -test can be seen in Figure 3.16. The part illustrated belongs to the first few lines of code and form the first array. As

```
  if m == 1
    Toes{i}(n,1) = str2num(S1(Epos(n,m)).name(2:4)); %Wavelength
    Toes{i}(n,2) = S1(Epos(n,m)).mean(i); %Mean without cuff
    Toes{i}(n,3) = S1(Epos(n,m)).std(i); %STD without cuff
  elseif m == 2
    %Find wavelength values to build array
    Index = find(Toes{1}(:,1) == str2num(S1(Epos(n,m)).name(2:4)));%Find exact position of wavelength
    Toes{i}(Index,4) = S1(Epos(n,m)).mean(i); %Mean with cuff
    Toes{i}(Index,5) = S1(Epos(n,m)).std(i); %STD with cuff
    Toes{i}(Index,6) = ztest2(Toes{i}(Index,2),Toes{i}(Index,4),0,0,(Toes{i}(Index,3)^2),(Toes{i}
(Index,5)^2));
```

Figure 3.16: Code used to build an array with the information needed for performing a z-test. It shows the extraction of mean pixel intensity values and the standard deviation of each ROI from each image.

it can be seen, the code firstly generates the information for `m==1`, namely for the toe images without cuff occlusion. The parameters were extracted and stored in a column position within the array. The first column indexed the 16 filters, the second column displays the mean pixel intensity value of the regions of interest without arterial obstruction, while the third column stored the standard deviation of the same data.

The code then continued by moving to the next group of data, `m==2`, which was the toe images with cuff occlusion. Next, it identified the wavelengths stored in position one, in order to match the wavelength with its data. The following three lines proceeded to arrange the mean pixel intensity value of the regions of interest with arterial obstruction and the standard deviation of the data, in column positions four and five, respectively. The sixth column represents the z-score resulted after the application of the z-test on the means and standard deviation of the two samples for each wavelength. As mentioned earlier, this was generated for each region of interest. The produced array was then exported as an Excel file with all the data available for each region. However, before moving the data externally, the rows within were sorted by increasing numerical value of the z-score. Hence the top rows displayed the smallest difference between the two data points, whilst the bottom rows show the highest difference.

The same code as in Figure 3.16, was adjusted for the main region of interest and its six segmented areas from the top of the foot. They were also exported externally. Appendix .6 contains all the arrays exported for each region of interest, starting with the toe data for ROI 1 and continuing with each region for each set of data.

The z-test formula is displayed in Equation 3.2, where x_1 and x_2 represent the means of the two samples, μ_1 and μ_2 are the means of sample population, σ_1 and σ_2 are the standard deviations, and n_1 and n_2 is the sample size.[78,79]

$$z = \frac{((\bar{x}_1 - \bar{x}_2) - (\mu_1 - \mu_2))}{\sqrt{\frac{\sigma_1^2}{n_1} + \frac{\sigma_2^2}{n_2}}} \tag{3.2}$$

The z-score is an indication of how close the oxygenated value is to the deoxygenated value for each wavelength at each region of interest. The smaller the z-value, the closer the two points are together, hence the filter with the lowest z-value was considered the isobestic filter. However, the filter that was needed, was the one that was most consistent across all regions for each sample set, for both the isobestic and larger difference points. The reason for this is that the camera used has a limited number of 4 filters that can be performed at a time, hence the chosen wavelengths had to be the most accurate.

	ROI 1	ROI 2	ROI 3	ROI 4
−	520	520	520	640
	620	580	560	610
	580	650	500	520
	610	532	589	500
	650	500	532	532
	532	560	650	589
	560	620	580	580
	589	589	610	650
	500	632	550	600
	632	510	568	560
	510	550	510	510
	568	540	620	550
	550	568	600	620
	600	600	640	632
	540	640	540	568
+	640	610	632	540

Figure 3.17: Toe filter wavelengths (nm) displayed in order of z-score for each ROI. Starting from the top with the lowest z-score and moving down to the bottom of the table, with the highest scores. The rows in light red indicate the minimum and maximum four z-scores for each ROI. They are also the areas in which the scoring method for finding the most common wavelength, has been applied.

During the code execution as the loop progresses, it completes the array and after each export iteration, a rank system was included in order to be able chose and validate the best fit filter for both samples, toe and top of foot.

An inner function, within the current function, was built to establish the most common filters and to help classify them. The manner in which this was accomplished, was by giving the code a command in which it only focuses on the top four and bottom four filters from the z-value arrays created previously (Appendix .6).

The code scans through the compiled data structure and selects the most frequently occurring filters, using the function `mode`, across all regions of interest for each type of sample. In order for a wavelength to be suitable and for the process to continue, the number of occurrences in the data had to be higher than 1. The function created allowed for the code to start recording the wavelengths that appeared more than once. The first filter found was then stored and the scan continued until the number of occurrences was registered. Once the total number of iterations for the filter was found, the function was cleared and the scan continued for the rest of the wavelengths.

Altogether, this segment of the function delivers the number of repeats for each wavelength that occurs more than once, across the top four z-values for all regions of interest, from both foot and toe sample sets. The reason for operating this in an automatic fashion, was due to

the ranking system that followed after. In order to be able to score the filters and classify them correctly, it was necessary to find the ones that occur to most, therefore not having to apply to process on all the filters available.

Once this has been acquired, the function scans through the most frequent wavelengths chosen, for both smallest and largest difference, and it assigns a score to each filter, depending on their position in the array column. The score was assigned based on minimum to maximum z-value, however if the respective filter was not present in one of the columns, it received a zero score. The closer the score is to the desired point, minimum or maximum, the better fit the filter represents.

Figure 3.17 shows a table which contains all 16 filters in increasing value, for all four regions of interest extracted from the toe images. The areas highlighted in light red, represent the part of the columns in which the generated code scanned for the most frequently occurring filters and then assigned each a score. For example, the filters with the wavelengths of 540 nm, 600 nm and 640 nm repeat 3 times across the regions for maximum z-value. When applying the classification system the process develops as it follows: filter 540 nm appears

	Main ROI	ROI 1	ROI 2	ROI 3	ROI 4	ROI 5	ROI 6
−	560	620	620	510	640	589	632
	580	520	632	550	632	560	640
	640	640	640	520	620	550	620
	620	580	600	600	589	632	560
	632	500	568	640	560	650	580
	600	550	589	589	580	510	589
	589	532	580	560	568	520	568
	650	510	650	650	600	600	650
	550	650	560	580	650	640	550
	520	540	540	532	540	532	540
	540	600	520	500	550	580	610
	510	560	610	632	520	568	600
	568	589	550	620	610	500	520
	500	632	500	540	500	620	510
	532	568	532	568	532	540	500
+	610	610	510	610	510	610	532

Figure 3.18: Foot filter wavelengths (nm) displayed in order of z-score for the main ROI and its segmentation. Starting from the top with the lowest z-score and moving down to the bottom of the table, with the highest scores. The rows in light red indicate the minimum and maximum four z-scores for each ROI. They are also the areas in which the scoring method for finding the most common wavelength, has been applied.

in the first column on position 3 from minimum to maximum, in the second column it is not present, in the third column it appears in position 3 again and in the fourth column it resides in position 4. Each of these positions represent the score number associated with the filter. When added together, the filter receives a score of 3+0+3+4 = 10. The same system leads to filter 600 nm and 640 nm to score a value of 5 and 9, respectively. Therefore, the filter with the highest score, 540 nm, was chosen as best choice for the largest difference filter, across the regions of interest from the toe data. Same classification took place for lower z-value filters, only fitted for the isobestic point.

Eventually, after the scoring system for each data set took place, the code generated and exported a data file with all the final information within. Figure 3.18, similarly to Figure

Table 3.2: Filters determined by the automatic Significance Test for all areas of interest.

	Largest Difference Filter	Isobestic Filter
Toes	540 nm	520 nm
Foot	610 nm	560 nm
Foot Segmentation	610 nm	620 nm

3.17, presents all the 16 filters for the global region of interest, from the top of the foot, and its six segments.

The results from scanning and classifying all the filters, can be seen in Table 3.2, where the determined filters for toes, large foot ROI and foot segmentation where exported by the 'Significance Test' script. Therefore the filters that, according to the current data, seem to demonstrate best suitability for the toe samples are: 520 nm for isobestic wavelength and 540 nm for the wavelength displaying the most difference between oxygenated and deoxygenated data. Whereas for the main foot region, the filters are 560 nm for its isobestic point and 610 nm for the wavelength that shows the largest variation. Values for the foot segmentation were also produced: 620 nm and 610 nm for the isobestic and variation points, respectively.

When looking at the results of the top of the foot data (see Figure 3.18), seeing as wavelength 610 nm appears at the end of the column for three of the segmentations, but also for the global region of interest, it becomes understandable why the system classified 610 nm as being the best fit in this point for both. It is also encouraging because it validates the test used, as it is expected to have filters that match, particularly for the same samples.

However, when examining the foot segmentation filter columns more in depth, it could be argued that 610 nm only covers half of the region. Although the major region of interest also has 610 nm as the maximum difference, when looking at the divisions made within the foot area and how they were split (Figure 3.13), it can be seen that only the left side of the region sports a predominant 610 nm wavelength, whilst the right side has different wavelengths in the first positions and the 610 nm filter climbs closer towards the centre of the column.

This particularly shows a lot of continuity for one side of the foot area, however the fact that the main region of interest still has 610 nm in the highest position, might indicate that the right segments don't substantially affect the outcomes, at least for this intersection point.

When directing the attention towards the isobestic fiters at the top of the columns, the left side of the region, formed by segments 1, 3 and 5 (Figure 3.13), does not have the first position as consistent with the filters it displays. Furthermore, when manually performing

the ranking system only for the left side of the whole region, the only filters that repeat more than once are 520 nm and 550 nm. They occur twice and both have a ranking score of 5, therefore they do not particularly indicate a best fit filter for them. This may come down to a flaw within the ranking system, which would be that there is not enough fidelity involved when the process is applied.

The automatic rank system determined the filter for the segmentation to be 620 nm, which is understandable as it occurs in four out of the six segments. Out of the four occurrences, three of them belong to the right side of the main area of interest. Thus, as opposed to the other side of the column that was mentioned previously, this shows more variety in the results.

The isobestic wavelength chosen for the global region of interest was 560 nm, which is distinct to its segmentation, as in most of them the 560 nm filter is closer to the centre of the column.

When observing all of the first wavelengths in each column (Figure 3.18), it can be seen that other than between the first two segments (named here as ROI1 and ROI2), there is a constant oscillation occurring. It is very possible that certain filters may have been omitted due to the high fluctuations between the values in each segment.

Fluctuations were however expected, mainly due to the differences between each area of the foot. The global region of interest is large enough to present dissimilarities from one side to another. In Figure 3.12 from the previous section of this chapter, it can be seen the size of these regions and since they were split in six equal parts, each part can elicit distinct results. This is due to the way the sample foot is positioned in the light and the spectral reflection that may take place on different sides of the foot.

Although it is early in the method development for the segmentation of the regions of interest, the main reason for segmenting a large ROI is to eventually be able to decide on certain parts that can provide best results and continue extracting more data from them. For example, the second segment, which is the one in the top right side, will always present a certain degree of shading due to the natural position of the foot and the camera arrangement, hence expectations of extremely accurate results from this part would be low.

On the other hand, when observing the filters belonging to the toe samples (Figure 3.17 and Table 3.2) the situation, interestingly, becomes reversed. There was no doubt that 520 nm was the most appropriate wavelength regarding the isobestic filter for this data. This is also endorsed by the mean pixel intensity scatter plots created (Appendix .5) for the toe

regions of interest, that are also the foundation of the current results. Compared to the top of the foot area, this regions are much smaller, therefore it can provide a more stable result for now, due to lack of wide data range. However, the sample was subjected to the same collection technique and it could still be affected by external factors, such as illumination.

Although the 520 nm filter is located in the first position for the first three regions of interest, in the fourth column the filter is found in the third position. This still provides enough valid information to prove the suitability of the filter as the isobestic wavelength. Nonetheless, having ROI4 yield different results was anticipated, mainly due to the low quality of the captured area. The nature of the sample made this particular location to be slightly out of focus in certain images and it can also presents shading in particular areas, contributing to its poor results.

When examining the isobestic data for both foot and toes, it is clear that the toes provide a more stable and consistent information, whereas the foot regions produced a wide variety within the results. It was also necessary to take into consideration the fact that the left side of the foot, might be more uniform in the delivery of its results. Regions 1, 3 and 5 of the left side of the foot display the 520 nm wavelength relatively close to the isobestic points, in the columns. As mentioned before, this is most likely due to the shading that occurs on the other side of the ROI, which falls in line with the results from the toes data. When looking at the Significance Test results from Appendix .6, it becomes noticeable how similar the oxygenated and deoxygenated points are, particularly for the standard deviation. Combining this with how conclusive the toe data is, resulted in the decision to only use 520 nm as an isobestic filter for both sets of data. This decision was also taken with the advice of a NHS podiatrist, which confirmed that due to the digits being the furthest away from the heart, they have more vascular sensitivity and can therefore provide more valid information. Having the same isobestic filter for both samples also signified that, due to the limitation in the number of filters that can be chosen, there would be extra possibility to test other filters that could prove distinct contrast between oxygenated and deoxygenated data.

Interestingly, when following the data from toe ROI, 520 nm and 540 nm were chosen as opposite poles by the system, however the are extremely close wavelengths. The reasoning behind this might be related to the fourth ROI again.

The wavelength for the larger variation points was selected to be 540 nm. Knowing that ROI4 has the potential of yielding false results, the ranking system was manually applied again for the first three regions only. When rating the most frequently occurring filters, it

Table 3.3: Final filters that were chosen for further testing for all areas of interest.

	Largest Difference Filter	Isobestic Filter
Toes	540 nm/640 nm	520 nm
Foot	610 nm	520 nm
Foot Segmentation	610 nm	520 nm

was shown that without taking the last ROI into consideration, the filter which would have scored the highest value would have been 640 nm, with a score of 9, whilst 540 nm ended with a score of 6. An interesting point to observe, is the contradictory reversion of the 640 nm filter in ROI4, where it is positioned in the first place, namely isobestic. This also proves that certain data collected may have not been in best conditions.

The position of 540 nm across all regions is relatively high, hence making it a favourable filter. However, due to the condition of ROI4 recorded, the 640 nm filter should not be disregarded. When adding all of these hypothesis together, it was decided to try both filters, 540 nm and 640 nm. They both have highest z-values and are in the top of the list. The premise for these decisions came from the position that, depending on the results of the subsequent data, each filter position might need to be optimised. The results of the toes data was promising to begin with due extra consistency, therefore both filters should be tested regardless.

All in all, there are several different decisions that could be made, mainly due to the variety in the results, however drawing all inferences from data from one individual was not conclusive enough. These results were based on one data point, thus extra data and testing is required in order to fully validate the filters. Moreover, acquisition of data sets under different conditions, with different skin pigmentation would also be useful.

Hence, the filters that were chosen and were used in the following tests can be seen in Table 3.3. These wavelengths will, therefore be used for the application of Beer-Lambert Law for tissue oxygenation and in any ensuing tests for more insight regarding further method optimisation.

This code was created in order to determine the filters that should be tested subsequently. Therefore, this script was not included in the main call function. It is not a script that will be part of the clinical process once the test start. Clinical application of this system will already have fixed filters that can deliver the functionality needed, without having to change them. The reason for having fixed wavelengths relates to the fact that the camera can only

hold 4 filters and to the need for a simplified system.

With this in mind, this function remains separated from the main script and can only be generated individually, when necessary.

When the final results of this section are observed in perspective to the literature wavelengths from Table 1.1, it can be seen that although the wavelengths chosen fit into almost all the ranges tested in the literature, the specific isobestic wavelength and the wavelengths sensitive to changes, exhibit some variations. Comparing specific wavelengths to a literature, which uses mostly ranges of wavebands due to higher specificity instruments, creates some limitations in determining highly accurate wavelengths for the points needed.

The isobestic wavelength determined here of 520 nm, although it is close to the ones given by Rubins *et al.*[51], it is still outside the range by 20 nm. For the wavelength susceptible to change, Akbari *et al.*[45] and Rubins *et al.*[51] define a close range to the 640 nm established here, whilst Bashkatov *et al.*[13] determines it to be 540 nm, which matches one of the filters chosen previously for the toe data.

There clearly are limitations and a lack of high specificity with the process of determining the wavelengths at the moment. However the only valid method of improving the process would be through repeated tests and further clinical trials, which are not available during this stage of the research.

The entire code for this section can be seen through the link in Appendix .4.

Chapter 4

Oximetry Map Development

Tissue oxygenation has been heavily researched in the past, particularly the application of a modified Beer-Lambert Law (BLL) towards oxygen saturation.[23,31] As mentioned in Section 1.3.2, the oxygen saturation is calculated (Equation 1.1) based on the ratio between O_2Hb and HHb, from which different variations of the formula can be created depending on the aim of the research.

There have been studies in which the extinction coefficients for both O_2Hb and HHb are unknown, hence certain algorithms have to be put in place as well.[47]

Furthermore, the method also carries some limitations, which can be accounted for and adjusted. The challenges mainly concern the other chromophores, which may have an effect on the optical reflectance of the blood vessels.[31] There are less significant chromophores, such as carotene, bilirubin or lipids, whose influence is not normally considered in tissue oximetry methods.[13,28,31]

However, there is one important pigment chromophore for the visible wavelength range, which has been investigated and considered in oximetry, melanin.[23,31] Melanin is one of the main absorber of light in the epidermal tissue[51] and if distributed abundantly it can cause substantial alterations to the MSI oximetry.[28,31] Therefore, melanin has been accounted for in studies, by taking into consideration its extinction coefficients and implementing them within the formula.[31,51]

Recognising and implementing the melanin factors is extremely important, particularly when studies involve clinical trials. However, for this stage of the discussed research, the foot sample used belongs to only one individual. Hence, the melanin coefficients are constant throughout the study. The implementation within the formula has been performed by multiplying with the melanin coefficients factor[51], therefore in this case the factor would be 1. For

the next sections the melanin will not be considered due to the consistency motive, explained above.

This chapter investigates two approaches of Beer-Lambert Law for the development of oximetry maps, to identify the resulting relation between the visible wavelengths used and the tissue oxygenation. Although two methods were examined, only one was carried forward due to its suitability to a clinical environment.

Both methods were applied through MATLAB and the scripts created for the application are explained in the following sections. The same code was subsequently executed for the next sets of images acquired.

4.1 Dual-Wavelength Oximetry Map

4.1.1 Beer-Lambert Law

The Beer-Lambert Law applied for this method, is based on two wavelengths: isobestic wavelength and the wavelength which exhibits the highest sensitivity the change between O_2Hb and HHb. It operates particularly well when the extinction coefficients are known, due to the fact that it functions by looking at the proportion between oxygenated haemoglobin (O_2Hb) and deoxygenated haemoglobin (HHb), based on the location of the isobestic point. [47,48]

The equation [47] used to measure the oxygen saturation of the tissue can be seen below:

$$SO_2 = \frac{\varepsilon_{HHb}^{\lambda_1}}{\left(\varepsilon_{O_2Hb}^{\lambda_2} - \varepsilon_{HHb}^{\lambda_2}\right)} \times \frac{\Delta A^{\lambda_2}}{\Delta A^{\lambda_1}} - \frac{\varepsilon_{HHb}^{\lambda_2}}{\left(\varepsilon_{O_2Hb}^{\lambda_2} - \varepsilon_{HHb}^{\lambda_2}\right)} \tag{4.1}$$

Where λ_1 represents the isobestic wavelength and λ_2 represents the wavelength with the biggest variation. $\varepsilon_{HHb}^{\lambda}$ and $\varepsilon_{O_2Hb}^{\lambda}$ serve as the extinction coefficients of HHb and O_2Hb at each wavelength, whilst ΔA^{λ} is the total reflectance for the specific wavelength λ.

The application of the formula depends on the data that is extracted. In this case, applying the formula using only the mean value for each ROI, would only result in comparing the regions of interest with each other, leading to a more generalised approach. Blood vessels would be more difficult to visualise in a large region, hence it was decided to apply the formula on each pixel of the regions, producing a pixel by pixel comparison and oxygen saturation (SO_2) colour maps as well.

However, the limitations of this method consists of the fact that it combines the pixels from the O_2Hb and HHb regions creating a new image with the SO_2 displayed. A practical clinical version of this suggests that patients would have to undergo arterial occlusion, in

order to acquire both coefficients, which is not feasible for real world application.

The equation was input into MATLAB as a separate function, which was later called in the oximetry map script below.

The code for the equation can be seen through the link in Appendix .4, under the title of 'BeerLambertLaw1'.

4.1.2 Oximetry Map

A function was created in order to be able to apply the Beer-Lambert Law on each pixel within the regions of interest and therefore create an oximetry map.

For this, it was necessary to create variables for each wavelength that was going to be used during this process. Due to the camera only having four lenses and being able to accommodate only four wavelengths at once, it was necessary to identify the ones that could deliver the functionality needed for the system to be used in a clinical environment. This meant using the wavelengths that can provide accurate data when focusing on the relation between the visible wavelength range used and the tissue oxygenation. The only filters used at this point, were the ones decided upon in the previous chapter, Table 3.3. These wavelengths had to be exported inside this script in order to be of usage. As the camera has a filter limitation of four wavelengths, they were manually hard-coded inside the main NIPAD script (Appendix .4, Figure 2) as variables. Following that, the wavelengths were invoked into the oximetry map function and remained in use throughout.

Variables for each parameter needed were also created at the start of the function. This included: oxygenated haemoglobin (O_2Hb) and deoxygenated haemoglobin (HHb) for the second wavelength (λ_2), followed by $IsoO_2Hb$ and $IsoHHb$ for the isobestic wavelength (λ_1).

Due to the toe data having two wavelengths as λ_2 (Table 3.3), a condition was introduced at the beginning of the first `for` loop that assures the code will be executed for both sets of toe filters.

The same principle as in the 'Significance Test' script, was followed at the beginning of the code. The data import inside the code, was again based on the array from Table 3.1.

First, extraction of the individual pixels out of the ROI was performed. The initial concept was to attempt to isolate the regions of interest, overlay them (λ_1 and λ_2) for their respective filters and then create a mask for those regions, which would have eventually resulted in the oximetry map. However, whilst the ROI do have the same size, there were certain areas that were not aligned perfectly. There is still enough movement between each sample present, that

```
if m == 1 || m == 3 % Toe data, Without cuff => Oxygenated
 %Find positions for filters in array
    if m == 1
      if(str2num(S1(Epos(n,m)).name(2:4))== FilterToe) % Large difference toe filter
         imshow(uint8(S1(Epos(n,m)).data3)); %show image of toe without cuff
         %draw ellipse using known position
         e = drawellipse('Center','SemiAxes','RotationAngle','AspectRatio');
         BW = createMask(e); % Create mask for ellipse
         close gcf %close image
         [x y] = find(BW == 1); % Find every every pixel coordinate in the mask
         x1{1} = x';% Store coordinates in position 1 for x-axis
         y1{1} = y';% Store coordinates in position 1 for y-axis
         HHBO2HB = HHBO2HB  + 1;% Method to make sure loop was completed
      elseif (str2num(S1(Epos(n,m)).name(2:4))== IsoFilter) % Isobestic toe filter
```

Figure 4.1: Fragment of code used for re-drawing ellipses, finding and importing the pixel coordinates for BLL application.

when superimposed on top of each other, the regions simply do not fully match. Therefore, the most appropriate method was to use part of the code from the region of interest script (Chapter 3, Section 3.2.1) in order to determine their locations here.

Fragments of how this was completed are shown in Figure 4.1. Starting with m==1, the large difference oxygenated filter for the toe data, the exact same line used in the ROI script to draw ellipse was brought in. The ROI locations were imported from the 'Region of interest' creation code (Section 3.2.1), together with the binary masks that were formed. Due to their circular shape, some difficulties are expected when extracting data and finding the locations of each pixel. However, through the binary mask created, each pixel coordinate was found for the mask, on the image. After finding each pixel's coordinate, each of these were stored in position 1 for both x and y axes. These positions are very dependent on the images it correlates with, hence they are each stored in a different position number, depending on their image of origin.

The code continued to execute the same commands for the oxygenated isobestic filter from the toe data. Once it ended, it progressed to m==3 (Table 3.1), for both the oxygenated foot filters. For these samples, isolating the data was performed by cropping the region of interest out of the image, using the four known corner coordinates from the previous ROI script. For the deoxygenated data of both toes and foot, the same process explained above was carried out: a binary mask was created and pixel coordinates were extracted, isolating the data needed.

For the foot segmentation, similarly to when the regions were created, temporary ROI were formed with the known pixel positions and the system continued accordingly; the shape and the size of the segments remaining the same as in the original segmentations constructed.

Once the pixel coordinates from each region of interest were stored, Beer-Lambert Law

```
function [SO2img]=BeerLambertImgLoop(IsoO2HBimg,IsoHHBimg,O2HBimg,HHBimg, m,x1,y1)

if m == 4 % For foot data
    for x = 1:size(O2HBimg,1) % For the whole region of interest - indexes every pixel in x-axis
        for y = 1:size(O2HBimg,2) % In y-axis
            SO2img(x,y)=BeerLambert(IsoO2HBimg(x,y),IsoHHBimg(x,y),O2HBimg(x,y),HHBimg(x,y));% Apply BLL
        end
    end
else % For toe data
    minXval = min(cellfun(@length, x1)); % Find minimum total number of coordinates -> remove extra pixels
    for i = 1:minXval
        % Crop the ellipse out of the image and apply BLL
        SO2img = BeerLambert(IsoO2HBimg(x1{3},y1{3}),IsoHHBimg(x1{4},y1{4}),O2HBimg(x1{1},y1{1}),HHBimg(x1{2},y1{2}));

    end
end
end
```

Figure 4.2: Fragments of the function used to apply BLL on each pixel in every region of interest.

(BLL) was applied. For this, an inner function was created, which calls in the Beer-Lambert Law displayed in Equation 4.1.

The function used a loop to separate the foot and the toe data in two sections, as it can be seen in Figure 4.2. Starting with the foot data, the code was directed to index every pixel in the regions of interest, on both axes and then apply Beer-Lambert Law (Equation 4.1).

For the data containing the toe regions, the method applied was slightly changed. Most of the dissimilarities that appear during this process between the toe and foot data, is based on the fact that ellipse functions have more complex parameters compared to rectangles. Hence why extracting data becomes more challenging.

While the BLL function was being generated, an issue developed regarding the sizes of the ellipses. The MATLAB array created while the ROI were assigned, was double checked again and there was no apparent difference in their size. However, due to the constant displacement of the ellipse around each image, some of the pixels situated in the extremities of the circular object, seemed to have been changed. Therefore, some of the ROI objects were not of same coordinates with each other anymore.

The situation was corrected and adjusted, by firstly converting the arrays into cells, making the values needed more accessible. The minimum total number of coordinates among all regions
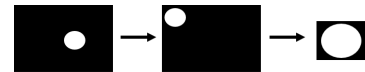
Figure 4.3: Process of cropping the ellipse binary mask for better visualisation, where the white dot represents the ellipse mask and its movement.

was found and the extra pixels in each of the other images were removed. This way every single value was successfully indexed, without exceeding the boundary conditions. Albeit, removing pixels is not ideal and there is a chance of having an effect on the intensity of the pixels for said region, however the written code also implemented a limit so that only the marginal pixels and the minimum amount necessary were removed.

The ROI masks were then cropped out of the whole image, to be able to have an aestheti-

cally pleasing shape, which was also zoomed in for better visualization. Figure 4.3 displays the cropping process and the necessary effect it had on the image. After the ellipses were brought to an equal size among all, the BLL inner function was applied to each pixel coordinate inside it.

The BLL function was applied pixel by pixel, on all regions of interest and for all filters. Due to the nature of the method, each dual-wavelength set creates a new image. The program imports the pixel value from the same position from each region of interest needed and combines the value through the Beer-Lambert Law formula, developing a new image. The new image displays the oxygen saturation of each pixel in that region of interest. In order to generate them visually, the MATLAB inherent function `imagesc` was implemented. The command applies a colour chosen to each pixel value in the array formed. In this case the colourmap colour vary from blue to red, the latter showing the highest oxygenation.

The entire code for this section can be seen through the link in Appendix .4, under the title 'Oximetry Map 1'.

4.2 Minimum/Maximum Pixel Oximetry Map

4.2.1 Beer-Lambert Law

The elementary standard form of measuring arterial oxygen saturation is by looking at the ratio between oxygenated haemoglobin and deoxygenated haemoglobin, using two wavelengths representing the different oxygenation levels. The saturation is defined by the equation:[31,49,50,52]

$$SO_2 = \frac{O_2Hb}{(O_2Hb + HHb)} \tag{4.2}$$

where O_2Hb is the oxygenated haemoglobin and HHb is the deoxygenated haemoglobin.

When applied in image processing, the formula examines the range within the area chosen, from minimum pixel value to the maximum. Thus, the equation was used for each image collected, with and without arterial obstruction, resulting in a final oximetry map for each oxygenated and deoxygenated image in part. O_2Hb represents the maximum pixel intensity from the region of interest, whereas HHb is the minimum pixel intensity value from the same region of interest.

The assumption made was that any changes between the total reflectance of oxygenated and deoxygenated areas, are in a 1:1 ratio. This may not be the case, however further

testing specifically regarding the background illumination and the affects it can have on both oxygenated and deoxygenated reflectance, is required for optimum development. To maintain the range, the isobestic wavelength data was applied as a normalisation factor.

This was put into practice by identifying a norm value from the isobestic data and applied it to the oxygen saturation. In order to make the resulted values comparable, the same normalisation factor was used across each image group, one for the foot image group and one for the toe group. Namely, from the first set of images that were to be taken, the mean pixel intensity value across all the regions of interest, for both foot and toe, was calculated. This resulted in one average value for toe data and one for the foot data, which were then divided by 255, the maximum intensity a pixel can have. Dividing the mean by 255, normalises the intensity range between 0 and 1 as a percentage value.

```
IsoMeanNormT = 0.154324156;
IsoMeanNormF = 0.276243316;
```

Figure 4.4: Isobestic normalisation values for both toe and foot data.

The final values used as the normalisation factor can be seen in Figure 4.4, where 'IsoMeanNormT' is the constant applied to the toe data and 'IsoMeanNormF' is the constant for the foot data. As aforementioned, these values were applied throughout the whole process that followed. Hence, the SO_2 equation was changed to implement the normalisation:

$$SO_2 = SO_2 + SO_2 \left(IsoMeanNorm - \frac{IsoMean}{255} \right) \qquad (4.3)$$

SO_2 is the oxygen saturation resulted from Equation 4.2. 'IsoMean' represents the mean of the specific region of interest for which the equation was applied, also normalised by 255. For example, if the code is generated for the cuffed foot main region of interest at $\lambda = 610nm$, then IsoMean would be mean intensity value of the cuffed isobestic wavelength, $\lambda = 520nm$. The isobestic value was then multiplied with the saturation, as it represents a percentage of the initial saturation level and then added to the oxygen saturation.

This equation was applied on each region of interest with the isobestic calibration. The code was written in a separate script, which was subsequently called in the oxymetry map function, explained in the following section.

The entire code for this section can be seen through the link in Appendix .4, under the title 'Beer-Lambert Law 2'.

4.2.2 Oximetry Map

The script created for this method was applied independently of the central NIPAD program (Appendix .4, Figure 2), mainly due to the fact that the analysis on the data was performed already whilst generating the dual-wavelength method (Section 4.1). Hence, in order to not execute the whole script again, a standalone function based on the processed data was constructed, for an automatic import.

To achieve this, an additional script was used. Throughout Chapter 2 which focused on method development, it has been explained how all the data obtained at each step, was formerly saved externally of MATLAB and also within a cell array in MATLAB. The main reason for also exporting the arrays with the data externally, was so that it can be used subsequently, if needed. Hence, an additional script was developed, which has the function of importing the data arrays in any other script that is independent of the main program.

The main reason for this script not being unified with the central NIPAD experiment, was primarily due avoiding any errors that might have been incurred within the main program execution. The operation of the whole code requires a substantial amount of time and would have made the process of establishing and clearing any flaws quite demanding and time consuming.

After automating the import of each data folder, from each former step, the focus was directed towards isolating the necessary values for the application of the updated Beer-Lambert Law.

Figure 4.5, illustrates the code used to extract the values needed from toe images without and with arterial occlusion (Table 3.1). Hence, the data obtained was the minimum and maximum values from each ROI of the filters chosen for the toe images, followed by the minimum, maximum and mean values of each region of interest belonging to the isobestic filter. The same code was executed again for the foot data and its segmentation.

After each value was obtained, the Beer-Lambert Law discussed in the previous section was applied, resulting into a singular oxygen saturation value for each region of interest of each image acquired. The raw values were exported in a spreadsheet friendly format. They can be displayed in any application such as Microsoft Office Excel.

In order to visualise the oxygen saturation, similarly to how it was developed previously for the dual-wavelength method, oximetry maps were created. The method used for creating these colour maps, is the same as explained in Section 4.1.2. The ROI code was used to be able to obtain pixel coordinates for each ellipse and the pixel coordinates of the rectangle

```
if m == 1 || m == 2 % Toe data
  if(str2num(S1(Epos(n,m)).name(2:4))== FilterToe) % Filter with largest
diffO2HBmax = double(S1(Epos(n,m)).max(i)); % Maximum value from region
    HHBmin = double(S1(Epos(n,m)).min(i)); % Minimumm value from region
    Comp = 1 + Comp;
   elseif (str2num(S1(Epos(n,m)).name(2:4))== IsoFilter) % Isobestic filter
   IsoO2HBmax = double(S1(Epos(n,m)).max(i)); % Maximum value from region
   IsoHHBmin = double(S1(Epos(n,m)).min(i)); % Minimum value from region
   IsoMean = S1(Epos(n,m)).mean(i);
  end
 end
```

Figure 4.5: Code written to extract the values needed for the application of BLL on each ROI.

regions.

Specifically for the ellipses, the reason it was necessary to be drawn again, was so that the binary mask could be generated. Creating the mask signified that pixel positions can be established and having the coordinates meant that BLL can be applied upon each pixel within the region, leading to an oximetry map for each image. As explained during the previous colour map code, for the foot data, localising the coordinates was much easier, due to the shape of the region having corners. Therefore, the areas needed were cropped and BLL was applied accordingly.

Once the pixel coordinates from each region of interest were stored, BLL was applied. The same function as in section 4.1.2 that ensures sizes match, was created for the application of the formula per pixel. The size conversion for ellipses was applied, as well as the isolation process highlighted in Figure 4.3.

The main disparity in the BLL equation, resided in the inputted values. When applying it pixel by pixel, the result produces a SO_2 value for each pixel in the region, as opposed to the value that was generated earlier per each region, whilst using the minimum and maximum intensities of the ROI.

Therefore, the equations (Equations 4.2 and 4.3) were changed slightly for the production of the maps. O_2Hb became the specific value of the pixel for which BLL was applied, whereas HHb continued to represent the minimum pixel intensity value from that region of interest. The isobestic constants remained the same and 'IsoMean' was exchanged with the specific pixel intensity value of the relevant isobestic region. Table 4.1 offers a formula visualisation of the different values automatically introduced for both SO_2, per region of interest and pixel by pixel.

After the BLL function was applied pixel by pixel, on all regions of interest and for all filters, the colour maps were created. Contrary to the first mapping technique, this method creates a cuffed and without cuff oximetry map image for each filter. Hence, each single ROI

Table 4.1: The values used for the production of SO_2 per ROI and pixel by pixel for the colour maps. The second column indicates the values used for BLL, whilst the third exhibits the ones applied from the isobestic filter for normalisation.

	Average SO_2 per ROI	Pixel by pixel SO_2
Beer-Lambert Law	O_2Hb = Maximum pixel value in ROI HHb = Minimum pixel value in ROI	O_2Hb = Pixel value at the specific location HHb = Minimum pixel value in ROI
Isobestic Filter λ normalisation	$IsoMeanNorm$ = Constant $IsoMean$ = Mean pixel value of ROI	$IsoMeanNorm$ = Constant $IsoMean$ = Pixel value at the specific location

forms a new image ROI after the application of BLL, displaying the oxygen saturation of each pixel.

The entire code for this section can be seen through the link in Appendix .4, under the title of 'BatchOximetryMap2'.

Chapter 5

Clinical Application

MSI is considered to have an outstanding potential regarding the enhancement of current medical techniques and instruments. Acquisition of spectral data through MSI, can deliver real-time information about the oxygenation of skin tissue. [23,31]

The studies investigating HSI/MSI and its abilities to collect spectral data and detect tissue oxygenation have yielded incredibly promising results. [6,54–57,64] Arterial occlusion to mimic vascular diseases was used in past research where clinical trials were not available, leading to reliable conclusions, however further studies need to be conducted in order to improve accuracy. [51,52,56,61,70]

The experiments demonstrated that HSI/MSI is useful in measuring and determining oxygenation changes in the vascular tissue, whilst also being reproducible. [31,51,52,56,61] Nevertheless, these studies also emphasised the importance of approaches that combine HSI/MSI together with other reliable techniques, such as thermal imaging, [52,70,80] pulse oximetry or other approved presumptive pulse tests and imaging techniques; in order to increase accuracy and repeatability. [23,31,56]

The method presented in this research uses MSI for detection of tissue devascularisation, whilst also attempting to improve the technical aspects of the device, making it less bulky, low-cost and portable.

After creating the algorithm for the extraction of tissue oximetry data, further testing was required to assess the performance of the filters with real-world examples that exhibit unpredictable changes in the background illumination.

This chapter will aim to discuss the efficiency of the software implementation, whilst analysing the data collected with the four filters: 520 nm, 540 nm, 610 nm, 640 nm.

5.1 Final Tests

Having discussed how the analysis method was constructed and the four wavelengths were chosen, the next step was to perform multiple tests on the filters to determine their validity. Testing the filters meant that the code created could be employed and investigated for further improvement.

Collecting real-world samples was beneficial, not only for the filter testing, but also for the ability to observe any similarities between different environments. Hence, data was procured indoors, where artificial lighting dominates in the background, but also outdoors, where natural lighting dominates in the background.

The instrumental arrangement was kept identical to the structure shown in Figure 2.3. The system used for the images collected in the laboratory can be seen in Figure 2.16, whereas the setup used for the outdoors samples, is displayed in Fig-

Figure 5.1: Outdoors image acquisition set-up.

ure 5.1. The latter set of images was collected on a cloudy summer afternoon, without the sun rays hitting the sample directly. For the purpose of this research, only daytime tests were carried out.

The four filters used (520 nm, 540 nm, 610 nm, 640 nm) were inserted into the camera slots and after the camera system was set, no other changes were made regarding the setup. The parameters, including focus and distances from sample to filter, remained constant all throughout image collection. For each environment, 15 sample sets were collected. Each set contained one image taken with arterial occlusion and one taken without the occlusion, for each filter. Hence, each set gathered contained eight images.

Similarly to the trial samples used for the code development, the XIMEA CamTool software was operated for the acquisition of images. The process was completed successfully, however there were a few dissimilarities within the software execution during image collection, that need to be considered.

Firstly, during the initial trial collection, the images for all the filters were saved as

Figure 5.2: Before (left image) and after (right image) flat-field correction comparison for image collected during the initial trial, at 640 nm without arterial occlusion.

a TIF format. However, when the current 30 sets of data were created, the images were automatically exported as a BMP format. Unfortunately, the difference was noticed later in the filter testing, when the code program was being executed. Although both extensions are specific for uncompressed formats with large arrays, the two types of files were analysed to ensure there was no significant difference.

In order to verify the difference in pixel value of the two formats, two identical images of a corner of a room were captured in a controlled illumination setting. One of the images was saved as a TIF and the other as a BMP format. When processed, the average pixel intensity of the TIF image was 172.5537, with a pixel standard deviation of 16.5541. Whereas, the BMP image had an average of 172.2950 and a standard deviation of 16.5333. The in-built MATLAB function `setdiff` was also applied, which returns the number of pixel differences between the two images. The set difference between the two images was of 92 pixels, accounting for the small variation in their averages. Moreover, considering the 1280x1024 image size, the set difference constitutes 0.01% of the total pixels. Therefore, the deviation from TIF to BMP had no impact on the final results regarding the pixel intensity. Hence, no major changes were applied to the code other than extending the recognition pattern towards a BMP format, alongside TIF. Moreover, the fact that all images collected for these final trials were batch saved as BMP, signified that any change would be consistent across all results, thus the pixel intensity fluctuation would still be visible accordingly.

The second inconsistency compared to the original images, was the difference in camera exposure. As it was seen in the first trial images (Appendix .5), there were a few wavelengths for which the images exhibit reflection from the light system, that was not greatly reduced even after flat-field correction, particularly for the toe images. Figure 5.2 shows an example

of such image from the initial trials, by comparing the image collected at 640 nm before and after flat-field correction. In this example, the reduction in the exposure is visible, but not fully corrected. A reason for this is due to the fact that the XIMEA software setup for exposure was left on automatic mode, to help compensating for all images.

Similarly, when the current samples were collected some of the images also appeared very bright, hence displaying an abundance of reflectance, mainly due to over-exposure. During the image capture, when the exposure level was monitored within the software, the automatic exposure was at 100.04 ms. This was for the whole image, before any image processing took place.

A normal effect from the pixels that are over saturated, is an increase in intensity values, which would inevitably give false results. To avoid any over-exposure, whilst also trying to remain consistent with the image capturing process, the exposure level was set to 43.74 ms across all acquisitions. Attempting a lower value than 43.74 ms appeared too dark, however a higher value seemed to still deliver a large amount of reflection. Therefore, the exposure was set to 43.74 ms for every image.

Applying the same exposure across all images, should still produce the same range of differences, assuming the sample is not over or under exposed. Exposure is environmental dependent, hence it is important that all images compared are of a similar exposure. Theoretically, only the initial images should be affected by the automatic exposure as in this instant, all images were taken at once with a unified exposure and gain. The effects the exposure change had on the images is explained more in-depth within the next section.

Following the completion of sample acquisition, a compressed version of the complete code program created was executed. The functions applied can be seen in Figure 5.3 and they focus on yielding results regarding the reflected intensity of each wavelength used. Hence, the 'Significance Test' script was not required to be enforced anymore.

Each set of samples, from each batch collected, indoors and outdoors, was subjected to the program created. The outcomes contain two sets of results regarding the oxygen saturation produced: one for the first method described in Chapter 4, and one for the second method.

Both sets of trial results for both BLL methods, including the images captured, data pre-processing and processing, can be visualised in Appendix .7.
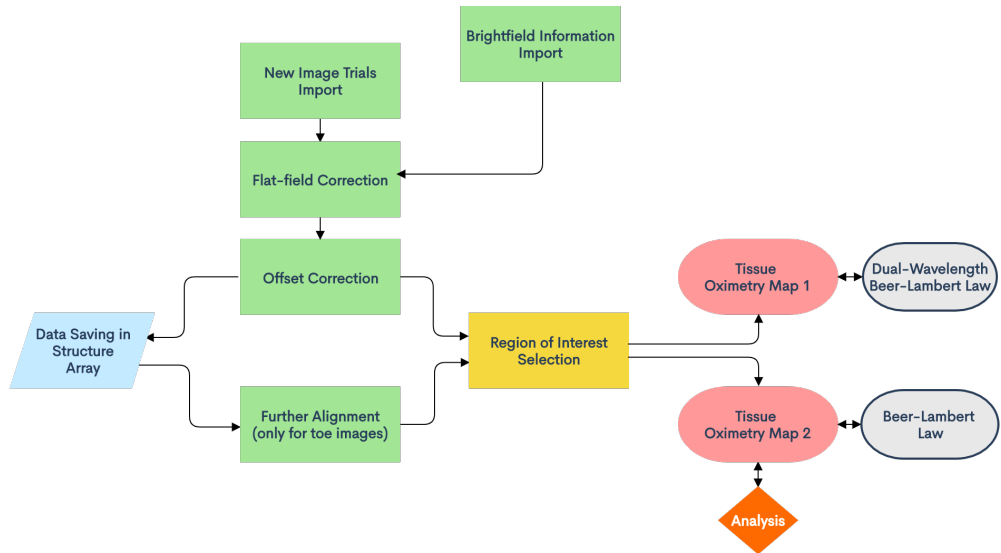
Figure 5.3: Updated MATLAB process applied to both final trials.

5.2 Results and Discussions

This section presents and discusses the principal findings of the application of the program upon the final test samples.

The first dual-wavelength BLL method mentioned in Section 4.1 focused on the application of BLL on the ROI selected, by using the extinction coefficients of the two wavelengths: isobestic and the one which exhibits a larger difference between O_2Hb and HHb. Although the results for this method were generated as well, due to the fact that it was not suitable for the aim of this research, only the second BLL (Section 4.2) was analysed.

The results of this method can be seen thorough the link in Appendix .7, within the 'SO_2' file for each trial from both environments.

The dual-wavelength method combines through Beer-Lambert Law the reflectance value of both images, with and without arterial obstruction from each wavelength, leading to an oxygen saturation value that represents both images. The purpose of the initial trials was to prove that there are differences between the intensities of cuffed and without cuff images. However, the first equation used requires for both oxygenated and deoxygenated coefficients to be known. Hence, translating this into a clinical version suggests that patients would have to undergo arterial occlusion, in order to acquire both coefficients. This would clearly be undesirable and unpractical, as the predominant functionality was for practitioners to be able to use the camera in a simpler manner. In real clinical environment, the ideal system is to be able to produce an oxygen saturation result immediately after image capture, instead of creating two oxygenation profiles, before and after arterial obstruction.

Therefore, the minimum/maximum pixel BLL method explained in Chapter 4, Section 4.2 was preferred and then adopted as the best formula of operation, having the entire focus directed towards enhancing this technique. The simplest form in which the data could be observed, was to examine the range of pixels, which is the intensity from the minimum to maximum point. This was subsequently adapted and normalised to provide the oxygen saturation. To make the data readable, the intensities were converted to a percentage range between 0 and 1, as explained in sections 4.2.1 and 4.2.2.

Each set of images has been processed accordingly, and the resulted regions of interest were subjected to BLL to obtain an oxygen spectrum. In addition to the pixel by pixel oxygen saturation colour maps that were created, the mean SO_2 values per each region of interest were averaged for each environment, indoors and outdoors. These values were then plotted for each filter, in order to be able to globally compare different oxygenation states from the data.

The results of the analysis provided by the toe data, are presented in Figure 5.4, where the final plots for each filter used are shown. The values seen are dependent on the average SO_2 value within the area of interest. Hence, the expected trend consisted of having a higher SO_2 value for the O_2Hb regions compared to HHb.

When examining the data from Figure 5.4a, it became evidently that the expected trend was not followed for the 540 nm filter. The first ROI has a higher mean SO_2 value for its oxygenated image, however the second and third regions display a higher SO_2 for the HHb images. Interestingly, for the fourth ROI the two switch again, however as explained in Section 3.2.2, the data within this region was not promising, due to environmental and experimental set-up variations. The values are also very close to each other, particularly for the second and fourth regions. The second ROI experiences overlap at a 48% SO_2.

Moving on to the second filter used for the toes, the results in Figure 5.4b exhibit some variation compared to the first wavelength. Keeping in mind that this filter was chosen as an alternative due to the high discrepancy within the fourth region of interest (section 3.2.2), the results displayed are more consistent and applicable to the initial filter deductions. The first three toe ROI present a higher SO_2 value for the O_2Hb images. As opposed to the previous wavelength, the fourth ROI reverses with a lower SO_2 value for its O_2Hb image and higher for the HHb.

The 640 nm wavelength clearly displays a consistent difference between O_2Hb and HHb, and although there is a shift in the fourth ROI, it was expected due to the quality of the

(a) Images collected indoors at 540 nm.

(b) Images collected indoors at 640 nm.

(c) Images collected outdoors at 540 nm.

(d) Images collected outdoors at 640 nm.
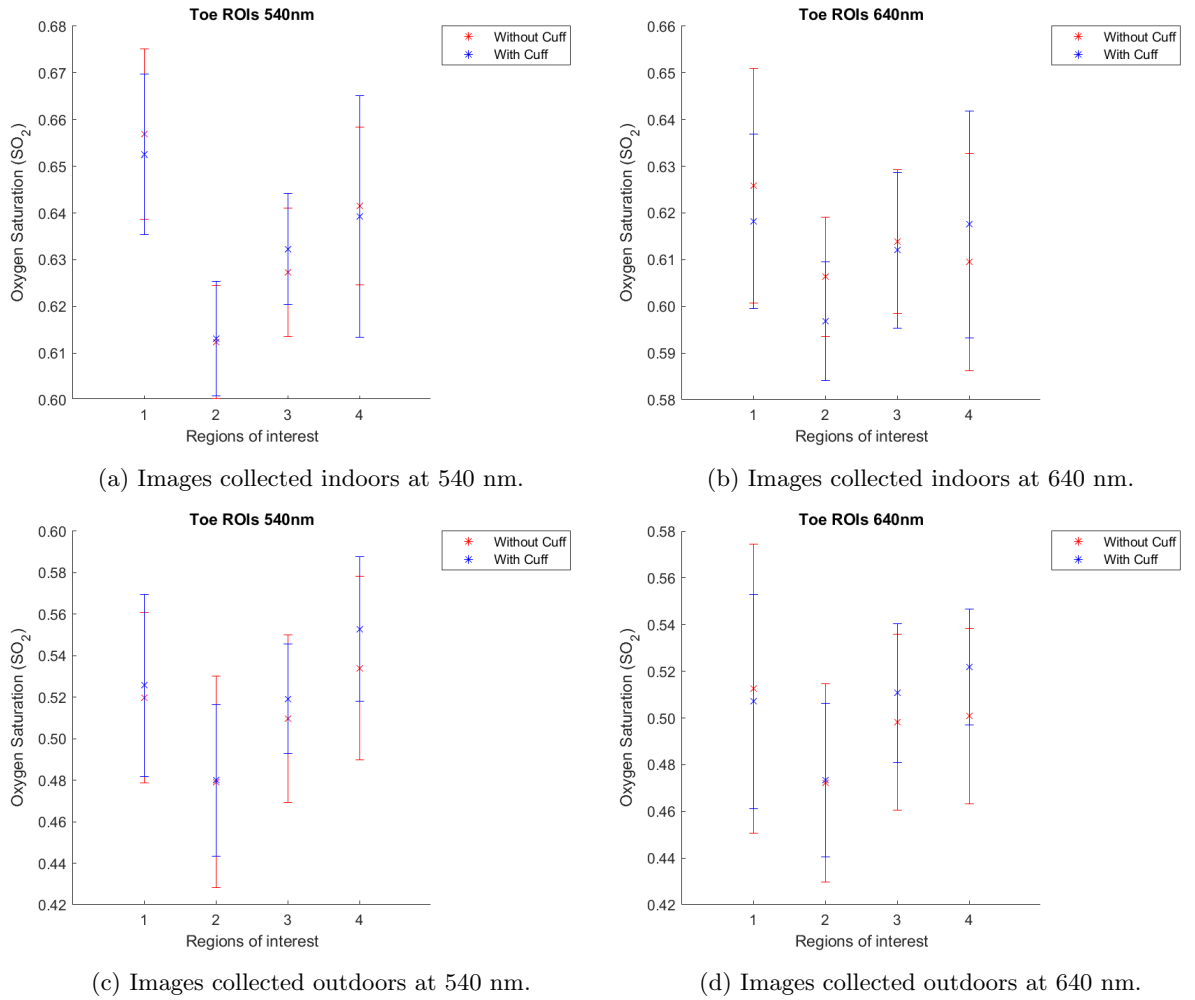
Figure 5.4: Average SO_2 values for the toe data, representing filters 540 nm and 640 nm, for all regions of interest, in both environments. Each individual value was calculated using the isobestic wavelength (520 nm) values, together with one of the two wavelengths mentioned above. In each graph, the red points represent the images without cuff occlusion, hence the oxygenated values (O_2Hb), whilst the blue stars represent the images with cuff occlusion, hence the deoxygenated values (HHb). The error bars on each plot represent the standard deviation of the data from each point.

area. Hence, it can be inferred that this filter produced more reliable results in comparison to 540 nm, however the range of difference between oxygenated and deoxygenated needs to be considered as well.

Turning now to the data from the images collected outdoors in natural lighting, in Figure 5.4c the averaged SO_2 values at 540 nm are depicted for each region. All four regions of interest show a higher averaged oxygen saturation for the images with cuff (HHb), leading to the decision that the filter does not function as desired, particularly in an uncontrolled environment. The reason why the outdoors environment produced slightly different HHb being higher, could be due to the fact that the sample may have had excessive background illumination, whilst the controlled environment had a more fixed illumination. The four ROI (Figure 5.4c) express a small variation between O_2Hb and HHb, with the largest being of

approximately 1% in the fourth region. The other differences are of less than 1% and the same overlap present in ROI 2 for the indoors 540 nm plot, is seen here as well only at 48% SO_2.

Figure 5.4d has a slightly higher SO_2 value for O_2Hb in ROI 1, however for the other three ROI HHb is higher. The same almost-perfect overlap for ROI 2 is present here as well.

There is a clear trend for the second region of interest, where the oxygenated and deoxygenated values seem to be extremely close. Moreover, the 540 nm filter is inconclusive as there is no clear consistency between O_2Hb and HHb trends. The reason for this could be due to the conflicting relation between the 540 nm filter and the isobestic filter of 520 nm, as they are very close to each other but were subjected to a formula that functions based on a larger ratio between its components. This signifies that the 540 nm - 520 nm filter combination, is simply not suitable for detecting the tissue oximetry at this point. If values continue to overlap, there is no clear delimitation between oxygenated and deoxygenated and having a definite reading is necessary for clinical applications.

Out of the two filters, the images collected in the laboratory at 640 nm, provide the best consistency, however the same filter presented some changes when used outdoors. This can simply say that having a controlled environment is most suitable when using this filter for the toes, however it also implies that its performance is not sufficient or that the technique needs further optimisation, for each step. However, testing the same process again, but on smaller regions of interest for better specificity, could also produce more accurate results.

As it can be seen in Figure 5.4, the error bars express the spread of the data for each filter. The deviation for all points are large, indicating a higher data variability from the mean value. The SO_2 values on the graphs draw attention to the predominantly low difference between cuff and without cuff images, which is also supported by the standard deviation bars overlap. The spread of data across the ROI seems to be relatively similar, demonstrating that the range of data is also close to each other for the filters used.

The data is mainly based on the mean pixel intensity of each ROI and the mean SO_2 per each region. On average results seem to exhibit similar intensities per each set, however it is also important to examine these fluctuations within the regions chosen.

In Appendix .8, Figures 3, 4, 5 and 6 depict the oximetry maps for all four regions of interest of the toe data, oxygenated and deoxygenated, collected with the 540 nm and 640 nm filters. The images shown in Figures 3 and 4 are from the sets collected indoors, in an environment with artificial lighting, whilst the maps from Figures 5 and 6 belong to the sets

collected outdoors, in an environment with natural lighting. As mentioned before, 15 image sets were acquired for each environment, however only 10 sets were used for yielding the final data. The reason being that, coincidentally, the created code program, resulted in errors for 5 image groups out of the 15 collected. The justification for this error is discussed further in the section.

Each O_2Hb - HHb pair displayed in Appendix .8, was selected out of the 10 image series from each environment. Hence, there are other 9 pairs left from each group. The sets from each environment are extremely similar to each other, which indicates the filters can produce repeatable results, even though there are other influencing factors. All the colour maps for each group of images, can be seen through the repository link in Appendix .7.

The colour maps only confirm the results from the graphs in Figure 5.4, as the lack of variation between the oxygenated and deoxygenated is also visible on the maps. Hence, similarities can be linked between the averaged SO_2 plots and the SO_2 colour maps. When examining Figures 5.5a and 5.5b (also avaialble in Appendix .8), it can be seen how similar the two are, with the O_2Hb region experiencing a slightly higher oxygenation. This matches the averages from Figure 5.4, however it is important to keep in mind that these maps represent only one of the sets made, whereas the mean SO_2 values indicate the oxygenation level across all image groups. More exactly, each map represents one of the 10 points used for each average SO_2 in the final plots (Figure 5.4), hence any changes that are seen on the maps of the individual O_2Hb and HHb are singularities. However, when combined together, the average resulted value for all sets can be somewhat different to the individual sets. Additionally, due to oxygenation levels being so similar, the maps offer limited ability to visualise differences.

As aforementioned, filter 640 nm (Figure 5.4b) seemed to exhibit the most accurate and consistent information. However when looking at Figure 4 in Appendix .8, where the regions are observed individually, the dissimilarities between O_2Hb and HHb seem almost imperceptible, which brings back the observations made earlier regarding the colour maps representing only one of the sets acquired, whereas the mean SO_2 values indicate the oxygenation level across all image groups.

The samples collected outdoors, such as the regions displayed in Figure 5.5c and 5.5d (all regions available in Appendix .8, Figure 5 and 6), exhibit more variation across the regions. It is noticeable for both filters how the pixels higher in SO_2 are more dispersed in comparison to the samples collected in the laboratory. This is more likely due to the fact that the illumination the foot receives outdoors was more scattered, whilst the lighting

(a) O_2Hb region of interest 1.

(b) HHb region of interest 1.

(c) O_2Hb region of interest 1.

(d) HHb region of interest 1.
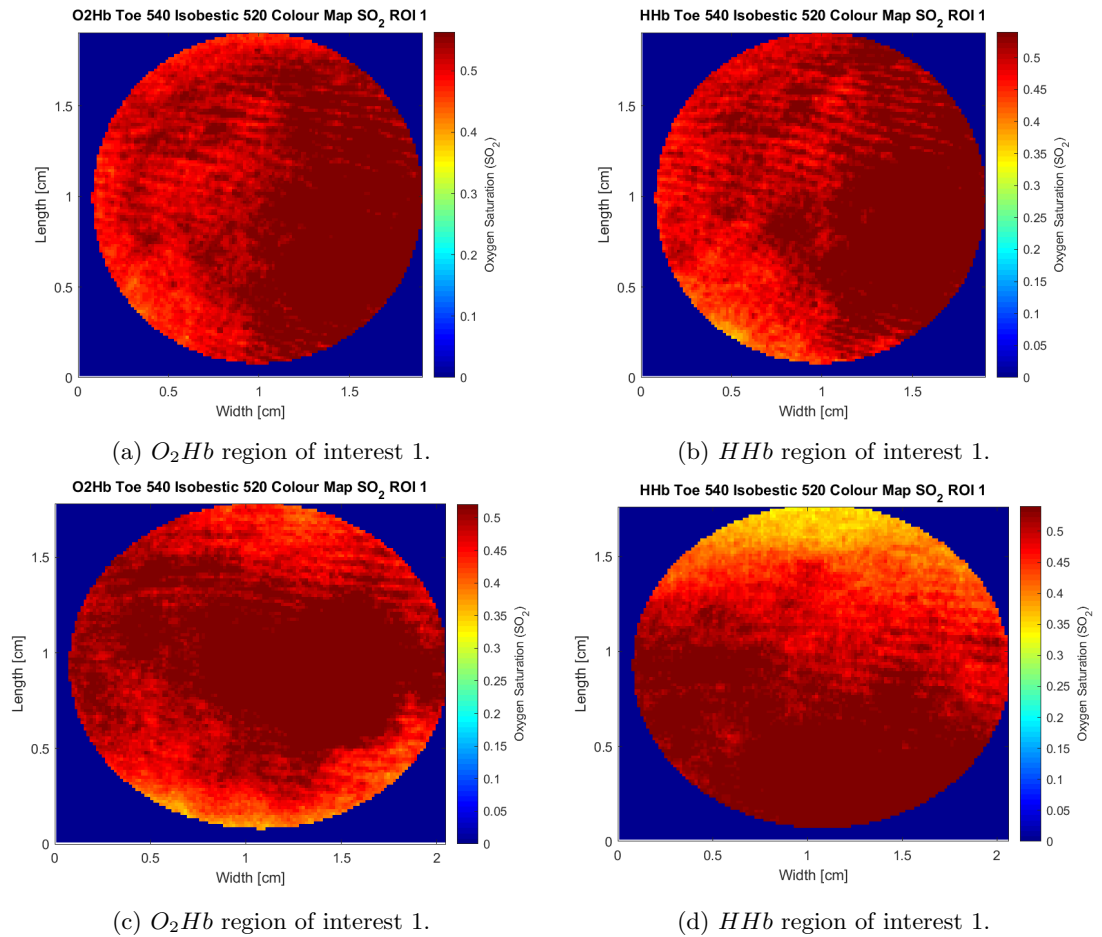
Figure 5.5: SO_2 oximetry colour maps (540 nm - isobestic 520 nm) for ROI 1 of the toe images, collected indoors (5.5a and 5.5b) and outdoors (5.5c and 5.5d), at 540 nm.

inside the laboratory was more localised. Surprisingly, although extra illumination and pixel dispersion occurs, when observing the final plots from Figure 5.4, it can be seen how for all data collected outdoors (Figure 5.4c and 5.4d), the SO_2 levels are lower by approximately 10% in comparison to the data collected inside the laboratory (Figure 5.4a and 5.4b).

The explanation might reflect into the initial pixel intensity used for BLL, which also leads to the level of exposure that the images were subjected to. However, when looking at the initial average pixel intensity resulted from each ROI before BLL application and displayed in Figures 7 and 8 from Appendix .8, it can be seen that the mean pixel intensity for the samples collected indoors is overall lower than for the ones collected outdoors. When examining the 540 nm and 640 nm wavelengths in both environments, it can be seen that the difference in pixel intensity between the outdoors ROI have an intensity closer to and over 100 a.u., whilst the ROI collected indoors have an overall pixel intensity closer to 50-60 a.u.. The plots from both figures display all four ROI from the second trial of each environment, indoors and outdoors. All the trials specific to each environment are seen to follow the same trend that appears in Figures 7 and 8 (Appendix .8), hence only one set for each environment

is displayed. The pixel intensity values of each ROI in each trial can be seen through the link in Appendix .5.

Therefore, the pixel intensity values did not factor into the fact that the average SO_2 values for the outdoors images were lower than for the images collected indoors. The reason for this final trend seems to derive from the BLL formula application and it could be the consequence of either the isobestic mean used, or the SO_2 equation (Equation 4.2). The latter could have had an effect due to the minimum and maximum intensity values that the formula used, indicating the difference between the spread of data between the oxygenated and deoxygenated. Hence, the SO_2 ratio between the samples collected outdoors and indoors was affected by the pixel intensity data spread within each region of interest.

(a) Main foot ROI collected indoors.

(b) Segmentation of ROI collected indoors.

(c) Main foot ROI collected outdoors.

(d) Segmentation of ROI collected outdoors.
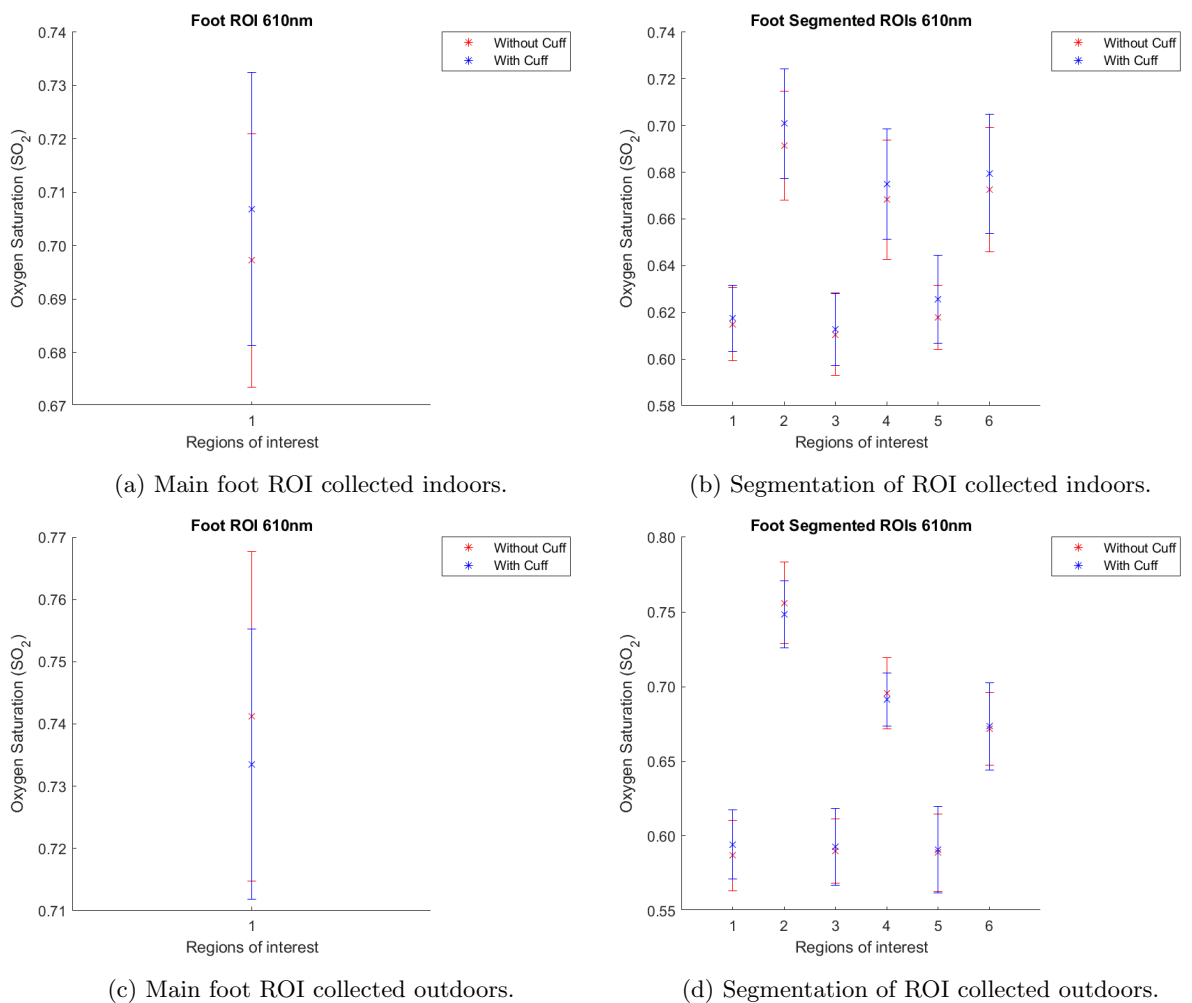
Figure 5.6: Average SO_2 values at 610 nm, for the main foot ROI and its segmentation, in both environments. Each individual value was calculated using the isobestic wavelength (520 nm) values, together with the data from 610 nm. In each graph, the red points represent the images without cuff occlusion, hence the oxygenated values (O_2Hb), whilst the blue stars represent the images with cuff occlusion, hence the deoxygenated values (HHb). The error bars on each plot represent the standard deviation of the data from each point.

Moving on to the final sets of images focusing on the foot artery, the results of the analysis

are presented in Figure 5.6, where the final average SO_2 plots for the 610 nm filter and the 520 nm isobestic filter are shown.

The expected trend was the same for these samples as well, with a higher SO_2 value for the O_2Hb regions compared to HHb. However, similarly to the previous results for the toe data, the outcome did not follow the trend.

Figures 5.6a and 5.6b display the average SO_2 values for both oxygenated and deoxygenated ROI from the foot images across all sets, collected in a controllable environment at 610 nm. Across all the sets collected indoors, the main foot ROI exhibits a higher SO_2 average (Figure 5.6a) for the deoxygenated image than for the oxygenated one, with a small difference between the two. This is also demonstrated in Figure 5.6b, where the segmented ROI have a higher deoxygenated SO_2 value as well.

Additionally, when looking at the six divisions, a visible separation can be seen between the left side of the main region and the right side. The dissimilarities between the two sides appeared mostly due to the larger size of the ROI and the natural position of the foot, leading to more shading on one side and more variation for the pixel intensity values. These differences were also discussed before when the final four filters were chosen, hence the resulted SO_2 values reinforce these differences. Segments 1, 3 and 5, which represent the left side of the rectangle region are closer in SO_2 value at an approximate of 62% saturation; whereas segments 2, 4 and 6 display a SO_2 value closer to 68 - 70%.

On the other hand, Figure 5.6c which represents the average SO_2 values at 610 nm in an uncontrollable environment, exhibits a higher oxygen saturation for the oxygenated, without cuff, image. However, the difference between O_2Hb and HHb of 0.01% is so small, that producing significant results becomes unlikely. Moreover, when examining the average values for the segmented version in Figure 5.6d, it can be seen how all divisions are almost perfectly overlapping, therefore yielding no conclusive results. Similarly to the sample collected indoors, the segmentation for the outdoors data is also clearly defined between left side and right side of the rectangle. Segments 1, 3 and 5 are closer in SO_2 value at an approximate of 50% saturation; whereas segments 2, 4 and 6 display a SO_2 value closer to 70 - 75%.

Although these results prove the dissimilarities between various regions and also within the regions it must be noted that, similarly to the toe data, there is a lack of significant SO_2 difference between oxygenated and deoxygenated values. This is also reinforced by the overlap of the error bars in each graph, which represent the standard deviation. The spread of data seems to also be similar between the indoors and outdoors samples, particularly for

the main ROI and the two sides of the segmented rectangle.

As can be observed in Figure 5.7, the examination of the pixel by pixel saturation maps found no significant differences between O_2Hb and HHb, complying with the results found in the average SO_2 graphs from Figure 5.6 and similarly to the toe data maps.

(a) O_2Hb ROI of the foot image, collected indoors.

(b) HHb ROI of the foot image, collected indoors.

(c) O_2Hb ROI of the foot image, collected outdoors.

(d) HHb ROI of the foot image, collected outdoors.
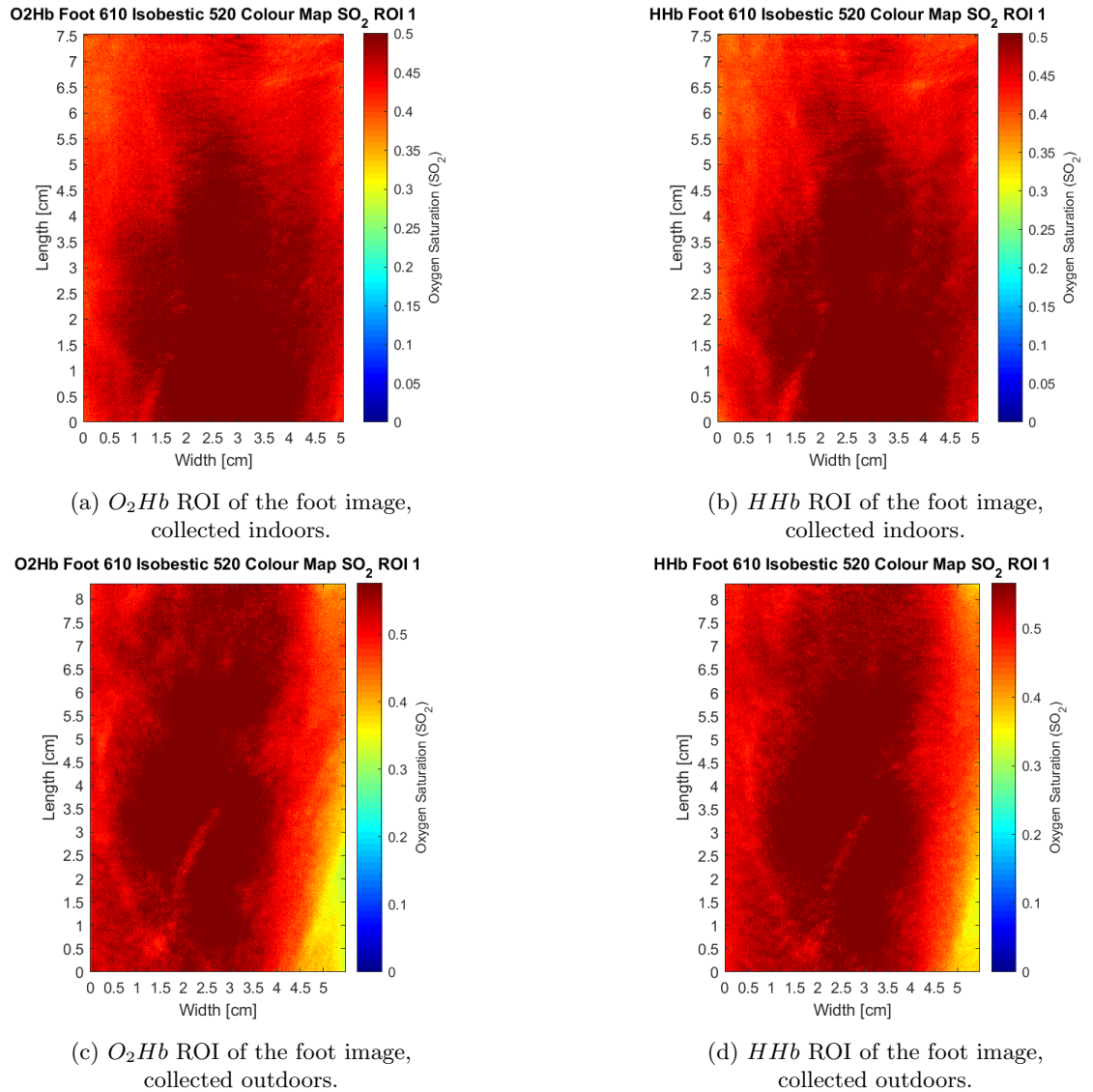
Figure 5.7: SO_2 oximetry colour maps (610 nm - isobestic 520 nm) for the main ROI of the foot data, collected in both environments at 610 nm, with cuff occlusion (deoxygenated - HHb) and without cuff occlusion (oxygenated - O_2Hb).

Each set collected in both environments has an individual O_2Hb and HHb colour map for each ROI, hence only the maps from the first trial from each environment are shown. Moreover within each setting, the resulted SO_2 maps are extremely similar with each other, which demonstrates the lack of variability between the oxygenated and deoxygenated SO_2 values seen in Figure 5.6. The maps from all trials can be visualised through the link in Appendix .7.

Figure 5.7 (also available in Appendix .8, as Figure 9) displays the oxygenated and de-

oxygenated SO_2 colour maps associated with the main foot ROI from the first set, collected in each environment, indoors and outdoors. The segmentation colour maps of the regions shown in Figure 9 can also be found in Appendix .8, where Figures 10 and 11 represent the left (ROI 1, 3 and 5) and right (ROI 2, 4 and 6) sides of the ROI image collected in a controllable environment, whilst Figures 12 and 13 display the left and right side of the ROI image collected in an uncontrollable environment. All the colour maps shown, have been set to a upper quartile limit of 75% to avoid extremely high values, with a range of 0 - 1 for the SO_2 percentage values. The samples collected outdoors (9), appear to exhibit more dispersion across both oxygenated and deoxygenated regions. However, the SO_2 values are similar with no clear and conclusive separations between them.

In summary, these results show a certain functionality regarding the camera and the processing method, however it can be argued that the four chosen filters were not suitable for the final aim. The whole process has many variables that need to be taken into consideration. To start with, the most noticeable aspect concerning the final filter results explained previously, is the lack of difference between the oxygenated and deoxygenated SO_2 values. Other than the isobestic filter, which was purposely chosen as a wavelength with no change in reflectance between O_2Hb and HHb, the other three wavelengths: 540 nm, 640 nm and 610 nm, have to exhibit a clear difference between the two in order to draw conclusive results regarding the oxygen saturation of the tissue. The final SO_2 values for both sample areas (Figures 5.4 and 5.6), showed that the variations within all four filters were inconsistent with the initial aim. The differences between O_2Hb and HHb are at an approximate 1%, sometimes experiencing complete overlap or having the deoxygenated image display a higher SO_2 level than the oxygenated one.

The explanation for the similar SO_2 levels, is mainly based on the exposure used during the acquisition of the images. Looking at the overall project there are two points to consider, one being the original data which the code was created for and also used to isolate the final four filters, whilst the other being the second tests collected to help yield and interpret extra findings for further optimisation.

When the initial images were acquired, the exposure setting within the software was automatic and some of the images collected seemed to be over-exposed in certain areas. Nevertheless, as explained above in Section 5.1, when the test images with the final filters were acquired they appeared even more over-exposed, hence the exposure was lowered and set to 43.74 ms. However, after the images were collected and examined they appeared dimmer

and under-exposed. It might be that the reason for perceiving the images during acquisition differently, is based on elements regarding the software display window. This requires further testing of XIMEA, the image acquisition program. Therefore, by trying to set an exposure limit to suit the areas of interest, the images ended being under-exposed.

Under-exposing the images has also had an effect on some of the trials taken in both environments. During the previous section of this chapter, it was explained how 15 trials were performed for each environment, however only 10 were used. Coincidentally, 5 trials out of the 15, in both data sets have resulted in errors when the algorithm was generated. This is due to the fact that the resulted oxygenated and deoxygenated SO_2 values for each ROI were so close together, leading to a lack of distinguishable differences and preventing the production of an SO_2 value. Moreover, the fact that the images were not subjected to enough exposure can induce pixel intensity loss, which can create the lack of differences.

As mentioned previously, spectral reflection due to over-exposure was seen for the initial images collected (Appendix .5) and the selection of the four filters was based on that data, which will automatically created a change in pixel intensity, leading to an inaccurate exposure process altogether. This is part of an exploratory process and whilst it does confirm software limitations, there is a clear possibility of further optimisation.

Moreover, the fact that the isobestic wavelength, 520 nm, was not displaying a consistent lack of variation between O_2Hb and HHb across all sets (Figures 5.4 and 5.6), confirms that the wavelength was not accurately selected for its purpose. The isobestic wavelength was meant for normalisation and comparison purposes between image sets, hence it should yield the same intensity values.

Nonetheless, even if 520 nm is the correct isobestic wavelength or if the other filters can potentially deliver conclusive information, it is uncertain at this point mainly due to the over/under exposure and the background illumination affecting the pixel intensity.

When observing the wavelengths used in literature (Table 1.1), it can be seen that they fit into most ranges, however it is difficult to choose a specific waveband, when most studies are performed within a hyperspectral range or using a commercial device. Therefore, considering the algorithm method was completed, although it still needs further optimisation, the most appropriate method of inspecting and re-selecting the filter choices, would be to repeat the process of testing the entire wavelength range available. Whilst doing so all variables should be taken into consideration, including exposure and improving illumination. LED lighting was used as the illumination system due to the fact that these types of lamps are more commonly

found in a medical practice. However, the effects this might have on the image collection, with the current set up, are unknown. The light spectrum of the LED light can aid in optimising any variations in the spectral characteristics of the illumination used. Therefore, the spectral profile of the LED lamp used should be acquired as it could help increase uniformity and comparability between samples.

On the other hand, there could be that certain filters are better for specific environmental light, however considering that the camera is limited to 4 wavelengths, which in a real-life scenario means that they cannot be changed, multiple testing would need to be performed.

The main issues that appeared, were based on certain assumptions that were taken in order to be able to create an algorithm for tissue oxygenation, produce results and then further optimise. The first variable issue was for the exposure and spectral reflectance created, which was automatic initially and most likely ended up creating false results. Taking this into consideration could mean that a manual approach might be beneficial, particularly at this stage in the research until the automatization can be optimised appropriately. Handling experimental tests manually, could signify higher ability to control and optimise certain settings and parameters step-by-step, therefore leading to a higher consistency when acquiring and analysing data.

Secondly, another issue would be the assumption that all samples were collected at the same time. As a result of the initial instrumental and technical set up, it was not possible for the data to be collected concomitantly, leaving space for variables to arise between sample collections, such as change in illumination and in the position of the sample, hence decreasing comparability.

Although the samples have been subjected to alignment process for a precise overlap, because of the notably natural movement of the foot during the cuffing process, the overlap was not exactly intact. Moreover, not having a flawless overlap, lead to challenges with the ROI selection and placement.

For each trial, every ROI had to be created and moved in order to match toe/foot area needed. This can cause issues with pixel intensity, as it is highly unlikely to be able to place the ROI manually in the same location for toes/foot. Hence, it can become a challenge with ellipses in particular, regarding losing or gaining pixels. In Chapter 4, it was discussed how marginal pixels in ellipses were lost in order to apply BLL. The reason for this was the overlap of the sample, as it required displacement of ROI, therefore changing their rotational angle and axes. Thus, the assumption was made that, although there has been pixel loss the ellipses

still ended at an equal size.

Despite results not being completely satisfactory at this stage due to different variables and assumptions, there is a clear conclusion regarding the functionality of the camera and the detection of reflectance, making it promising for further development. The method generated not only has applicability in the medical industry, but it is also repeatable and with the new code created, the following tests and trials can reveal more potential and abilities in creating a low-cost, portable spectral imaging device.

Chapter 6

Future perspectives and conclusions

The application of spectral imaging in medical care, can clearly lead to development of early-stage diagnosis and monitoring of vascular diseases. Hence, this research is trying to not only advance towards making HSI/MSI into a recognisable technique in medical care, but also deliver, a cost-effective, portable technology suitable for clinical delivery.

The research presented has developed a technical set-up, acquired images with and without arterial obstruction, created an entire code for the image processing in order to select four preliminary wavelengths (520 nm, 540 nm, 610 nm, 640 nm) and performed multiple trials in two different environments with the selected filters.

There are many existing variables that still need to be examined and corrected. Starting with the light exposure, which would require further testing using XIMEA, the software for image acquisition, but also looking into alternative lighting systems that may have a better light selectivity than the LED lights used here. Another issue with XIMEA, is that at the moment the software only allows one image to be collected at a time, hence each image with and without cuff is acquired one after the other, decreasing comparability. Due to time restraints, this was not amended at this stage, however a script can be written within the software, to a allow for collection from all four lenses at the same time.

Secondly, a way to overcome foot displacement for better ROI overlap needs to be investigated. Keeping the foot still in real clinical scenarios is not a solution, however when it comes to isolate the ROI, the same pixels must be selected. Hence, the code should be updated with a particular alignment automatisation, which needs to be implemented.

Thirdly, the ranking system used for selecting the four filters could be enhanced to have a higher specificity. However, not all the images from which the filters were chosen were exposed perfectly, thus it may be that the reason why the filter selection was inconsistent was because

of the exposure settings. The main method of improving the filter selection process, is to simply perform more tests, particularly clinical trial tests. Clinical trials would result in a slight change of BLL by implementing the extinction coefficients of other chromophores, such as melanin, extending the sensitivity of the technique. Having a larger data set of patients, in more variable conditions, would steer towards an improvement in establishing the limitations of the technique and could lead to answers regarding the influence that different patients, ages, skin types or even environmental parameters could have on the final results. However, before performing clinical trials, the method should undergo extra testing with a tissue phantom with known absorption properties as well. This could aid in the consistency during data acquisition and analysis.

The whole process, including the written code, requires more optimisation by testing the limitations of the camera and the process used. The system is not perfected yet and all the variables mentioned before, as well as the code, can create issues; nevertheless both the camera and the system have a high testing limit and there are many more trials that need to be performed for a full optimisation. Unfortunately, it may be that at this stage the technique does not have the sensitivity needed, however testing further filters will eventually reach it. An additional step that should be considered in future developments is the applicability of non-visible wavelengths, as they may provide a better understanding of the technique and final results.

It can therefore be suggested that multiple tests should be performed again with all the filters, whilst paying attention to all the variables that were disregarded during the first trials. There will always be some variability until the system is accurately enhanced. Although the process of optimisation is gradual and it prerequisites certain steps to be achieved, an entire program has been completed for the project. Thus the future procedures for augmenting the system will be more accessible regarding data collection and less time consuming.

Other future perspectives include the use of MSI together with another technique that measures tissue oximetry, such as pulse oximeter. Using an instrument that is on the market, even in contact with skin such as the pulse oximeter, would be beneficial in measuring and controlling the oxygenation.[49] Another option would be to investigate the hypoxia state caused by holding breath temporarily and its opposite, hyperoxygenation, that could be achieved by rapid breaths in quick succession, and compare the results against the ones from arterial occlusion or with a tissue phantom. Moreover, the applicability of thermal imaging together with MSI has been studied before, with successful outcomes.[52,70,80]

The technical set-up will also be changed in order to become easily portable. This includes creating a hand-held camera support and also finding an alternative for the long and heavy HDMI cables that are currently in use. In the distant future, enhancement regarding the use of the software program should also be discussed, such as developing a graphical user interface and maybe even using a neural network, which can input the written program to improve applicability and repeatability.

All in all, the system created and the results yielded can provide proof of principle regarding the feasibility of the technology presented. The detection of oxygenated and deoxygenated haemoglobin with MSI is already known to offer a reliable way to detect PAD. [23,31] The preliminary tests performed with coloured liquid, confirm the camera's high proficiency in distinguishing tissue reflectance. Although, the results of the preliminary four filters (520 nm, 540 nm, 610 nm, 640 nm) were not highly conclusive, the method still opens an opportunity for the performance of further system optimisation. The development of a multispectral imaging device, that not only is non-invasive, but also light weight and low-cost, can deliver a reproduceable method in order to detect and monitor tissue oxygenation in clinics and at the patient's residence.

List of Figures

List of Tables

Bibliography

[1] G. Pocock, C. D. Richards and D. A. Richards, *Human Physiology*, OUP Oxford, 5th edn., 2017.

[2] J. G. Betts, T. J. College, P. Desaix, J. E. Johnson, J. A. Wise, M. Womble and K. A. Young, *Anatomy & Physiology*, OpenStax, 2017.

[3] E. R. Mohler and B. Annex, *Regenerative Medicine for Peripheral Artery Disease*, Academic Press, 2016, p. 180.

[4] R. Donnelly and N. J. M. London, *ABC of Arterial and Venous Disease*, Wiley, 2000.

[5] R. L. Morley, A. Sharma, A. D. Horsch and R. J. Hinchliffe, *BMJ (Online)*, 2018, **360**, DOI: https://doi.org/10.1136/bmj.j5842.

[6] D. Yudovsky, A. Nouvong and L. Pilon, *Journal of Diabetes Science and Technology*, 2010, **4**, 1099–1113.

[7] A. J. Boulton, *Medicine (Baltimore)*, 2010, **38**, 644–648.

[8] M. Clokie, A. L. Greenway, K. Harding, N. J. Jones, K. Vedhara, F. Game and K. K. Dhatariya, *Diabetic Medicine*, 2017, **34**, 305–315.

[9] L. Norgren, W. R. Hiatt, J. A. Dormandy, M. R. Nehler, K. A. Harris and F. G. Fowkes, *Journal of Vascular Surgery*, 2007, **45**, 5–67.

[10] W. S. Jones, M. R. Patel, D. Dai, S. Vemulapalli, S. Subherwal, J. Stafford and E. D. Peterson, *American Heart Journal*, 2013, **165**, 809–815.e1.

[11] V. Grimaldi, C. Schiano, A. Casamassimi, A. Zullo, A. Soricelli, F. P. Mancini and C. Napoli, *Clinical Physiology and Functional Imaging*, 2016, **36**, 165–178.

[12] N. R. Barshes, E. Flores, M. Belkin, P. Kougias, D. G. Armstrong and J. L. Mills, *Journal of Vascular Surgery*, 2016, **64**, 1682–1690.e3.

[13] A. N. Bashkatov, E. A. Genina, V. I. Kochubey and V. V. Tuchin, *Journal of Physics D: Applied Physics*, 2005, **38**, 2543–2555.

[14] Y. Rabi, D. Kowal and N. Ambalavanan, in *Blood Gases: Technical Aspects and Interpretation*, Elsevier Inc., 2017, pp. 80–96.e3.

[15] A. Jubran, *Critical care (London, England)*, 2015, **19**, 272.

[16] J. N. Kwon and W. B. Lee, *Journal of the Korean Surgical Society*, 2012, **82**, 94–100.

[17] D. Jawahar, H. R. Rachamalla, A. Rafalowski, R. Ilkhani, T. Bharathan and N. Anandarao, *Angiology*, 1997, **48**, 721–724.

[18] J. Ena, C. R. Argente, V. González-Sánchez, N. Algado, G. Verdú and T. Lozano, *Journal of Diabetes Mellitus*, 2013, **03**, 79–85.

[19] E. D. Chan, M. M. Chan and M. M. Chan, *Respiratory Medicine*, 2013, **107**, 789–799.

[20] E. S. Varaki, G. D. Gargiulo, S. Penkala and P. P. Breen, *BioMedical Engineering Online*, 2018, **17**, 1–27.

[21] P. Normahani, C. Mustafa, N. J. Standfield, C. Duguid, M. Fox and U. Jaffer, *Journal of Foot and Ankle Research*, 2018, **11**, 29.

[22] NICE, *Recommendations — Peripheral arterial disease: diagnosis and management — Guidance — NICE*, `https://www.nice.org.uk/guidance/cg147/chapter/Recommendations#diagnosis` (last accessed on 14/05/20).

[23] G. Lu and B. Fei, *Journal of Biomedical Optics*, 2014, **19**, 10901.

[24] V. V. Tuchin, *Tissue optics: Light scattering methods and instruments for medical diagnosis: Third edition*, SPIE Press, 2015.

[25] V. V. Tuchin, *Journal of Biomedical Photonics & Engineering*, 2015, **1**, 3–21.

[26] M. F. Yang, V. V. Tuchin and A. N. Yaroslavsky, in *Principles of light-skin interactions*, Springer London, 2009, pp. 1–44.

[27] G. V. Baranoski and T. F. Chen, *Agache's Measuring the Skin: Non-invasive Investigations, Physiology, Normal Constants: Second Edition*, 2017, 85–98.

[28] T. Lister, P. A. Wright and P. H. Chappell, *Journal of Biomedical Optics*, 2012, **17**, 0909011.

[29] A. N. Bashkatov, E. A. Genina and V. V. Tuchin, *Journal of Innovative Optical Health Sciences*, 2011, **4**, 9–38.

[30] E. Salomatina, B. Jiang, J. Novak and A. N. Yaroslavsky, *Journal of biomedical optics*, 2006, **11**, 064026.

[31] L. E. MacKenzie and A. R. Harvey, *Journal of Optics*, 2018, **20**, 063501.

[32] S. Prahl, *Optical Absorption of Hemoglobin*, 1999, `https://omlc.org/spectra/hemoglobin/` (last accessed on 15/08/222).

[33] S. L. Jacques, *PHYSICS IN MEDICINE AND BIOLOGY Phys. Med. Biol*, 2013, **58**, 37–61.

[34] M. Vidal and J. M. Amigo, *Chemometrics and Intelligent Laboratory Systems*, 2012, **117**, 138–148.

[35] M. Hébert, R. D. Hersch and P. Emmel, in *Fundamentals of Optics and Radiometry for Color Reproduction*, John Wiley & Sons, 2015, pp. 1021–1077.

[36] S. M. K. M. P. Mahajan, *Asian Journal of Computer Science Engineering*, 2016, **2**, 6–10.

[37] M. Aboras, H. Amasha and I. Ibraheem, *American Journal of Biomedical and Life Sciences*, 2015, **3**, 29–33.

[38] P. Escribano, T. Schmid, S. Chabrillat, E. Rodríguez-Caballero and M. García, in *Optical Remote Sensing for Soil Mapping and Monitoring*, ed. P. Pereira, E. C. Brevik, M. Muñoz-Rojas and B. A. Miller, Elsevier Inc., 2017, pp. 87–125.

[39] J. M. Amigo, H. Babamoradi and S. Elcoroaristizabal, *Analytica Chimica Acta*, 2015, **896**, 34–51.

[40] M. A. Calin, S. V. Parasca, D. Savastru and D. Manea, *Applied Spectroscopy Reviews*, 2014, **49**, 435–447.

[41] G. Elmasry, M. Kamruzzaman, D.-W. Sun and P. Allen, *Critical Reviews in Food Science and Nutrition*, 2012, **52**, 999–1023.

[42] G. J. Edelman, E. Gaston, T. G. van Leeuwen, P. J. Cullen and M. C. G. Aalders, *Forensic Science International*, 2012, **223**, 28–39.

[43] F. Rosi, C. Miliani, R. Braun, R. Harig, D. Sali, B. G. Brunetti and A. Sgamellotti, *Angewandte Chemie International Edition*, 2013, **52**, 5258–5261.

[44] S. T. Monteiro, Y. Kosugi, K. Uto and E. Watanabe, *IASTED Visualization, Imaging and Image Processing*, 2004, 6.

[45] H. Akbari, Y. Kosugi, K. Kojima and N. Tanaka, *2009 Annual International Conference of the IEEE Engineering in Medicine and Biology Society*, 2009, 1461–1464.

[46] S. V. Panasyuk, S. Yang, D. V. Faller, D. Ngo, R. A. Lew, J. E. Freeman and A. E. Rogers, *Cancer Biology & Therapy*, 2007, **6**, 439–446.

[47] Q. Wang, Q. Li, M. Zhou, Z. Sun, H. Liu and Y. Wang, *PLOS ONE*, 2017, **12**, e0178499.

[48] R. V. Maikala, *International Journal of Industrial Ergonomics*, 2010, **40**, 125–134.

[49] M. Nitzan, A. Romem and R. Koppel, *Medical Devices: Evidence and Research*, 2014, **7**, 231–239.

[50] Y. Rabi, D. Kowal and N. Ambalavanan, in *Blood Gases: Technical Aspects and Interpretation*, Elsevier Inc., 2017, pp. 80–96.e3.

[51] U. Rubins, A. Grabovskis, J. Cimurs, Z. Marcinkevics and A. Caica, author, 2018.

[52] I. Saknite, A. Grabovskis, S. Kazune, U. Rubins, Z. Marcinkevics, K. Volceka, E. Kviesis-Kipge and J. Spigulis, author, 2017.

[53] Hypermed, *HyperView™*, https://hypermed.com/products/ (last accessed on 12/06/20).

[54] R. L. Greenman, S. Panasyuk, X. Wang, T. E. Lyons, T. Dinh, L. Longoria, J. M. Giurini, J. Freeman, L. Khaodhiar and A. Veves, *The Lancet*, 2005, **366**, 1711–1717.

[55] A. Nouvong, B. Hoogwerf, E. Mohler, B. Davis, A. Tajaddini and E. Medenilla, *Diabetes Care*, 2009, **32**, 2056–2061.

[56] B. J. Sumpio, G. Citoni, J. A. Chin and B. E. Sumpio, *Journal of Vascular Surgery*, 2016, **64**, 1066–1073.

[57] J. A. Chin, E. C. Wang and M. R. Kibbe, *Journal of Vascular Surgery*, 2011, **54**, 1679–1688.

[58] S. P. Chong, C. W. Merkle, C. Leahy, H. Radhakrishnan and V. J. Srinivasan, *Biomedical Optics Express*, 2015, **6**, 1429–1450.

[59] R. Guay-Lord, X. Attendu, K. L. Lurie, L. Majeau, N. Godbout, A. K. E. Bowden, M. Strupler and C. Boudoux, *Journal of Biomedical Optics*, 2016, **21**, 116008.

[60] Y. Khan, D. Han, A. Pierre, J. Ting, X. Wang, C. M. Lochner, G. Bovo, N. Yaacobi-Gross, C. Newsome, R. Wilson and A. C. Arias, *Proceedings of the National Academy of Sciences of the United States of America*, 2018, **115**, E11015–E11024.

[61] A. A. Bruins, D. G. Geboers, J. R. Bauer, J. H. Klaessens, R. M. Verdaasdonk and C. Boer, *Journal of Clinical Monitoring and Computing*, 2020, DOI: 10.1007/s10877–019–00448–z.

[62] R. Gillies, J. E. Freeman, L. C. Cancio, D. Brand, M. Hopmeier and J. R. Mansfield, *Diabetes Technology & Therapeutics*, 2003, **5**, 847–855.

[63] M. S. Chin, B. B. Freniere, Y.-C. Lo, J. H. Saleeby, S. P. Baker, H. M. Strom, R. A. Ignotz, J. F. Lalikos and T. J. Fitzgerald, *Journal of Biomedical Optics*, 2012, **17**, 026010.

[64] D. Yudovsky, A. Nouvong, K. Schomacker and L. Pilon, *Journal of Biomedical Optics*, 2011, **16**, 26009.

[65] H. Akbari, L. V. Halig, D. M. Schuster, A. Osunkoya, V. Master, P. T. Nieh, G. Z. Chen and B. Fei, *Journal of Biomedical Optics*, 2012, **17**, 0760051.

[66] N. T. Clancy, S. Arya, D. Stoyanov, M. Singh, G. B. Hanna and D. S. Elson, *Biomedical Optics Express*, 2015, **6**, 4179–4190.

[67] C. Solomon and T. Breckon, *Fundamentals of Digital Image Processing A Practical Approach with Examples in Matlab*, Wiley-Blackwell, Chichester, 2011.

[68] O. Marques, *Practical Image and Video Processing Using MATLAB®*, John Wiley and Sons, Inc., Hoboken, New Jersey, 2011.

[69] R. D. Hill and R. B. Smith, in *Examination of the Extremities: Pulses, Bruits, and Phlebitis*, Butterworths, Boston, 3rd edn., 1990.

[70] J. H. G. M. Klaessens, R. de Roode, R. M. Verdaasdonk and H. J. Noordmans, *Advanced Biomedical and Clinical Diagnostic Systems IX*, 2011, **7890**, year.

[71] P. Muntner, D. Shimbo, R. M. Carey, J. B. Charleston, T. Gaillard, S. Misra, M. G. Myers, G. Ogedegbe, J. E. Schwartz, R. R. Townsend, E. M. Urbina, A. J. Viera, W. B. White and J. T. Wright, *Hypertension*, 2019, **73**, E35–E66.

[72] G. Ogedegbe and T. Pickering, *Cardiology Clinics*, 2010, **28**, 571–586.

[73] M. Sonka, V. Hlavac and R. Boyle, in *Image pre-processing.*, Springer US, Boston, 1st edn., 1993, pp. 56 – 111.

[74] J. Chaki and N. Dey, *A Beginner's Guide to Image Preprocessing Techniques*, CRC Press, 2018.

[75] *Configurations for intensity-based registration - MATLAB imregconfig - Math-Works United Kingdom R2020a*, `https://uk.mathworks.com/help/images/ref/imregconfig.html#btcb0ax-1-optimizer` (last accessed on 15/03/20).

[76] D. Muthukumaran and M. Sivakumar, *International Journal of Scientific Research in Computer Science, Engineering and Information Technology*, 2017, **2**, 29–34.

[77] T. MathWorks, *Create customizable elliptical ROI - MATLAB drawellipse - MathWorks United Kingdom*, `https://uk.mathworks.com/help/images/ref/drawellipse.html` (last accessed on 19/05/20).

[78] J. T. Walker and S. Maddan, *Statistics in Criminology and Criminal Justice : Analysis and Interpretation*, Jones & Bartlett Learning, Burlington, 5th edn., 2020.

[79] P. C. Bruce, *Introductory Statistics and Analytics: A Resampling Perspective - Peter C. Bruce - Google Books*, John Wiley & Sons, New Jersey, 2015.

[80] M. Tepper, R. Neeman, Y. Milstein, M. B. David and I. Gannot, *Journal of Biomedical Optics*, 2009, **14**, 054048.

Appendices

.1 Preliminary Tests

Raw images of the colored liquid can be found in repository: Coloured liquid images.

.2 Pixel Calibration

The individual images collected for flat-field correction, by each camera, and their respective surf plots, can be seen in repository: Brightfield images and surf plots.

.3 Image offset calibration
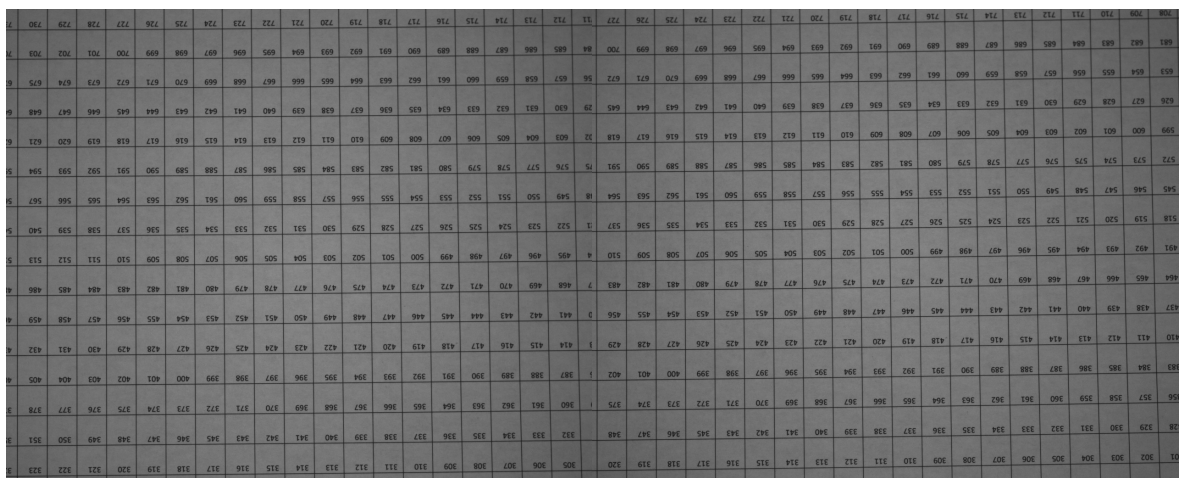
(a) Camera 1.

(b) Camera 2.
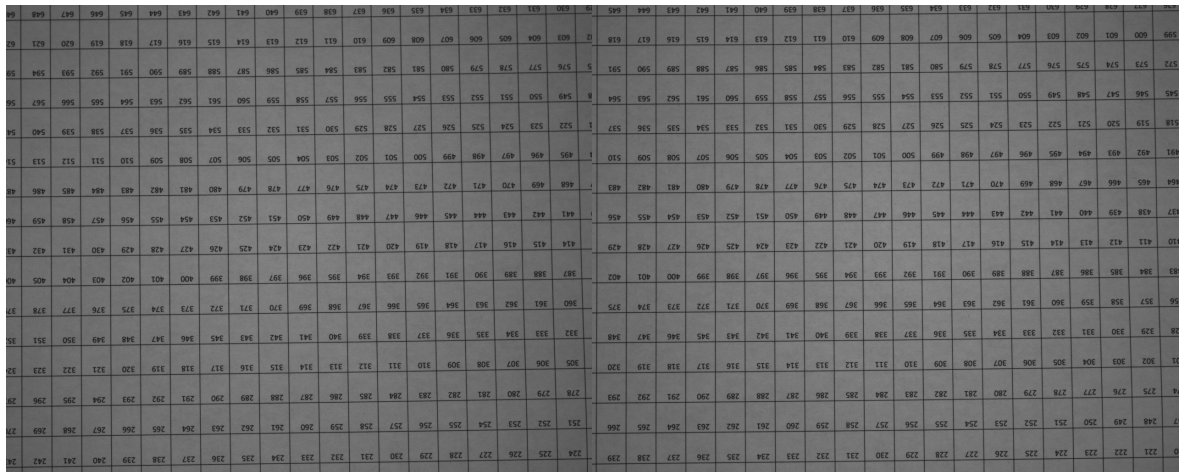
(c) Camera 3.

(d) Camera 4.

Figure 1: Grid images collected with no filters on the cameras, at the a distance of approximately 76 cm from the camera lens to the sample support.

.4 Image processing

```matlab
function NIPADmain % Main for calling all other NIPAD code

ToeROI = 4;
FootROI = 1;
FootSegCol = 2;
FootSegRow = 3;

FilterToe = [540 640];
FilterFoot = 610;
IsoFilter = 520;

% Import Images
[S,ChPos]=ImageImport('Brightfield folder containing images');

% Brightfield surf plots and flat-field correction of sample images
S1 = FlatFieldCorrection(S, ChPos); % Contains offset code

% Save arrays (Save all images)
ExportArray(S1);

% Further Alignment
[S1,Epos] = Centred(S1);

%Save arrays (Save all images)
ExportArray(S1);

% Regions of interest
[S1] = ROI(S1,Epos,ToeROI,FootROI,FootSegCol,FootSegRow);

% Save arrays (Save all images)
ExportArray(S1);

% Oxygen saturation maps - Method 1
OxymetryMap(S1,Epos,FilterToe,FilterFoot,IsoFilter,ToeROI,FootROI,FootSegCol,FootSegRow)
```

Figure 2: Main code that generates the processing functions.

The entire code, with every complete function, is available in BitBucket through the following link: MATLAB codes used for image processing.

.5   Test samples

All the images collected for all filters can be through the following link: Images collected with all filters.

Before and after comparison of all images for flat-field correction are available through the following link: Flat-field corrected images.

The results of the Image Offset code applied on all images, can be seen in the repository through this link: Results of image offset calibration.

All toe images after they have been further aligned can be seen through the following link: Further alignment toe images.

All regions of interest selected for the toe data and foot data can be visualised through the following links: Toe Regions of interest. and Foot Regions of Interest. The resulting pixel intensity graphs for each ROI can be seen through the following links: ROI Toe Graphs. and ROI Foot Graphs.

.6 Significance Test

Table 1: Z-test value results for the main Region of Interest of the foot area.

Filter (nm)	Oxygenated (no arterial occlusion)		Deoxygenated (arterial occlusion)		Z-test score
	Mean pixel intensity	Standard deviation	Mean pixel intensity	Standard deviation	
560	79.64856169	9.372486716	79.56423272	11.14253588	0.005791743078
580	86.06305585	13.32080613	85.46300109	10.61803676	0.03522509918
640	99.40979722	17.85346597	98.09831974	16.01413298	0.05468294418
620	101.5536383	19.74372904	98.17730411	18.2810214	0.1254795547
632	110.602914	15.78139878	114.331213	19.04905945	0.1507175046
600	108.0391447	14.92399791	104.3412599	13.90278519	0.1813008533
589	99.69277714	10.85329971	103.9944342	13.01523427	0.2538345881
650	98.92177915	17.09310673	105.5933095	18.70373578	0.2633034738
550	97.84554344	9.507401299	93.67472658	11.44266234	0.2803533091
520	84.60345636	10.20675806	79.47719195	10.2234733	0.3548481707
540	88.53288119	12.59712282	80.84518011	13.4727137	0.4168006284
510	108.7890801	13.10899725	99.89129645	9.26041324	0.5543805938
568	89.39039339	11.37245908	99.88635203	12.73100011	0.6148497471
500	98.77531581	7.632984546	90.11502757	9.513766693	0.7100166299
532	105.0354061	13.41519661	92.43837376	11.53415586	0.7120215273
610	95.00367014	15.39455556	112.9962351	18.69603075	0.7429276418

Table 2: Z-test value results for the first segmentation of the ROI belonging to the foot area.

Filter (nm)	Oxygenated (no arterial occlusion)		Deoxygenated (arterial occlusion)		Z-test score
	Mean pixel intensity	Standard deviation	Mean pixel intensity	Standard deviation	
620	110.9082863	7.625464518	112.0731952	5.842049739	0.121267566
520	73.73939109	7.570383625	75.0905838	6.562449474	0.134865658
640	96.83038293	8.026962156	94.68669178	7.925030387	0.19004367
580	93.5386064	7.100055069	91.18443189	7.260268348	0.23182614
500	94.0274639	8.414581269	96.90423729	6.498434859	0.270582374
550	99.31861268	9.12001786	102.9578782	7.327389032	0.311076339
532	87.89758318	11.04440449	82.87589454	8.889598525	0.35419923
510	95.06481481	12.35458438	100.8168236	10.15855003	0.359618643
650	92.51949153	8.527399243	97.51208412	8.548037053	0.413493798
540	95.58939109	5.680625364	92.02696171	4.864536076	0.476333767
600	100.1620841	9.121205533	107.5580038	8.77585823	0.584311666
560	73.45342122	7.157097095	79.26082863	5.992887902	0.622123556
589	102.4575643	9.313257982	112.6299749	9.316326269	0.77221051
632	114.4790333	9.040306956	126.9225047	9.07335604	0.971515081
568	74.36428123	9.105164598	91.91070308	9.398559663	1.340879742
610	91.87460766	7.8675876	118.3836158	6.549529886	2.589540008

Table 3: Z-test value results for the second segmentation of the ROI belonging to the foot area.

Filter (nm)	Oxygenated (no arterial occlusion)		Deoxygenated (arterial occlusion)		Z-test score
	Mean pixel intensity	Standard deviation	Mean pixel intensity	Standard deviation	
620	77.90018832	16.29695264	78.06738858	18.53880943	0.00677375
632	94.35925926	16.33521831	94.54070935	19.20454556	0.007196923
640	77.31848713	15.4565175	78.13807282	14.60917255	0.038535924
600	91.61497175	12.74298037	89.98038293	12.91682885	0.090086587
568	85.78571877	7.432504624	87.90662272	11.56025075	0.154321439
589	94.99231011	11.8724799	98.3210295	15.02914986	0.173797729
580	74.29993723	10.71398667	77.4396108	10.15651961	0.212672648
650	77.62774639	13.25505396	83.09274953	17.15049787	0.25212578
560	71.73427495	8.239632097	67.33386692	10.36975789	0.332237896
540	78.52419962	11.6323039	70.46384181	13.05006217	0.46107042
520	76.42215945	8.785188334	68.81155053	9.946578193	0.573485609
610	76.85621469	11.803686	89.10831764	16.3141276	0.608453112
550	97.97332078	10.72905677	87.73273697	12.42928934	0.623684367
500	98.64441306	9.388056809	88.67259887	12.19264167	0.648017725
532	98.17777778	10.32877469	82.15772128	9.936746672	1.117738
510	118.5229127	8.922224932	100.5295041	11.30725546	1.249240707

Table 4: Z-test value results for the third segmentation of the ROI belonging to the foot area.

Filter (nm)	Oxygenated (no arterial occlusion)		Deoxygenated (arterial occlusion)		Z-test score
	Mean pixel intensity	Standard deviation	Mean pixel intensity	Standard deviation	
510	102.7908977	10.61622217	103.2157878	7.576285934	0.032577596
550	102.7634024	8.048009051	102.126177	6.752123584	0.060657431
520	86.48132454	6.16610902	85.53844947	4.864239454	0.120053796
600	114.2934714	8.900185927	115.9661645	7.666759856	0.142392948
640	108.9664783	7.533612062	106.6645637	8.238252669	0.206199764
589	107.1352793	8.013718123	112.2911802	9.599035644	0.412325418
560	84.1888575	6.01141581	87.60546139	5.24702603	0.42818619
650	105.6034212	8.577840886	111.890113	11.01973959	0.450183172
580	99.98534212	4.880383871	95.7329253	6.1761353	0.540219593
532	104.1932517	9.413722852	96.65775267	7.263660929	0.633752444
500	100.5927809	5.704495258	95.57812304	4.4692243	0.691988162
632	121.8511613	9.340446924	130.6230069	8.468635935	0.695736309
620	118.9501255	5.742337752	112.537037	6.478675475	0.74077811
540	100.1780917	4.996795922	92.76443817	5.212951387	1.026679705
568	86.26120527	8.251226867	104.6322034	8.721358215	1.530147199
610	105.6661645	5.965288074	127.9836472	7.051769111	2.416238875

Table 5: Z-test value results for the fourth segmentation of the ROI belonging to the foot area.

Filter (nm)	Oxygenated (no arterial occlusion)		Deoxygenated (arterial occlusion)		Z-test score
	Mean pixel intensity	Standard deviation	Mean pixel intensity	Standard deviation	
640	92.07131199	14.1584744	93.27150031	15.06149721	0.058060038
632	106.1414313	14.71885586	104.3134965	17.66863223	0.07948855
620	89.16939736	15.96597406	87.15125549	16.08381423	0.089050957
589	98.5017263	10.91098622	101.3501883	13.00233929	0.167815059
560	78.81635279	8.646101343	75.25743879	10.52728569	0.261248194
580	78.34315756	11.2462943	82.88512241	11.39633198	0.283675895
568	95.32689893	6.561836694	99.85922787	11.13971033	0.350563851
600	104.9759573	12.75043613	98.32404269	11.85268514	0.382104827
650	93.84428751	12.12952501	102.8503139	16.9388946	0.432277439
540	81.59610797	11.94730888	73.08509102	12.00752578	0.502460474
550	98.63358443	9.699173321	89.16173886	10.82808878	0.651572577
520	86.29453861	8.184589752	77.01858129	10.00121618	0.717769695
610	87.96748274	12.57898624	102.842059	15.53626788	0.744094892
500	101.4737602	7.944003379	88.60486503	9.483554745	1.040235545
532	111.5493095	9.091032838	92.52922159	10.59710693	1.362246976
510	121.4925612	6.752352446	101.6865348	10.11431277	1.628630946

Table 6: Z-test value results for the fifth segmentation of the ROI belonging to the foot area.

Filter (nm)	Oxygenated (no arterial occlusion)		Deoxygenated (arterial occlusion)		Z-test score
	Mean pixel intensity	Standard deviation	Mean pixel intensity	Standard deviation	
589	102.2728186	6.819750547	102.7968927	7.252738713	0.052641866
560	89.27510986	4.854233215	90.20238544	4.711424518	0.137075737
550	97.40549278	6.222779868	95.18411802	5.692187915	0.263398787
632	120.4661959	6.203821476	123.1624922	6.787584624	0.293216531
650	117.6871626	7.538320078	121.7315443	8.284461018	0.361078789
510	102.0075016	7.448145088	96.3477715	5.853861356	0.597443027
520	94.55561833	5.042625726	89.86271186	4.201289304	0.715005801
600	122.2534212	8.27870205	114.1972065	6.285396818	0.775054909
640	119.565882	4.687325519	113.6994036	5.18414875	0.839384813
532	111.7462021	7.861780279	102.8633396	6.01886285	0.897147635
580	94.07561205	4.557895857	86.16751412	4.918070045	1.179369957
568	94.83750785	7.552681223	110.9821092	8.021944561	1.465303758
500	99.53003766	4.623414894	90.03873195	4.436311549	1.481266766
620	117.7140301	4.324863258	108.0105461	4.749277067	1.51064594
540	96.51465788	4.457373455	86.68411802	4.420821035	1.565900025
610	113.3978343	5.202474333	129.0892341	6.02109002	1.971940289

Table 7: Z-test value results for the sixth segmentation of the ROI belonging to the foot area.

Filter (nm)	Oxygenated (no arterial occlusion)		Deoxygenated (arterial occlusion)		Z-test score
	Mean pixel intensity	Standard deviation	Mean pixel intensity	Standard deviation	
632	106.6394852	16.29080624	106.7669178	15.65592966	0.005640051
640	101.9298807	16.56038557	102.3723478	13.09393346	0.020958531
620	94.92708726	17.24502314	91.44723792	15.28855361	0.150994018
560	80.53735091	7.53578313	77.88245449	9.558096702	0.21812414
580	76.28512241	10.92387048	79.54522913	9.155135402	0.228731579
589	93.01161331	10.59163776	96.8128688	12.4356275	0.23270819
568	99.91867546	6.659172549	104.2311676	10.65129314	0.34330665
650	106.5053045	15.85758585	116.7661017	15.76722246	0.458845449
550	91.18327056	8.72729209	85.08788449	9.676970162	0.467757092
540	78.97915882	10.38764683	70.17576899	10.90948563	0.584404386
610	94.43822976	12.5155339	110.8343063	16.35901005	0.796023786
600	115.1783741	12.10228859	100.2655995	13.23572855	0.831508599
520	90.2524796	6.051782859	80.68075957	7.617083596	0.983882771
510	113.0144068	6.271810375	96.94350282	7.358897201	1.662111331
500	98.52661645	6.331693784	81.05881984	7.796291736	1.739208745
532	116.8324545	6.934623508	97.73311362	8.187307528	1.780086425

Table 8: Z-test value results for ROI 1 belonging to the toe area.

Filter (nm)	Oxygenated (no arterial occlusion)		Deoxygenated (arterial occlusion)		Z-test score
	Mean pixel intensity	Standard deviation	Mean pixel intensity	Standard deviation	
520	161.4593575	21.99227408	161.8512657	23.56793611	0.012157773
620	153.222263	19.94501953	153.6746502	18.91366862	0.016458273
580	163.318956	26.47963861	165.0649861	26.83986311	0.046309568
610	244.4234055	7.464186305	243.4354069	8.923331175	0.084926524
650	119.663068	18.80302469	117.1017766	19.19017984	0.095333493
532	161.5388082	23.60670302	167.470468	23.35491607	0.17862487
560	160.8279964	18.31153961	156.0292438	17.99925125	0.186892381
589	182.7341858	31.22336927	191.6705099	32.5446656	0.198142513
500	115.7642157	17.54417068	123.9742152	19.86783451	0.309749826
632	111.6228709	17.13980069	118.5787957	13.32818324	0.320371584
510	130.3116713	20.72096758	120.7230753	20.18406564	0.331478879
568	176.4049578	23.73507756	159.8194539	24.76832226	0.483473828
550	188.4883916	24.04152993	172.7057282	18.77759614	0.517368923
600	227.094125	22.58639227	205.3407054	28.39943228	0.599499181
540	175.4626068	19.25527073	157.934647	17.34691139	0.676316378
640	171.5969813	29.48528344	141.280174	25.02985397	0.783855003

Table 9: Z-test value results for ROI 2 belonging to the toe area.

| Filter (nm) | Oxygenated (no arterial occlusion) | | Deoxygenated (arterial occlusion) | | Z-test score |
	Mean pixel intensity	Standard deviation	Mean pixel intensity	Standard deviation	
520	182.3554063	18.89845307	181.3246122	18.39310459	0.039087379
580	187.5201482	18.23410465	186.3422819	20.52163283	0.042906176
650	108.3493976	12.80790481	107.3687746	12.296779	0.055229653
532	166.7302616	18.25224428	170.8998381	18.5776414	0.160099368
500	134.940727	15.39457741	139.0588099	17.26950922	0.178002164
560	196.1451687	16.51867374	191.3446681	12.52017058	0.231602721
620	172.9587677	13.86909464	165.7433403	12.40950211	0.387709117
589	182.2927281	16.79769548	195.7792178	20.38273778	0.510610694
632	120.8276581	9.039944016	112.9036368	9.418067901	0.606994284
510	138.6114841	15.77463468	124.0530215	14.98012002	0.669226874
550	202.7845585	14.85573411	188.9081656	11.24817863	0.744693818
540	211.5379103	18.16406507	195.3680315	11.36327835	0.75469816
568	181.5552473	17.35661353	161.3652556	12.97051106	0.931804342
600	242.1871386	8.04658546	223.5297385	18.15713784	0.939434704
640	183.9798424	18.68456296	153.114663	16.95824794	1.22321575
610	235.2030997	2.359916569	239.8984031	1.69636876	1.615532421

Table 10: Z-test value results for ROI 3 belonging to the toe area.

| Filter (nm) | Oxygenated (no arterial occlusion) | | Deoxygenated (arterial occlusion) | | Z-test score |
	Mean pixel intensity	Standard deviation	Mean pixel intensity	Standard deviation	
520	168.4162593	23.92553672	168.425521	22.89111478	0.000279703
560	173.0929032	24.86491273	173.2999743	24.60156505	0.005919939
500	121.7571392	18.97228788	124.1427836	18.9175547	0.089042524
589	159.6425806	16.52874699	163.3491124	19.02530544	0.1470705
532	144.5739645	20.35365533	139.0074608	20.76327664	0.191449947
650	95.22451613	10.6667608	92.35197114	9.868436373	0.197676492
580	179.2332903	19.26840707	168.9156162	21.40715062	0.358231497
610	226.9233548	2.779381987	229.777377	6.056371231	0.428295361
550	169.5331613	18.39237211	156.1852328	18.40641598	0.512973961
568	146.9267097	20.91340787	129.8747106	19.59976415	0.594929994
510	119.2099305	17.67339906	103.52354	16.51503822	0.648499486
620	168.4113548	14.36230101	154.5037362	15.31917738	0.662302936
600	229.0270968	17.8548857	207.9166452	25.66104176	0.675284346
640	166.955871	18.60900548	148.1314094	15.10564857	0.785392463
540	193.2794839	20.38657572	169.0385902	22.27003055	0.802886941
632	113.0477419	8.89088214	99.8840505	9.215866117	1.027974372

Table 11: Z-test value results for ROI 4 belonging to the toe area.

| Filter (nm) | Oxygenated (no arterial occlusion) | | Deoxygenated (arterial occlusion) | | Z-test score |
	Mean pixel intensity	Standard deviation	Mean pixel intensity	Standard deviation	
640	135.6001006	18.58999915	135.0822055	16.53604733	0.020815475
610	211.9844064	13.24981524	211.3056112	18.05218966	0.030313051
520	142.4784569	17.90173122	143.7800601	19.76320804	0.048811999
500	105.1317635	13.64916747	106.8892786	13.65790401	0.091020433
532	116.0731463	15.82306541	113.7209419	16.13817411	0.104074741
589	138.4537223	13.10384047	145.0270541	19.19857913	0.282793645
580	162.1996982	17.27857502	153.5871743	23.4813898	0.295420195
650	72.13732394	10.94460881	79.11679198	10.0366693	0.470001372
600	204.1851107	22.53055023	185.5470942	27.00967107	0.529893825
560	154.6146881	13.53620325	144.6533066	11.87421737	0.553217314
510	99.39028056	11.45429559	90.39278557	10.42729519	0.58087128
550	152.5875252	15.85950912	139.6127255	10.79578233	0.676291165
620	155.4406439	12.92257543	139.3887776	15.93276059	0.782463391
632	100.8410463	7.245958098	88.57894737	8.75006096	1.079335365
568	123.9642857	11.54164152	104.9609218	10.10542999	1.238775396
540	177.8622244	15.94914752	152.1202405	11.29254685	1.317252214

.7 Final test samples

The trial results for the 'indoors' images, including the images captured, data pre-processing and processing, can be seen through the following link: Data collected indoors, the image processing results and final oximetry maps.

The trial results for the 'outdoors' images, including the images captured, data pre-processing and processing, can be seen through the following link: Data collected outdoors, the image processing results and final oximetry maps.

.8 Results and Discussions

A filter limit from 0 to 75% of the data was applied over each oximetry map presented in this appendix, for both toe and foot data, using the third quartile of the data. It was implemented in order to avoid extreme high values, but to still maintain the spread of data from 0 to 75%. If the limit was to be set for the highest number, the colour resulted would be mostly blue, hence 'diluting' the values as most of them were lower. A fidelity for such high values was therefore not needed. Both axes provide a reference of the size of the region shown in cm. The colour bar varies from blue to red (0 - 1), the latter showing the highest oxygenation.
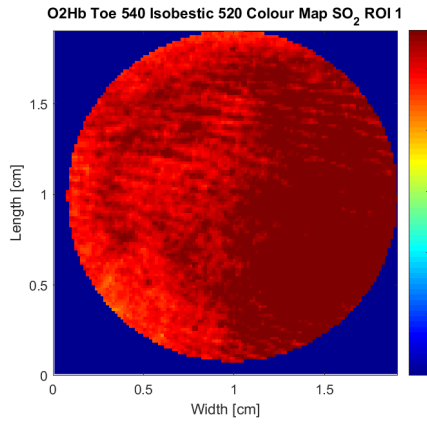
(a) O_2Hb region of interest 1.
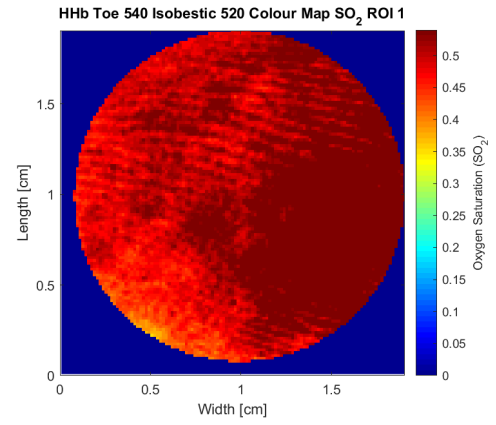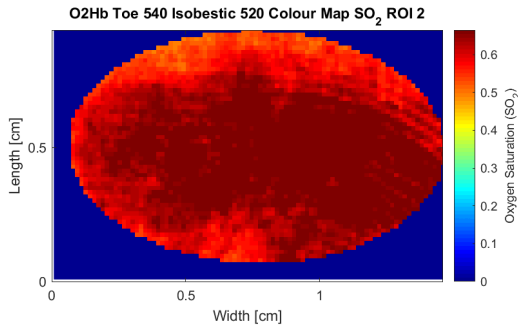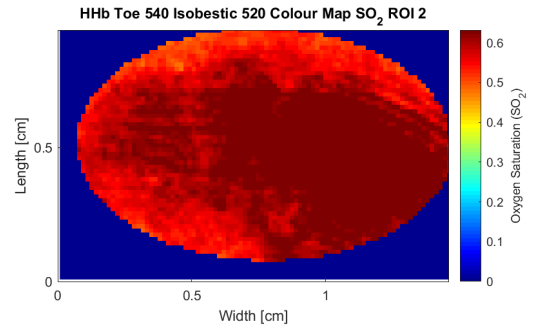
(b) HHb region of interest 1.

(c) O_2Hb region of interest 2.

(d) HHb region of interest 2.
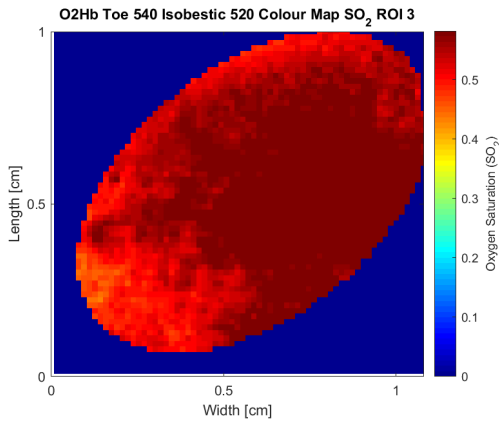
(e) O_2Hb region of interest 3.
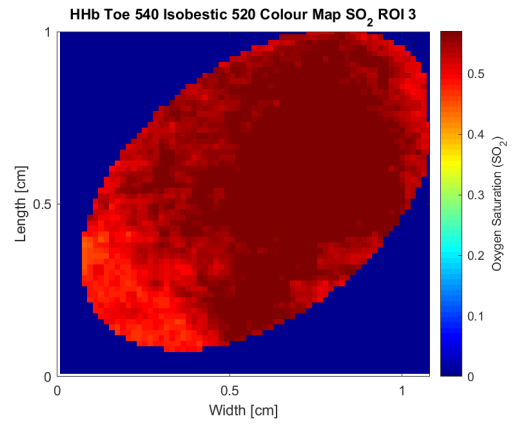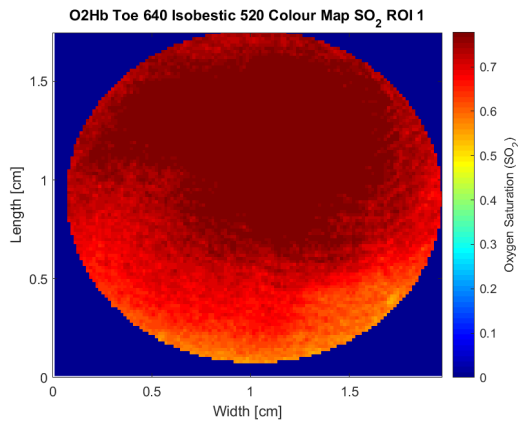
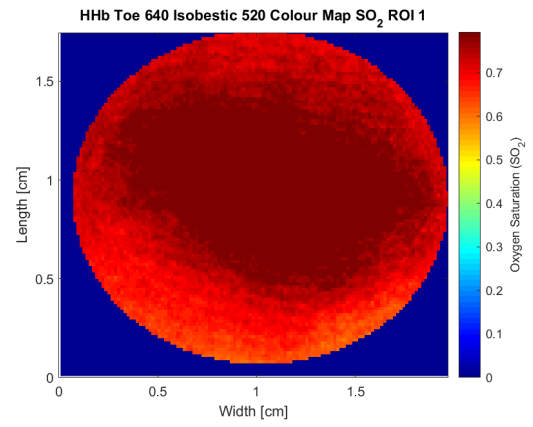(f) HHb region of interest 3.
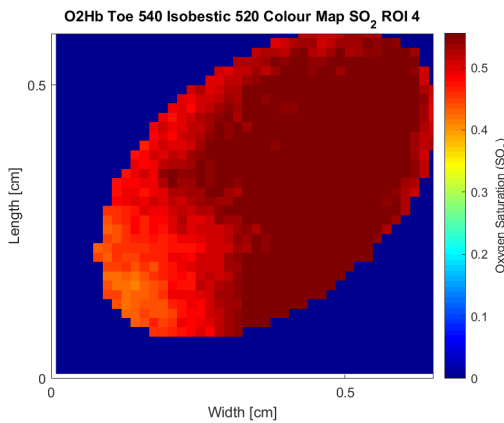
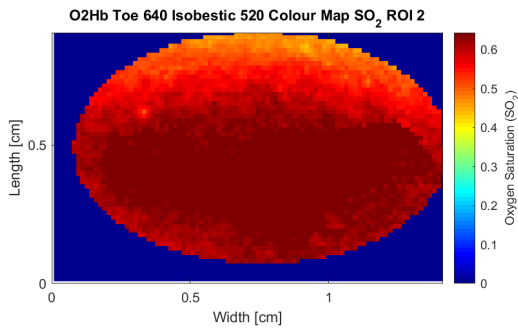(g) O_2Hb region of interest 4.
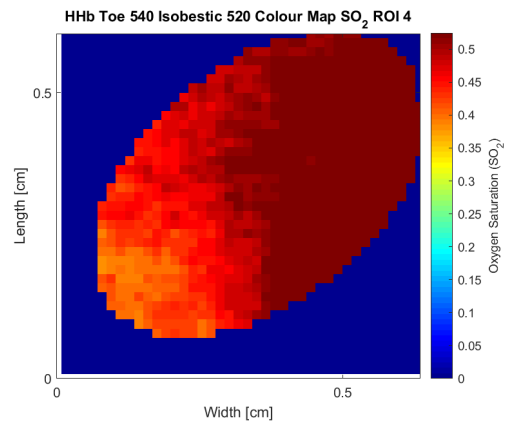
(h) HHb region of interest 4.

Figure 3: SO_2 oximetry colour maps (540 nm - isobestic 520 nm) for all four regions of interest of the toe images, collected in a controlled environment, at 540 nm.
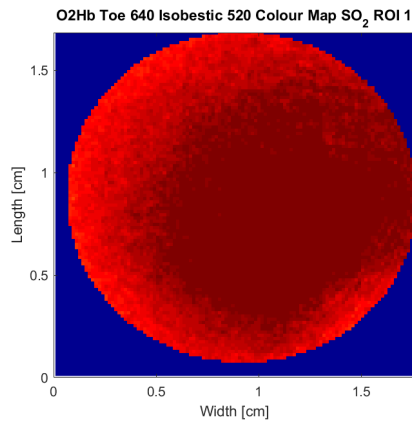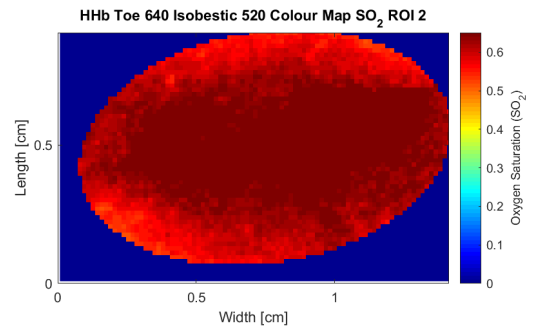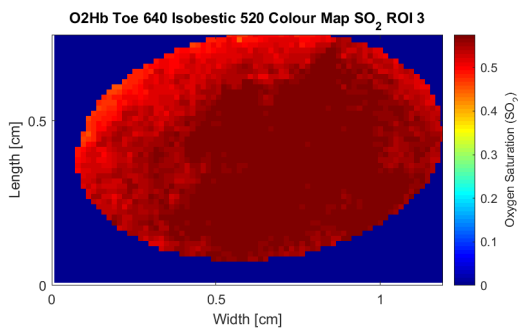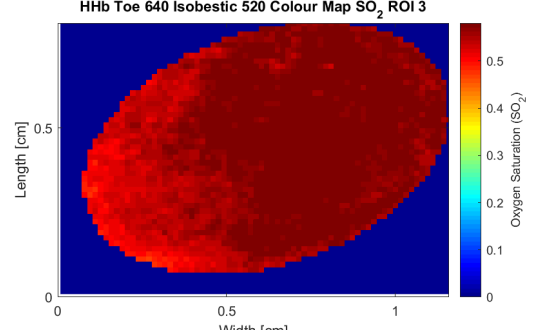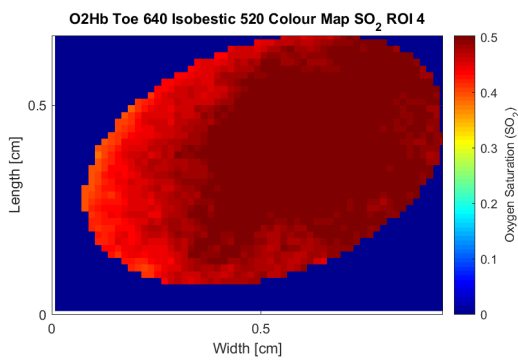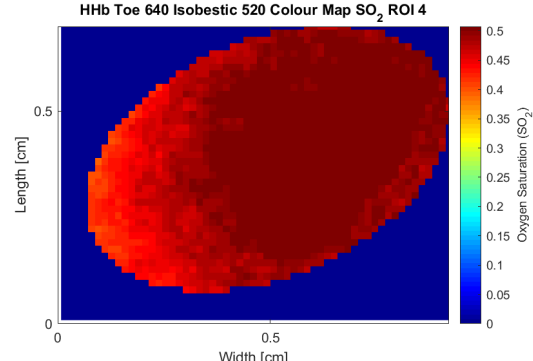
(a) O_2Hb region of interest 1.
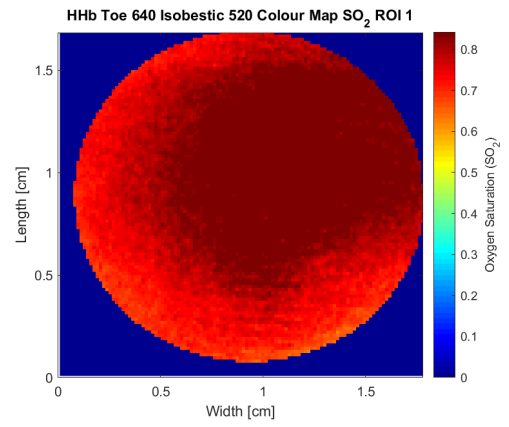
(b) HHb region of interest 1.
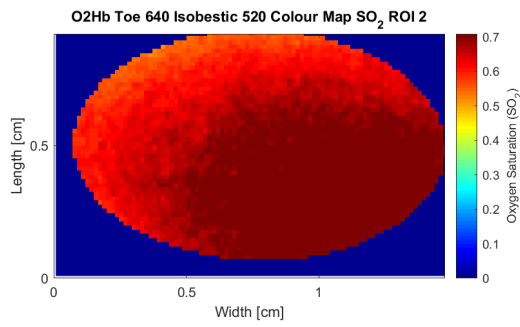
(c) O_2Hb region of interest 2.
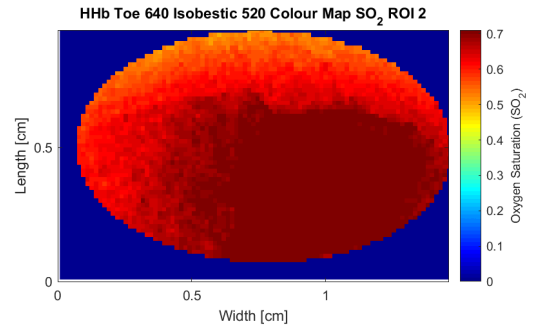
(d) HHb region of interest 2.
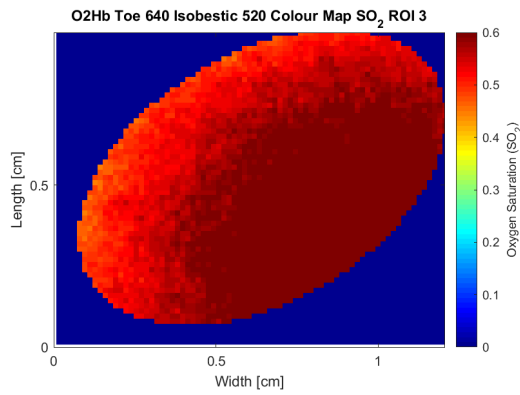
(e) O_2Hb region of interest 3.
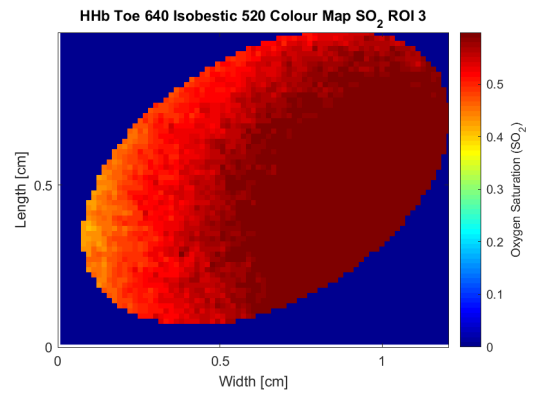
(f) HHb region of interest 3.
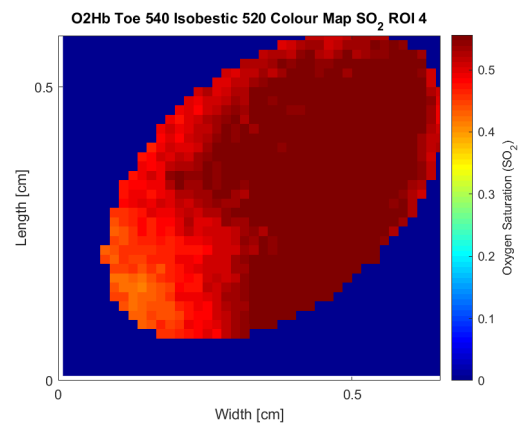
(g) O_2Hb region of interest 4.
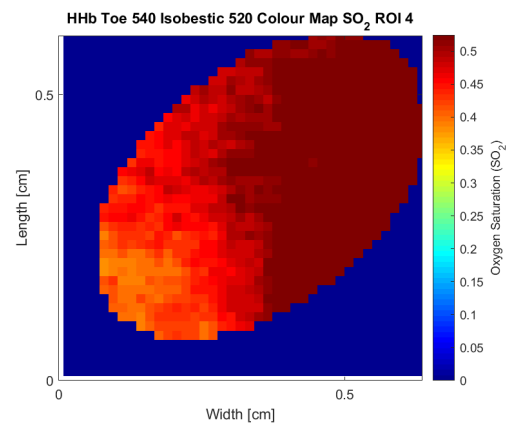
(h) HHb region of interest 4.

Figure 4: SO_2 oximetry colour maps (640 nm - isobestic 520 nm) for all four regions of interest of the toe images, collected in a controlled environment, at 640 nm.
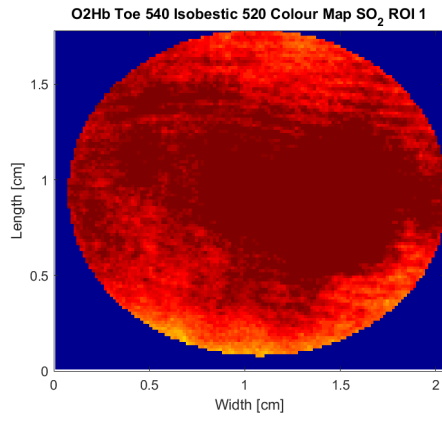
(a) O_2Hb region of interest 1.
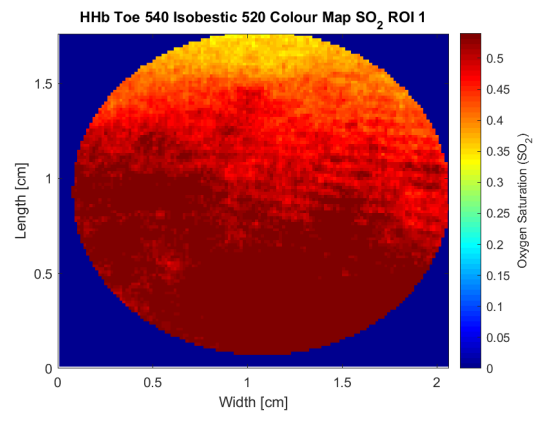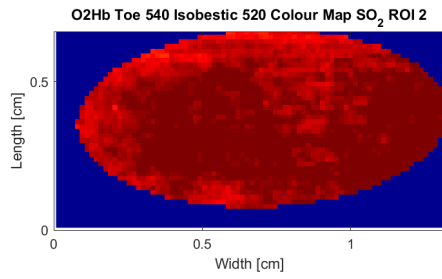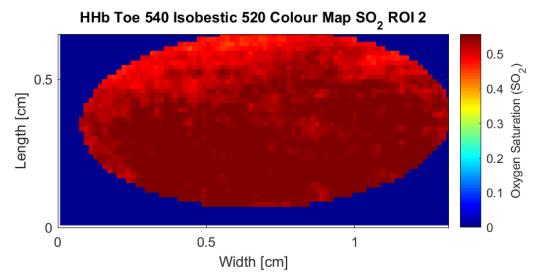
(b) HHb region of interest 1.

(c) O_2Hb region of interest 2.

(d) HHb region of interest 2.
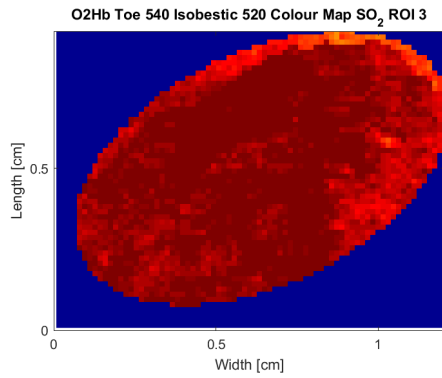
(e) O_2Hb region of interest 3.
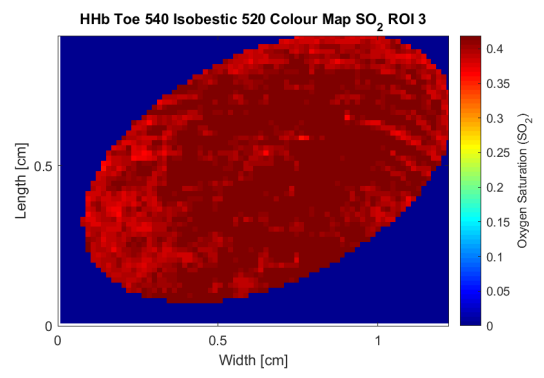
(f) HHb region of interest 3.
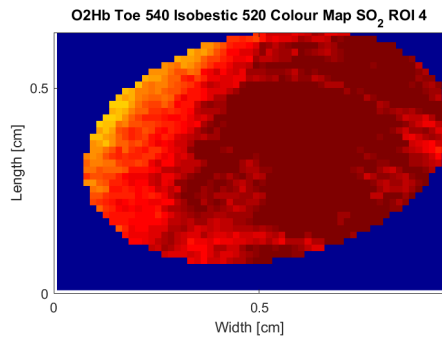
(g) O_2Hb region of interest 4.
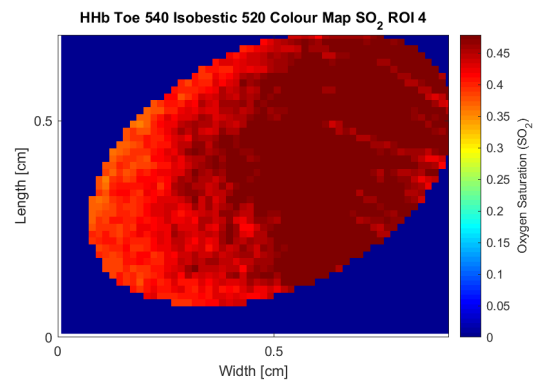
(h) HHb region of interest 4.

Figure 5: SO_2 oximetry colour maps (540 nm - isobestic 520 nm) for all four regions of interest of the toe images, collected in an uncontrolled environment, at 540 nm.

(a) O_2Hb region of interest 1.

(b) HHb region of interest 1.

(c) O_2Hb region of interest 2.

(d) HHb region of interest 2.

(e) O_2Hb region of interest 3.

(f) HHb region of interest 3.

(g) O_2Hb region of interest 4.

(h) HHb region of interest 4.

Figure 6: SO_2 oximetry colour maps (640 nm - isobestic 520 nm) for all four regions of interest of the toe images, collected in an uncontrolled environment, at 640 nm.
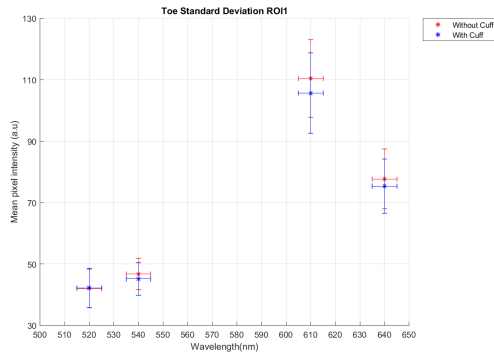
(a) ROI 1 collected indoors.
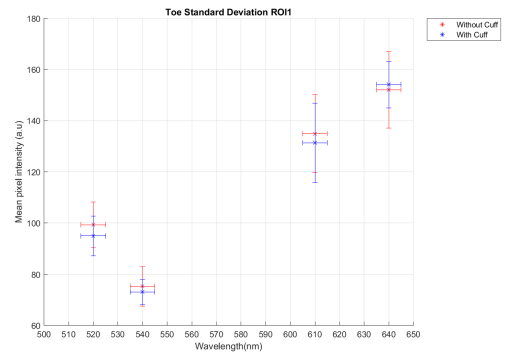
(b) ROI 1 collected outdoors.
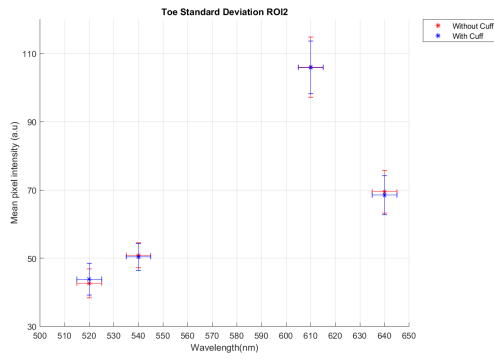
(c) ROI 2 collected indoors.
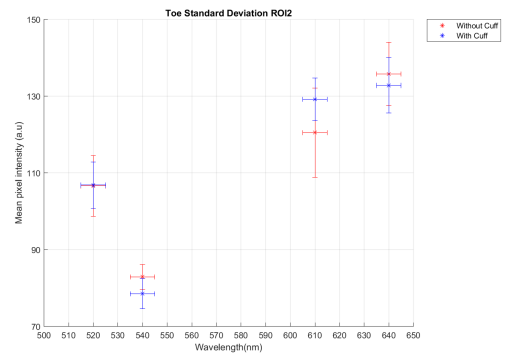
(d) ROI 2 collected outdoors.

Figure 7: Mean pixel intensity for the first and second ROI belonging to the second set of toe data, from both environments.
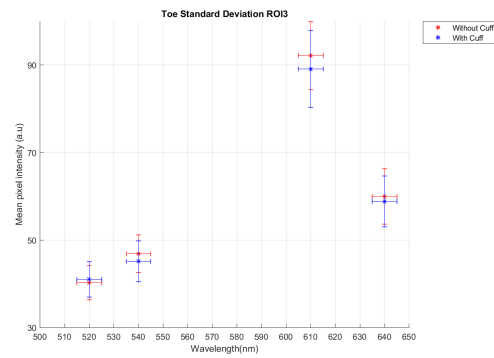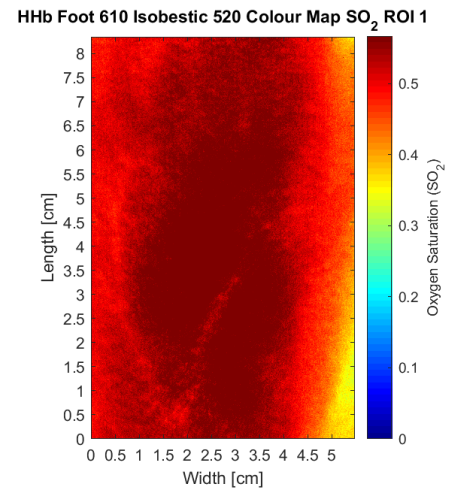
(a) ROI 3 collected indoors.
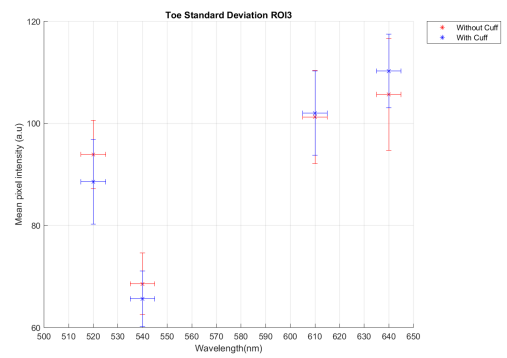
(b) ROI 3 collected outdoors.
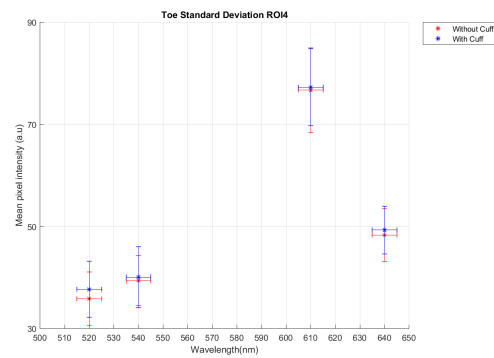
(c) ROI 4 collected indoors.
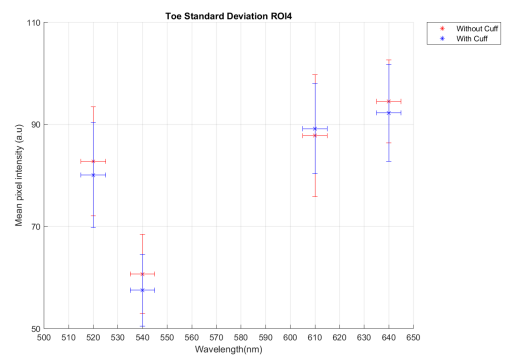
(d) ROI 4 collected outdoors.

Figure 8: Mean pixel intensity for the third and fourth ROI belonging to the second set of toe data, from both environments.
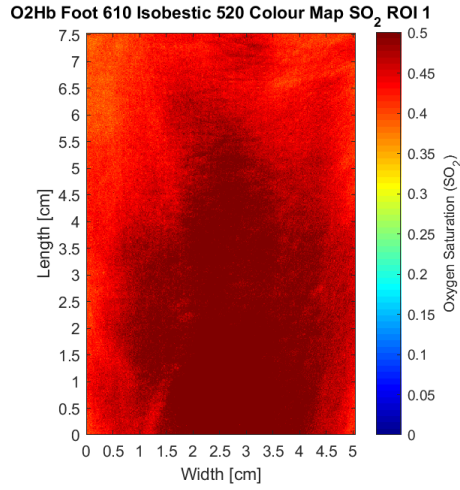
(a) O_2Hb ROI of the foot image, collected indoors.
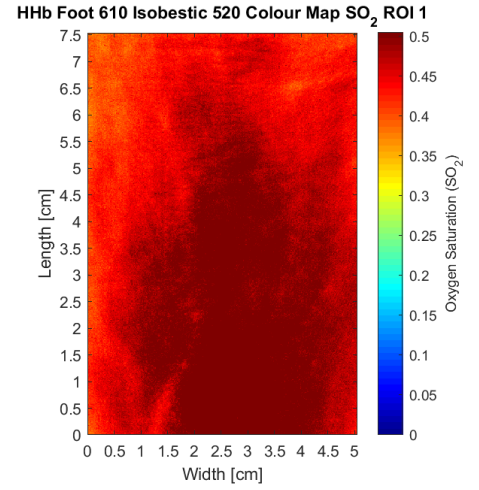
(b) HHb ROI of the foot image, collected indoors.
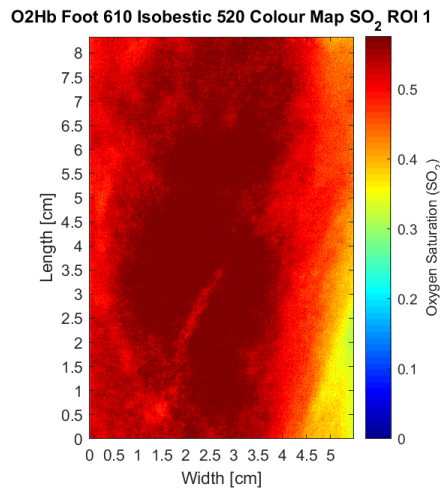
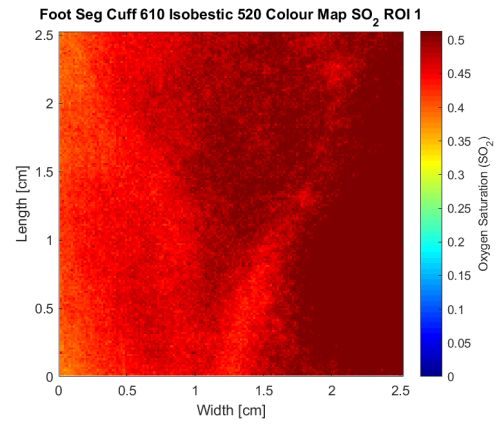(c) O_2Hb ROI of the foot image, collected outdoors.

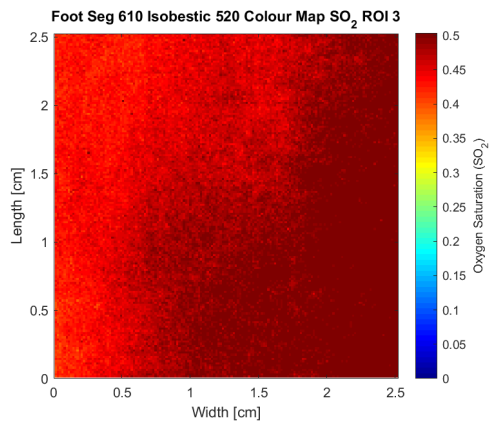(d) HHb ROI of the foot image, collected outdoors.

Figure 9: SO_2 oximetry colour maps (610 nm - isobestic 520 nm) for the main ROI of the foot data, collected in both environments at 610 nm, with cuff occlusion (deoxygenated - HHb) and without cuff occlusion (oxygenated - O_2Hb).
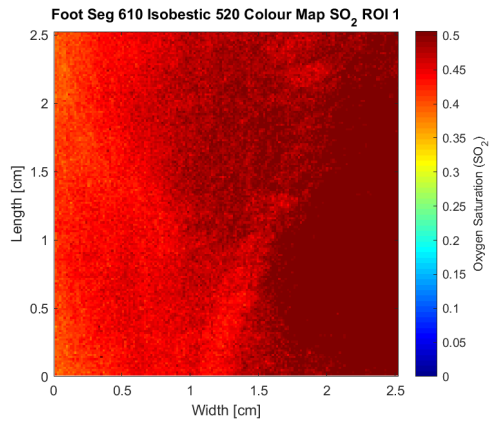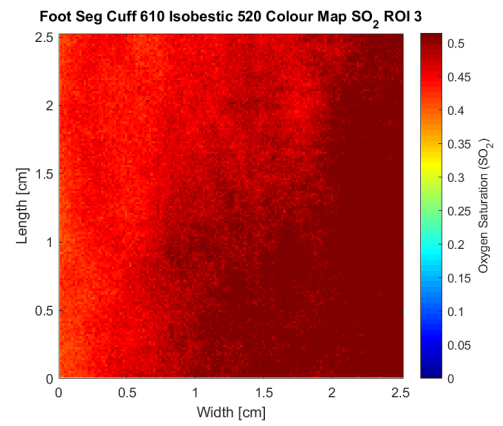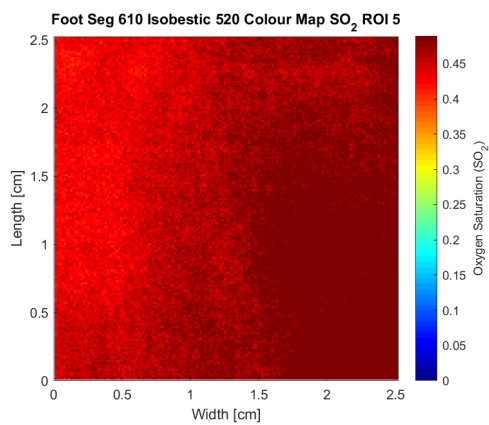
(a) O_2Hb Segment 1 of foot region.

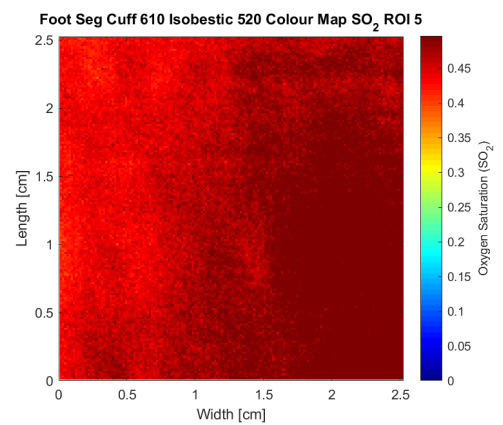(b) HHb Segment 1 of foot region.

(c) O_2Hb Segment 3 of foot region.

(d) HHb Segment 3 of foot region.

(e) O_2Hb Segment 5 of foot region.

(f) HHb Segment 5 of foot region.

Figure 10: SO_2 oximetry colour maps (610 nm - isobestic 520 nm) for the oxygenated and deoxygenated segmentation 1, 3 and 5, belonging to the left side of the main foot ROI, presented above in Figure 9. All maps displayed in this figure are from images collected in a controlled environment at 610 nm.

(a) O_2Hb Segment 2 of foot region.

(b) HHb Segment 2 of foot region.

(c) O_2Hb Segment 4 of foot region.

(d) HHb Segment 4 of foot region.

(e) O_2Hb Segment 6 of foot region.
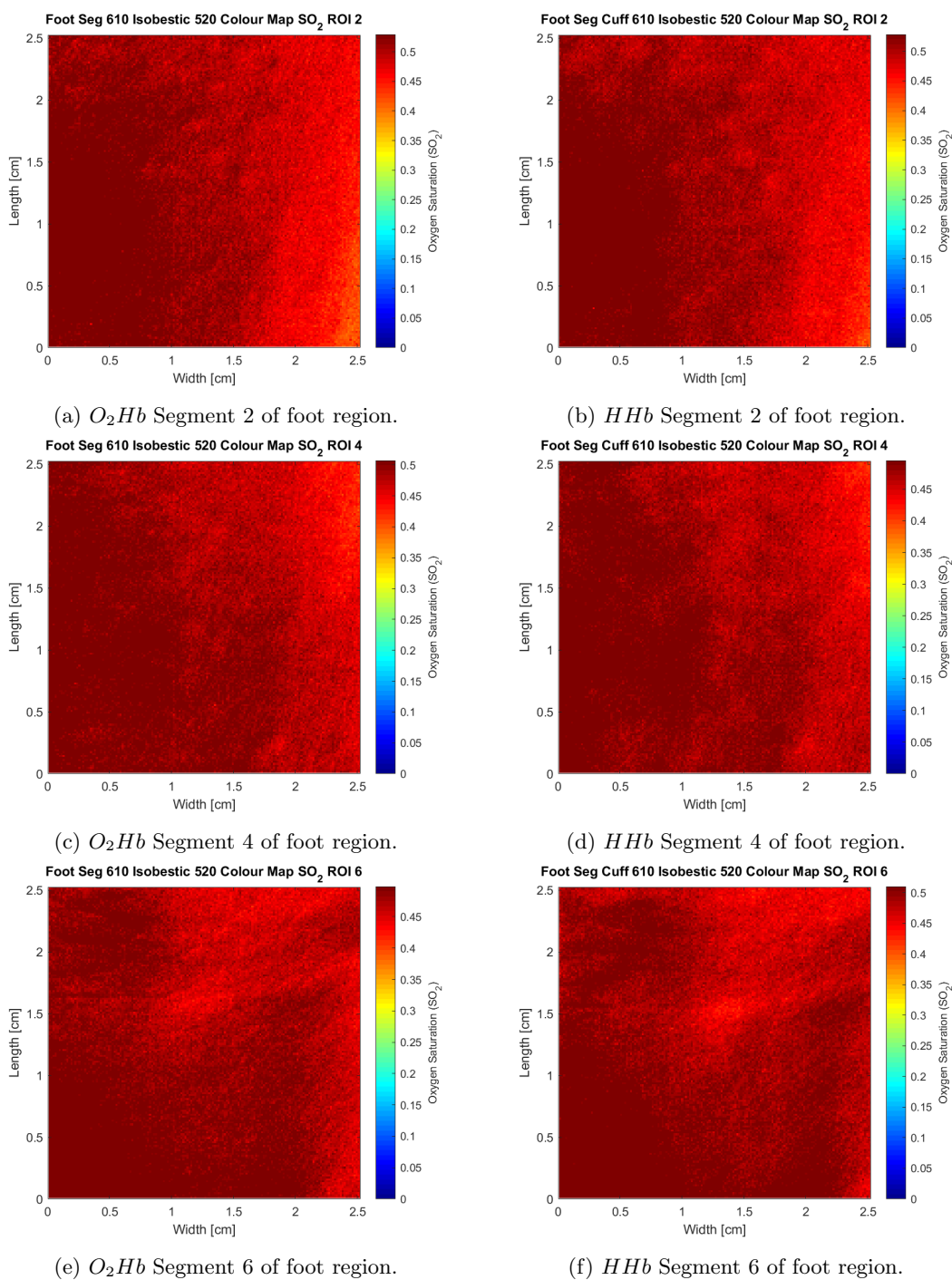
(f) HHb Segment 6 of foot region.

Figure 11: SO_2 oximetry colour maps (610 nm - isobestic 520 nm) for the oxygenated and deoxygenated segmentation 2, 4 and 6, belonging to the right side of the main foot ROI, presented in Figure 9. All maps displayed in this figure are from images collected in a controlled environment at 610 nm.

(a) O_2Hb Segment 1 of foot region.

(b) HHb Segment 1 of foot region.

(c) O_2Hb Segment 3 of foot region.

(d) HHb Segment 3 of foot region.

(e) O_2Hb Segment 5 of foot region.
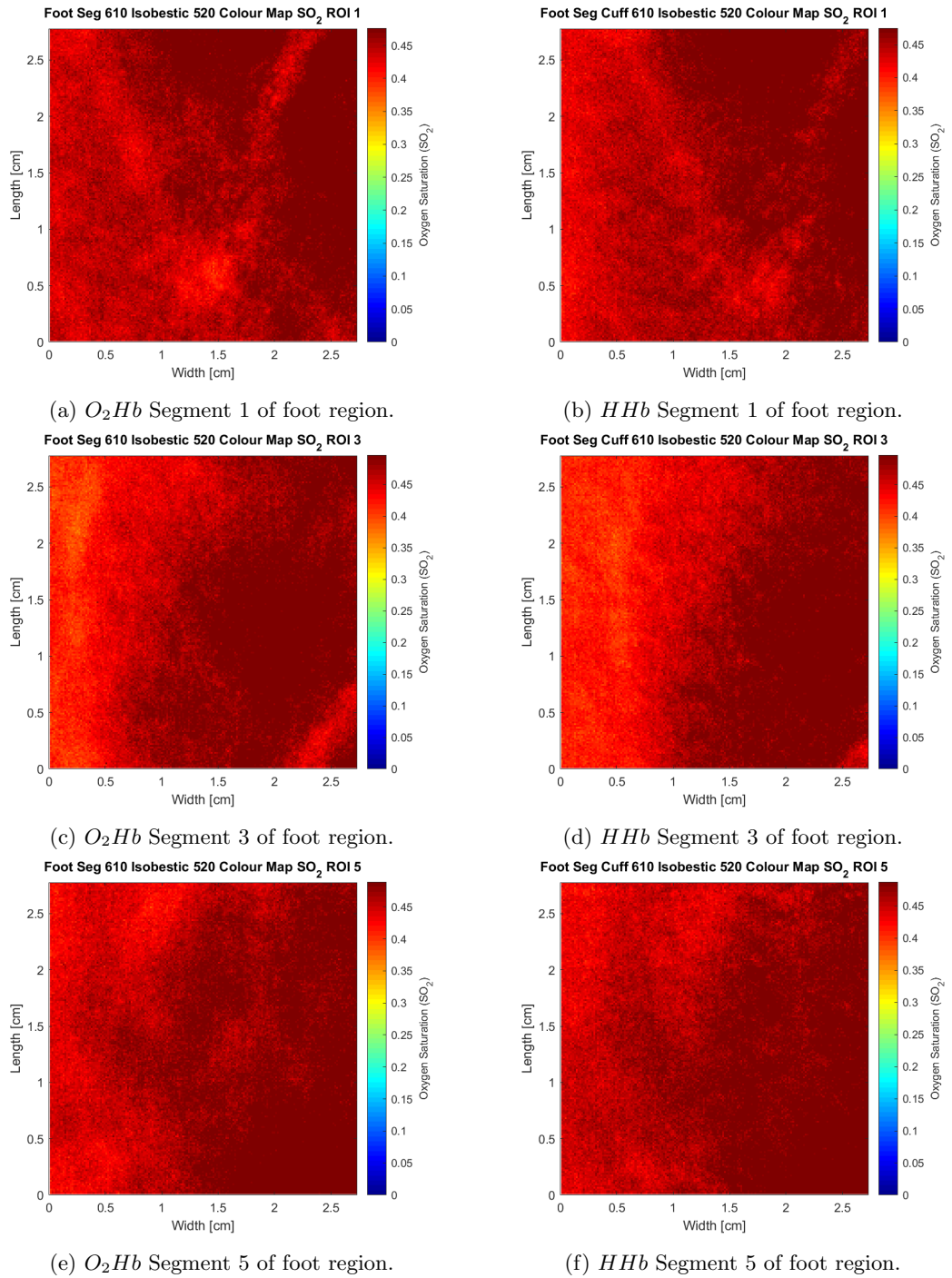
(f) HHb Segment 5 of foot region.

Figure 12: SO_2 oximetry colour maps (610 nm - isobestic 520 nm) for the oxygenated and deoxygenated segmentation 1, 3 and 5, belonging to the left side of the main foot ROI, presented in Figure 9. All maps displayed in this figure are from images collected in an uncontrolled environment at 610 nm.

(a) O_2Hb Segment 2 of foot region.

(b) HHb Segment 2 of foot region.

(c) O_2Hb Segment 4 of foot region.

(d) HHb Segment 4 of foot region.

(e) O_2Hb Segment 6 of foot region.

(f) HHb Segment 6 of foot region.

Figure 13: SO_2 oximetry colour maps (610 nm - isobestic 520 nm) for the oxygenated and deoxygenated segmentation 2, 4 and 6, belonging to the right side of the main foot ROI, presented in Figure 9. All maps displayed in this figure are fro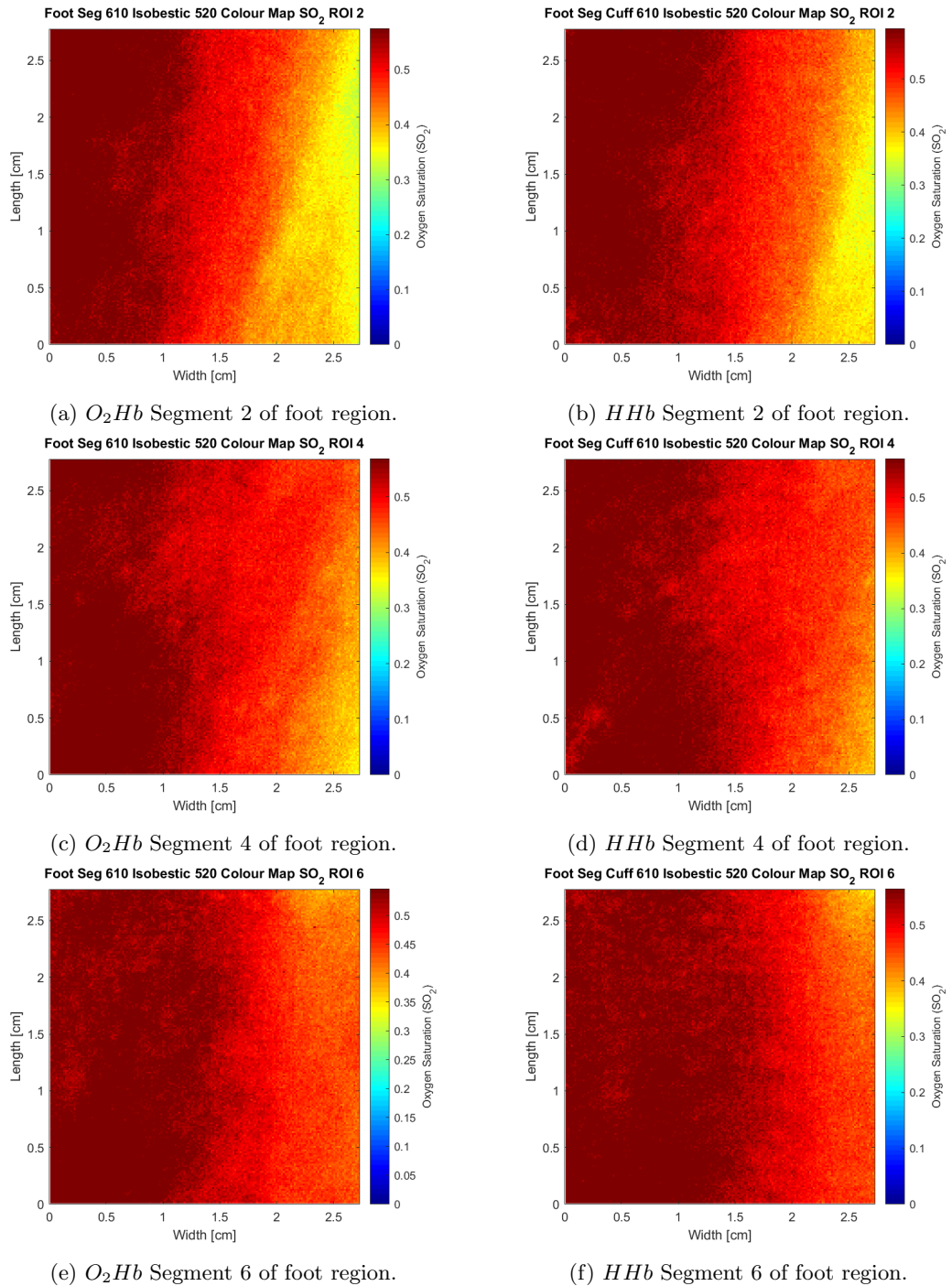m images collected in an uncontrolled environment at 610 nm.